

Copyright
by
Dipankar Koley
2011

**The Dissertation Committee for Dipankar Koley Certifies that this is the approved
version of the following dissertation:**

**Applications of Scanning Electrochemical Microscopy in Biological
Systems**

Committee:

Allen J. Bard, Supervisor

Richard M. Crooks

Keith J. Stevenson

Charles B. Mullins

Simon M. Humphrey

**Applications of Scanning Electrochemical Microscopy in Biological
Systems**

by

Dipankar Koley, B. Tech., M.S.

Dissertation

Presented to the Faculty of the Graduate School of

The University of Texas at Austin

in Partial Fulfillment

of the Requirements

for the Degree of

Doctor of Philosophy

The University of Texas at Austin

August, 2011

Dedication

To my parents and sister for their continuous encouragement and support, without whom many of my achievements would be impossible.

To Carole, friends and lab members for sharing many memorable moments in graduate school both inside and outside the lab.

Acknowledgements

I would like to thank Dr. Allen J Bard first for his guidance, and teaching me electrochemistry and above all how to become a good scientist. I am also indebted to him for teaching me how to see a big picture out of any complex problem besides asking a very important question “Why”. I am also thankful to Dr. Fu-Ren (Frank) Fan for many stimulating scientific discussions.

I would like to thank my collaborator Matthew Ramsey and Marvin Whiteley for their help in my microbiology projects. Those countless hours of discussion with Matthew on microbiology were invaluable and helped me to enrich my knowledge in this subject.

I would also like to thank Angie Nelson both for manuscript preparation and administrative work as well as Penny Kile for their tremendous help with paperwork during my entire time in graduate school.

Applications of Scanning Electrochemical Microscopy in Biological Systems

Dipankar Koley, Ph.D.

The University of Texas at Austin, 2011

Supervisor: Allen J Bard

The main theme in this dissertation is to develop Scanning Electrochemical Microscopy (SECM) based electroanalytical techniques to study quantitative biology in real time. The multidrug resistance (MDR) phenomenon in live cancer cells was studied using mimic drug molecules such as menadione with the aid of SECM. Real time quantitative detection of thiodione (menadione-conjugate) pumped out of the cells was determined to be 140 μM due to exposure of 500 μM menadione to the cells. Selective blocking of these MDR pumps in live intact cells was also achieved by small molecules such as MK571 as well as by the MDR specific antibody. An approximately 50% drop in thiodione flux was observed in both cases of MDR pumps inhibition.

This SECM technique was also extended to measure the permeability of a highly charged hydrophilic molecule passing through the membrane of a single living cell. The permeability was measured to be $6.5 \pm 2.0 \times 10^{-6}$ m/s. Real time monitoring of morphological changes in a live HeLa cell due to addition of varying concentration of surfactant such as Triton X-100 was also demonstrated by SECM.

This electroanalytical technique was also expanded to study quantitative microbiology. Real time quantitative detection of pyocyanin produced by *Pseudomonas aeruginosa* (PA14 strain) biofilm locally was determined to be 2.5 μM after 6 h. Pyocyanin (PYO) was also observed to be reduced by PA14 biofilm, thus maintaining a

reduced atmosphere above the biofilm even in presence of oxygen. Spatial mapping of this reduced PYO showed that this reduced zone was only formed up to 500 μm above the biofilm. The cells are also able to modulate the height of the reduced PYO zone in accordance to the availability of Fe(III/II) in the solution to scavenge iron from the surrounding environment.

Real time spatial mapping hydrogen peroxide across polymicrobial biofilm (*Sg* and *Aa*) was also achieved with the aid of SECM. The local peroxide concentration produced by *Sg* was measured to be 1 mM, which is significantly higher than the bulk peroxide concentration. This study also showed that the local concentration across the microbial film is more important than the bulk concentration since bacteria communicate locally in real world.

Table of Contents

List of Tables	xiii
List of Figures	xiv
CHAPTER 1: Introduction to Scanning Electrochemical Microscopy (SECM).....	1
1.1 Ultramicroelectrode (UME) as a SECM Probe	1
1.2 SECM Modes of Operation	5
Feedback Mode.....	9
Generation–Collection Mode.....	11
1.3 SECM Studies with Living Cells.....	13
1.4 Square Wave Voltammetry (SWV)	17
1.5 References.....	19
CHAPTER 2: Effects of Triton X-100 on Membrane Permeability of a Single HeLa cell as Studied by SECM	22
Abstract.....	22
2.1 introduction.....	23
2.2 Materials and Methods.....	25
Chemicals.....	25
Cell Culture.....	25
Fluorescent Based Viability Assay.....	26
SECM Experiments	26
Electrochemistry and Electrode Fabrication.....	26
X-scan Over Single Cell Experiment.....	27
Approach Curve Over Single Cell Experiment	30
I-t Experiment Over Single Cell	30
2.3 Simulation	30
X-Scan Simulation	34
Permeability Measurement	36
2.4 Results.....	36
Fluorescence-Based Cell Viability	36

Cellular Topography without Surfactant	38
Cell Membrane Permeability	38
Cellular Topography in Presence of TX100	42
Current-time (i_T vs. t) Response over a Single Cell.....	44
2.5 Discussion	46
2.6 Conclusion	47
2.7 Acknowledgement	47
2.8 Reference	48
Chapter-3: Inhibition of the MRP1-Mediated Transport of the Menadione-Glutathione Conjugate (Thiodione) in HeLa Cells as Studied by Scanning Electrochemical Microscopy	52
Abstract.....	52
3.1 introduction.....	53
3.2 Materials & Methods	57
Chemicals.....	57
Cell Culture.....	58
Cytotoxicity Assay.....	58
SECM Experiment.....	60
Simulation Model.....	62
3.3 Results.....	69
Cytotoxicity Experiments	69
Thiodione Flux from a Monolayer of HeLa Cells	71
Model of Thiodione Release.....	73
Inhibition of MRP1 Pump by MK571	73
Inhibition of MRP1 Pump by QCRL-4 Antibody.....	75
3.4 Discussion	78
Cellular Response to Menadione Induced Oxidative Stress.....	78
Model of Thiodione Efflux from a Monolayer of HeLa Cells.....	80
Selective Blocking of MRP1 by MK571	80
Selective Blocking of MRP1 by QCRL-4 Antibody	81
3.5 Conclusion	82

3.6 Acknowledgement	83
3.7 References.....	84
CHAPTER 4: Quorum Sensing & Electrochemistry: as Studied with <i>Pseudomonas aeruginosa</i> Biofilm using SECM	87
Abstract.....	87
4.1 Introduction.....	88
<i>Pseudomonas aeruginosa</i>	88
Quorum Sensing.....	88
Quorum Sensing (QS) Circuit for <i>P. aeruginosa</i>	92
Biofilm Formation	92
Function of Phenazine compounds	98
Basic Electrochemistry of Phenazine Derivative Compounds	100
Bacterial iron acquisition	102
Motivation.....	103
4.2 Materials & Methods	104
Materials	104
Preparation of Buffer	104
Bacteria Culture & Biofilm Sample Preparation	105
Measurement of pH and Pyocyanin Production by Planktonic Bacteria.....	105
Detection of <i>phzA</i> Induction in a Colony Biofilm	106
Determination of Fe(II) in Presence of Pyocyanin (PYO).....	107
Electrochemical Measurements	107
Calibration Curve for Pyocyanin (PYO).....	107
Real Time Quantitative Detection of Pyocyanin (PYO) using SECM.....	110
Mapping of Reduced / Oxidized Pyocyanin (PYO) Layer above Biofilm using SECM:.....	110
Electrochemical Imaging of a Biofilm using SECM	111
4.3 Results.....	111
Pyocyanin (PYO) Production by Planktonic Bacteria	111
Activation of QS Controlled Genes in a <i>P. aeruginosa</i> Colony Biofilm:	111

Calibration Curve for Pyocyanin (PYO).....	113
Real Time Quantitative Detection of Pyocyanin (PYO).....	115
Spatial Mapping of Reduced/Oxidized Pyocyanin (PYO) above Biofilm	117
Determining the Mechanism of PYO Reduced Layer Development.	122
Reduction of Iron (III) in the Presence of Pyocyanin (PYO)	125
Electrochemical Imaging of a Biofilm.....	127
4.4 Discussion.....	129
4.5 Conclusion	133
4.6. Acknowledgement:	133
4.7 References.....	133
CHAPTER 5: Real-time Mapping of a Hydrogen Peroxide Concentration Profile Across a Polymicrobial Biofilm Using SECM	138
Abstract.....	138
5.1 Introduction.....	139
5.2 Materials and Methods.....	140
Chemicals.....	140
Bacterial Strains Culture and Preparation.....	141
Ultramicroelectrode Fabrication	142
Calibration Curves for H ₂ O ₂ in CDM.....	142
Stability Tests.....	143
Real-Time Electrochemical Monitoring of Hydrogen Peroxide by SECM on a Sg Biofilm	143
Y-scan and Approach Curve SECM Experiment on a Sg and Aa Coculture Biofilm	145
Fluorometric Measurements of Hydrogen Peroxide.....	147
Confocal Laser Scanning Microscopy	147
Simulations	148
5.3 Results.....	151
Calibration Curves for H ₂ O ₂ in CDM.....	151
Stability Tests.....	153

Real-Time Quantitative Measurement of Hydrogen Peroxide Produced by Living <i>Sg</i> Colony Biofilms with SECM	155
Y-scan and Approach Curve SECM Experiments over a <i>Sg</i> and <i>Aa</i> Cocultured Bacterial Biofilm.....	156
Effect of the Number of <i>Sg</i> Bacteria on H ₂ O ₂ Current Response.....	157
5.4 Discussion	159
Real-Time Quantitative Measurement of Local Hydrogen Peroxide Concentration Produced by a <i>Sg</i> Biofilm.....	159
KatA Mediated Decomposition of Hydrogen Peroxide in a Mixed Species Biofilm	164
5.5 Conclusions.....	165
5.6 Acknowledgement	166
5.7 References.....	166
CHAPTER 6: Electrochemical Characterization of Nanoelectrodes using SECM	170
Testing of Nanoelectrodes	170
Cleaning of Electrode	172
Approach Curve with Nanoelectrodes.....	175
SECM Imaging with Nanoelectrodes	177
Major challenges associated with Nanoelectrodes & Commercial CHI SECM	181
Appendix A: Publications from this dissertaion	183
Appendix B: List of Protocols	184
B.1 Subculture of HeLa Cells	184
B.2 Freeze Storing of HeLa Cells.....	185
B.3 Menadione-Antibody SECM Experiment Protocol	185
References.....	188
Vita	203

List of Tables

Table 3.1: The boundaries in comsol multiphysics model showed in figure 3.3 and their corresponding boundary conditions.....	66
Table 3.2: The fitted simulation parameters for respective menadione concentration.	68
Table 4.1: List of electroactive phenazine derivative compounds and their respective half wave potential.	101
Table 5.1: Comparison of hydrogen peroxide production concentration from <i>Sg</i> by fluorometric and electrochemical measurement.	163

List of Figures

Figure 1.1: Simulated hemispherical diffusion layer of a 10 μm radius ultramicroelectrode (UME).....	4
Figure 1.2: Schematic diagram of a Scanning Electrochemical microscope (SECM) setup.	7
Figure 1.3: Negative and positive feedback approach curves in SECM	8
Figure 1.4: SECM feedback modes of operation.....	10
Figure 1.5: SECM generation-collection mode of operation.....	12
Figure 1.6: SECM image of thiodione transport from a single living cell	15
Figure 1.7: Square wave voltammetry	18
Figure 2.1: Experimental setup for SECM experiment.	28
Figure 2.2: Topographical SECM image of a single HeLa cell.....	29
Figure 2.3: The schematics of simulation model in 2D axial symmetry.	33
Figure 2.4: Determination of height of a single HeLa cell	35
Figure 2.5: Viability test of HeLa cells in presence of varying concentration of TX-100.....	37
Figure 2.6: Permeability measurement of a single HeLa cell in presence of varying concentrations of TX-100	41
Figure 2.7: Topographical variation of a single HeLa cell in presence of TX-100	43
Figure 2.8: I-t experiment over a single HeLa cell in presence of TX-100.....	45
Figure 3.1: Schematic diagram of cellular response to menadione in the presence or absence of MRP1 blocker MK571.....	55
Figure 3.2: Cellular response to varying concentration of menadione	61
Figure 3.3: The mesh distribution of Comsol Multiphysics model in 2-D axial symmetry.....	64

Figure 3.4: Cellular viability w.r.t time (h) in presence of 500 μM menadione in buffer solution.....	70
Figure 3.5: Cellular viability w.r.t time (min) on exposure of 500 μM menadione and 50 μM MK571.....	70
Figure 3.6: Cyclic voltammetry of thiodione efflux coming out from the monolayer of HeLa cells on exposure to 500 μM menadione.....	72
Figure 3.7: Cellular response to 500 μM menadione in presence of MK571 blocker	74
Figure 3.8: Cellular response to 500 μM menadione in presence of antibody based blocker.....	76
Figure 3.9: Thiodione concentration (μM) w.r.t time (min) in presence of QCRL-4 antibody.....	77
Figure 4.1: Schematic representation of a quorum sensing circuit of the Gram-negative bacteria (<i>Vibrio fischeri</i>).	90
Figure 4.2: List of different autoinducers or quorum sensing (QS) molecules. ...	91
Figure 4.3: Quorum sensing circuit for <i>P. aeruginosa</i> . (Adapted from reference 3).	93
Figure 4.4: Colored phenazine compounds.....	94
Figure 4.5: Schematic diagram of the different stages of <i>P. aeruginosa</i> biofilm formation.....	95
Figure 4.6: Phenazine synthesis pathway in <i>P. aeruginosa</i>	97
Figure 4.7: Schematic diagram of the different functions of phenazine compounds produced by bacteria.....	99
Figure 4.8: Schematics of SECM experimental setup	109

Figure 4.9: Bulk phase PYO and pH measurement in presence of planktonic bacteria	112
Figure 4.10: Activation of QS in <i>P. aeruginosa</i> biofilm (5 mm).	112
Figure 4.11: Calibration curve of PYO (6 – 200 μ M range)	114
Figure 4.12: Real time quantitative detection of PYO produced from <i>P. aeruginosa</i> biofilm.....	116
Figure 4.13: Z-direction naturally produced PYO profile above <i>P. aeruginosa</i> biofilm.....	119
Figure 4.14: Z-direction PYO profile above Δ <i>phz</i> biofilm at 25°C and 36°C...120	
Figure 4.15: Comparison of Z-direction oxidized and reduced PYO profile above <i>phz</i> biofilm at 25°C and 36°C.....	121
Figure 4.16: Z-direction oxidized and reduced PYO profile above Δ <i>phz</i> biofilm in presence of excess iron or nitrate.....	123
Figure 4.17: Z-direction oxidized and reduced PYO profile above different mutant of <i>P. aeruginosa</i> biofilm	124
Figure 4.18: Percentage of Fe(II) in the presence of PYO treated biofilms for 1h.126	
Figure 4.19: SECM image of 1 mm wild type <i>P. aeruginosa</i> biofilm	128
Figure 4.20: Proposed model of reduced PYO layer formation	132
Figure 5.1: Real time quantitative detection of peroxide produced by biofilm ..144	
Figure 5.2: Real time spatial mapping of local peroxide produced by polymicrobial (<i>Aa</i> and <i>Sg</i>) biofilm.....	146
Figure 5.3: The schematic diagram of Comsol Multiphysics model used for simulation.....	150
Figure 5.4: Calibration curve for H ₂ O ₂ with concentrations ranging from 0.06 ~1.6 mM in CDM with a <i>Sg</i> biofilm at 37°C.....	152

Figure 5.5: Calibration curve for H ₂ O ₂ over the concentration range from 0.06 ~1.0 mM in CDM with a <i>Sg</i> biofilm at 37°C.....	152
Figure 5.6: Amperometric current of Au UME as a function of time in 0.2 mM H ₂ O ₂ CDM solution at 37°C.	154
Figure 5.7: Current response of 0.6 mM H ₂ O ₂ as a function of time in the presence of a <i>Sg</i> biofilm.....	154
Figure 5.8: Effect of <i>Sg</i> numbers on H ₂ O ₂ detection. 1.0 mL of <i>Sg</i> suspension contain 5×10^8 <i>Sg</i> cells.....	158
Figure 5.9: Confocal laser scanning micrograph of a mixed species biofilm. <i>S. gordonii</i> (red) and <i>Aa</i> (green) were cocultured in a colony biofilm.....	161
Figure 5.10: The simulated (solid line) hydrogen peroxide metabolite efflux from bacterial biofilm of <i>Sg</i> at a distance of 100 μ m from surface compared to experimental measurements (dots). The diameter of the SECM tip used was 25 μ m (RG = 10).....	161
Figure 6.1: The nanoelectrode assembly after being received from nanonics....	171
Figure 6.2: The CV of nanoelectrode 2.3 (19 nm approx.) in presence of 2 mM ferrocene methanol & 0.1 (M) Na ₂ SO ₄	171
Figure 6.3: Electrochemical cleaning of nanoelectrodes	173
Figure 6.4: Effect of electrochemical cleaning and annealing of nanoelectrode on radius.....	174
Figure 6.5: Negative and positive feedback approach curve using nanoelectrode.....	176
Figure 6.6: SECM image of pores of a polycarbonate membrane.....	178
Figure 6.7: Constant height mode SECM image of 200 nm pore polycarbonate membrane place on 2 mm Pt electrode.....	179
Figure 6.8: SECM image of a glass nanopore	180

CHAPTER 1: Introduction to Scanning Electrochemical Microscopy (SECM)

1.1 ULTRAMICROELECTRODE (UME) AS A SECM PROBE

Since the very core of the SECM instrument is the use of an ultramicroelectrode (UME), it is necessary to describe its unique properties to the readers first. There has been tremendous progress in the use of UME's in varying electrochemical systems during the last two decades through the independent works of Wightman, Bard and others (1-9). Typically, an electrode is called an UME when its critical dimension is less or equal to 25 μm in diameter. Even though UME's can be found with differing shapes in the literature we will focus our discussion on disk shaped UME's. One of the advantages of using the UME is low uncompensated resistance and double layer charging, thus allowing one to record much lower concentrations of analytes. Another great advantage of the the UME is its ability to reach steady state in a \sim ms to μs time period, allowing one to determine analyte concentration using the following equation:

$$I_{ss} = 4nFaDC^*$$

Where, n is number of electrons transferred, a is radius of electrode, F is Faraday constant (C/mol), D is diffusion coefficient of the redox couple (cm^2/s), C^* corresponds to concentration of the redox species in the bulk solution (mM or mol/cm^3) and I_{ss} corresponds to tip current (Amp). Since recorded current is proportional to the diffusion coefficient (D) or concentration (C^*), it is possible to determine one parameter if all other parameters are known in the above equation.

Even though the steady state current follows a simple equation the actual diffusion layer calculation for disk UME's is quite complex. Generally the current-time behavior for a UME disk goes through three transitional regimes: (a) short time, (b)

intermediate and (c) a long time regime. Thus, the current-time behavior for the disk UME can be predicted by the following relation:

$$i = \frac{4nFAD_0C_0^*}{\pi r_0} f(\tau)$$

Where, $\tau = 4D_0t/r_0^2$

At short time regime ($\tau < 1$)

$$f(\tau) = 0.88623\tau^{-1/2} + 0.78540 + 0.094\tau^{1/2}$$

At long time regime ($\tau > 1$)

$$f(\tau) = 1 + 0.71835\tau^{-1/2} + 0.05626\tau^{-3/2} - 0.00646\tau^{-5/2} \text{ ----}$$

As clear from the equation above, in the short time regime planar diffusion plays an important role until radial diffusion (edge effect) takes over in the long time regime (Figure 1.1). In the intermediate regime diffusion is complex as it is mixture of both regimes and hence no useful data can be successfully extracted.

One can also represent approximately the UME current-time behavior by the following equation:

$$i = \frac{nFAD_0^{1/2}C_0^*}{\pi^{1/2}t^{1/2}} + 4nFD_0C_0^*r_0$$

The first term in the equation represents the Cottrell equation and the second term represents steady state behavior. In normal operating conditions one can use the very short time regime or semi-infinite condition to study Cottrell behavior or one can use the long-time limit to study the steady state regime. In most cases, SECM operates in a steady state condition to avoid any complications in time-dependent or transient response.

A detailed procedure of SECM tip fabrication can be found in reference (10). Briefly, a high purity (99.99%) metal wire (Goodfellow) of known diameter such as 10 or 25 μm was sealed inside a borosilicate glass capillary (1mm diameter) using an electrically heated coil. While sealing, a vacuum is maintained inside the capillary with aid of a vacuum pump to ensure good sealing. After sealing, the capillary is back-filled with silver epoxy (Epoxy Technologies, catalog number H20E) and a connecting wire and cured for 2-3 hours inside a 120°C oven. The epoxy end of the capillary is then sealed further with “10 minute” epoxy to ensure the connecting wire can withstand mechanical tension. The sealed side was then polished using sand paper of different grain sizes to expose the active metal area. Once exposed the active metal area was then polished with 0.3 and 0.05 μm alumina powder (Buehler, catalog number 40-10075) respectively on a polishing pad (Buehler, catalog number 40-7212).

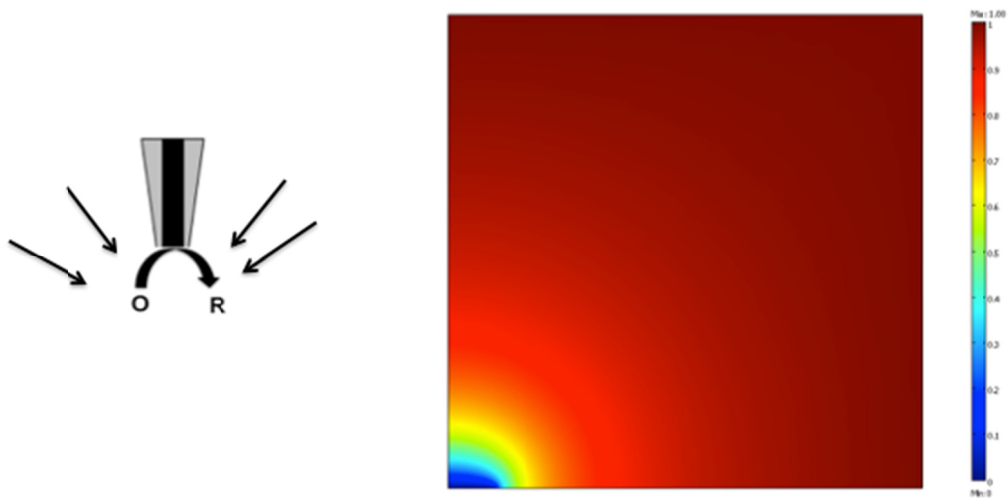


Figure 1.1: Simulated hemispherical diffusion layer of a 10 μm radius ultramicroelectrode (UME).

The simulation model is in axial symmetry coordinates. The blue color represents only the radius of the tip.

1.2 SECM MODES OF OPERATION

SECM consists of a three-electrode (working electrode, counter electrode and reference electrode) electrochemical cell as well as three sets of stepper motors (xyz-micro-positioner). The schematic diagram of a SECM set up is shown in Figure 1.2. The working electrode in the cell is generally used as an electrochemical probe or ultramicroelectrode (UME, diameter $\sim 10 \mu\text{m}$) to monitor and study different electrochemical reactions. The position of the probe or tip is manipulated by xyz-motors, which are controlled by computer. Thus, it is possible to move a tip in three-dimensional space with micrometer or better precision. A typical SECM tip is shown in Figure 1.2. The electroactive metal area is normally made of platinum or gold and is surrounded by an insulating sheath generally composed of glass. The glass portion of the working end of electrode is generally tapered or polished to bring the tip closer to the substrate as shown in Figure 1.2. Another major advantage of SECM is the ability to control the potential of a substrate as well as the working electrode or SECM tip independently with a bipotentiostat.

In a typical SECM experiment all the electrodes including the tip and the substrate are immersed inside a SECM cell containing a redox species. When the tip, held at diffusion-controlled potential, is brought close to the substrate two possible response can be observed: a) the redox species at the tip is blocked by the insulating substrate b) the redox species at the tip is regenerated by a conducting substrate. In the first case, a decrease in tip current has been observed whereas an increase in tip current is observed for the latter conducting substrate due to regeneration of redox species by the substrate. These tip current vs. tip-substrate distance curves are called approach curves in SECM nomenclature. When an approach curve is performed over an insulator it is called a negative feedback approach curve (Figure 1.3 A & B) and when performed over a conducting substrate it is called a positive feedback approach curve (Figure 1.3 C & D).

The curves are generally plotted as normalized current vs. normalized distance. The current is normalized against the tip current recorded far away from the substrate, which is generally ten times the radius of the tip. The distance is normalized against tip radius. Henceforth, the curves are independent of tip radius, diffusion coefficient of redox species and concentration of redox species present in the solution. In addition, a positive feedback approach curve is observed to be insensitive to the RG (the ratio of outside glass diameter to metal disk diameter) of the tip and is generally observed at a comparatively close distance to the substrate. Since the negative feedback approach curve occurs due to the blocking of redox species, the current-distance curve profoundly depends on the RG of the tip. Thus, with the aid of a negative feedback approach curve it is possible to determine electrochemically the diameter of an outside glass sheath.

Since SECM approach curves are performed at steady state experimental conditions, one can simulate the same set of approach curves with the aid of a finite element method to obtain theoretical current-distance relationships. Corresponding theoretical negative and positive feedback equations are as follows:

For an insulating substrate

$$I_T = [0.292 + 1.5151/L + 0.6553 \exp(-2.4035/L)]^{-1}$$

For a conducting substrate

$$I_T = 0.68 + 0.78337/L + 0.3315 \exp(-1.0672/L)$$

Hence, by fitting the experimental curves with the theoretical approach curves, one can determine the exact distance between the tip and substrate.

There are many reports of different modes of operation for SECM. Here we will confine our discussion on the two most popular mode of operations (a) feedback mode and (b) generation collection mode. Detailed reports about other modes of operation can be found elsewhere (10).

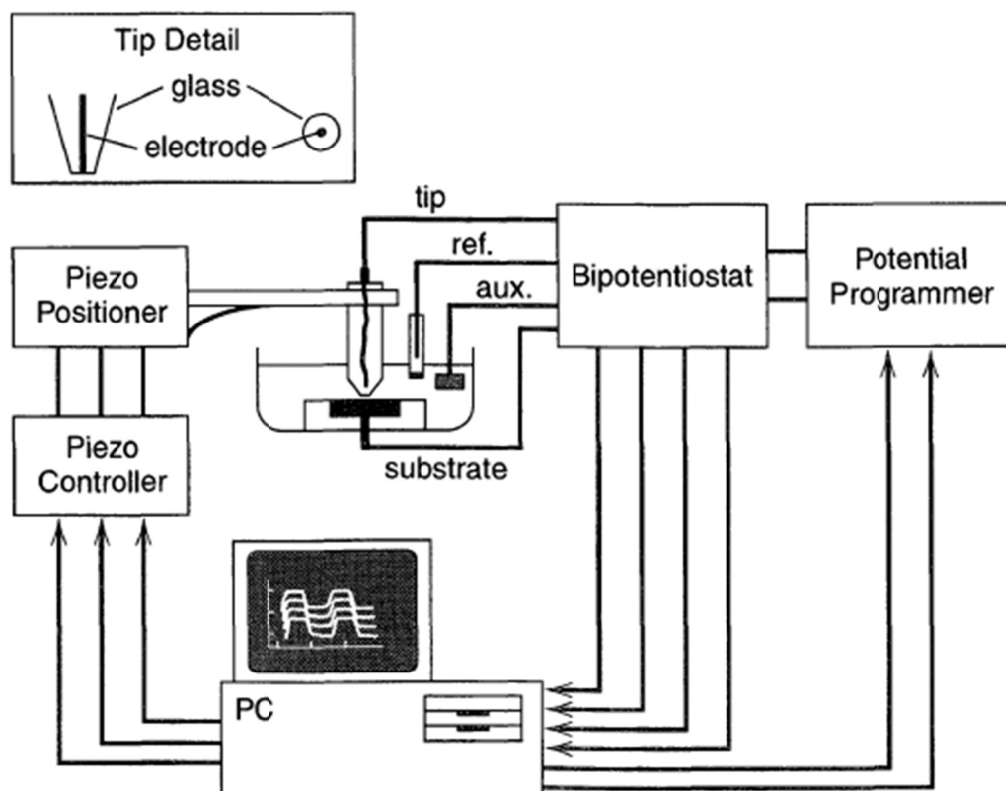


Figure 1.2: Schematic diagram of a Scanning Electrochemical microscope (SECM) setup.

(Inset) Electrochemical probe or glass enclosed electrode used as a SECM tip. Typical diameter of the active metal area is ~ 10 to $25 \mu\text{m}$. (Adapted from reference 11)

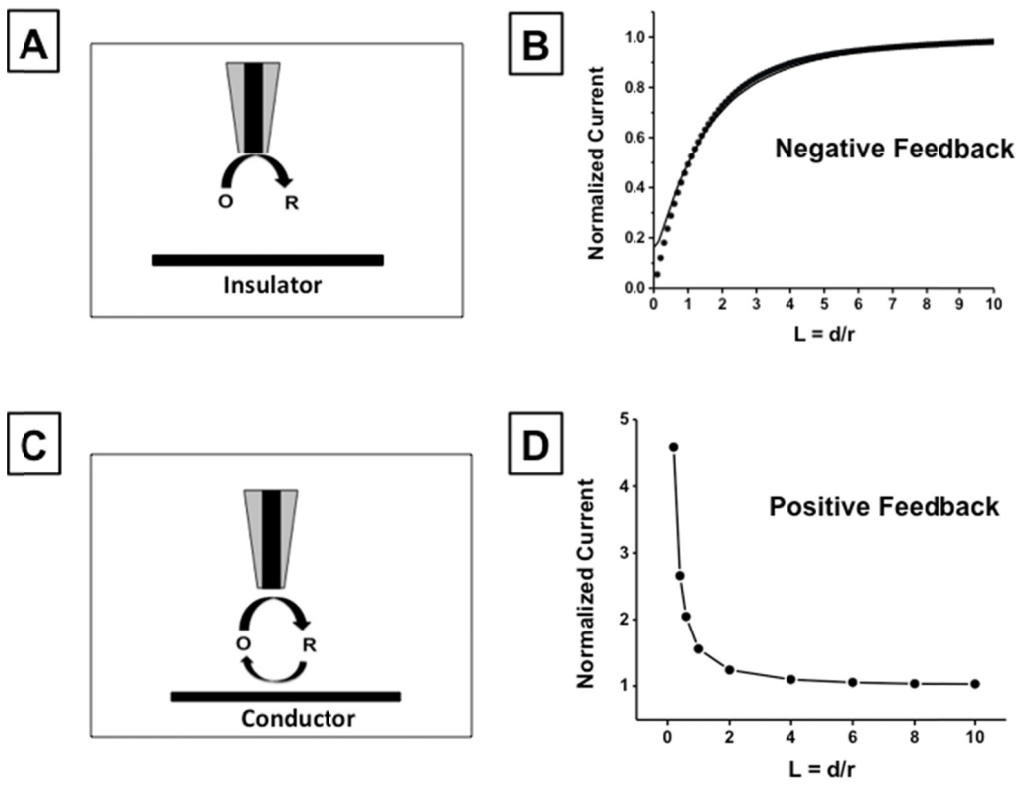


Figure 1.3: Negative and positive feedback approach curves in SECM

(A) Schematic diagram of the SECM negative feedback mode of operation (B) Typical negative feedback mode approach curve (C) Schematic diagram of the SECM positive feedback mode of operation. (D) Theoretical positive feedback mode approach curve.

Feedback Mode

In feedback mode the tip is generally held at diffusion controlled potential and brought close to the substrate of interest. Depending on the nature of the substrate the tip can sense the feedback by the increase or decrease of current. The increase in tip current in comparison to I_{ss} (tip current in bulk solution) is called positive feedback mode and a decrease in tip current is called negative feedback mode. If a tip is scanned over an insulating substrate with topographical features the tip current decrease is due to blocking of redox species in the solution. As a result, current-distance (x-direction scan) curves follow the topographical features of the substrate. Negative feedback mode SECM imaging is also very useful in determining a topographical feature, which is not electroactive or does not give feedback such as a living cell. For example, in Figure 1.4 A & B below it is shown how SECM negative feedback mode was used to determine topographical features of a single living HeLa cell located on a Petri dish.

Similar topographical features can also be mapped with the aid of SECM operating in positive feedback mode. In this case, higher current compared to I_{ss} , is observed when moved over the substrate of interest. Thus, this contrast of high and low current can also be used to obtain an electrochemical image as shown in Figure. 1.4 C & D. Since the positive feedback mode gives a sharp contrast between the current over the substrate and the background, generally a better quality of SECM electrochemical image can be obtained in this mode.

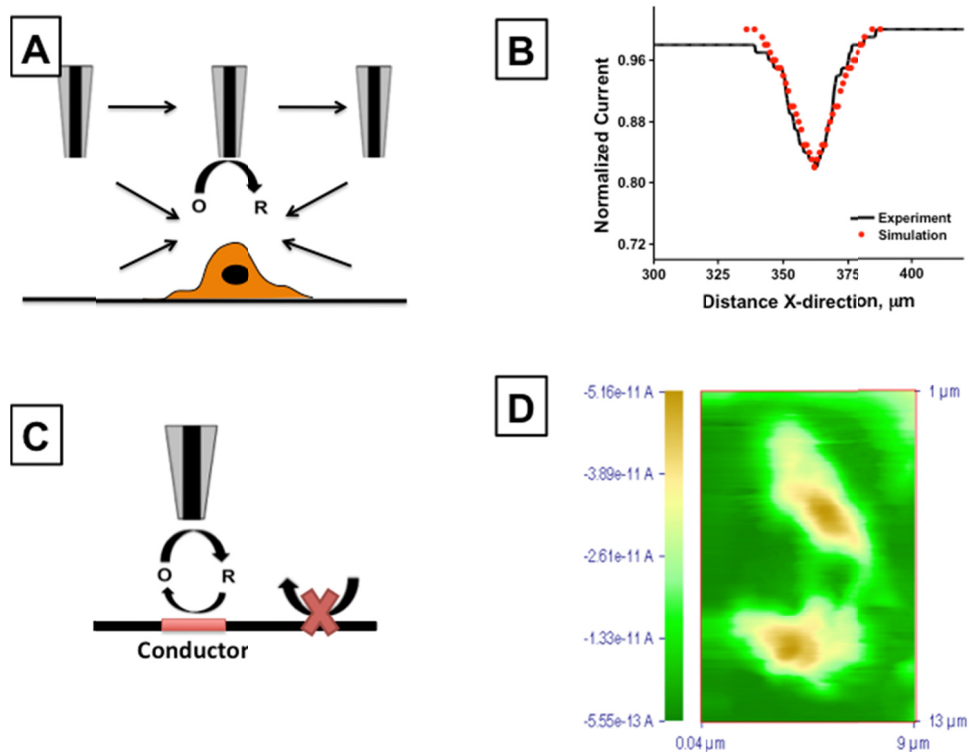


Figure 1.4: SECM feedback modes of operation.

(A) Schematics of a SECM tip moving over a single live cell in negative feedback mode. (B) X-direction scan showing the topographical features of a live cell. The height of the cell was determined to be $10 \mu\text{m}$. (C) Schematic diagram of a SECM positive feedback mode of operation. (D) SECM image of a polyester membrane obtained in positive feedback mode. Pore diameter: $1 \mu\text{m}$. Tip diameter: $1.5 \mu\text{m}$ Pt. Scan speed: $2.39 \mu\text{m}/\text{sec}$. The membrane was placed over a 2mm Pt electrode.

Generation–Collection Mode

In generation-collection mode the SECM generally operates in two different modes (i) TG/SC (Tip generation-Substrate collection) (ii) SG/TC (Substrate generation-Tip collection) (Figure 1.5). Each of these modes has its own advantages and disadvantages in operation. In TG/SC mode, the tip is held at a fixed potential to produce new electroactive species and the substrate is held at the potential where it can collect the tip-generated species. In TG/SC mode, since a large substrate is used compared to tip size, almost 100% collection of the electrogenerated species is possible. Whereas, in SG/TC mode, the substrate generates the electroactive species, which is collected by the tip located at a certain known distance. The collection efficiency of the tip greatly depends on the tip-substrate distance and each system needs to be calibrated separately before concluding any kinetic parameters or other measurements. One has to be very careful as neither of the generation-collection modes can be used to determine the distance between tip and substrate. So, for all practical purposes an approach curve is done first allowing the tip to be fixed at a certain distance and then the experiment is switched to generation-collection mode to study the system of interest. In most biology related SECM experiments, SG/TC mode is used to detect and quantify electroactive species generated by cells (acting as a substrate). The tip is generally located 10 to 80 μm away from the sample. SG/TC mode can also be used to image a live cell to map the molecules of interest and thus identify a “hot spot” of molecules being generated.

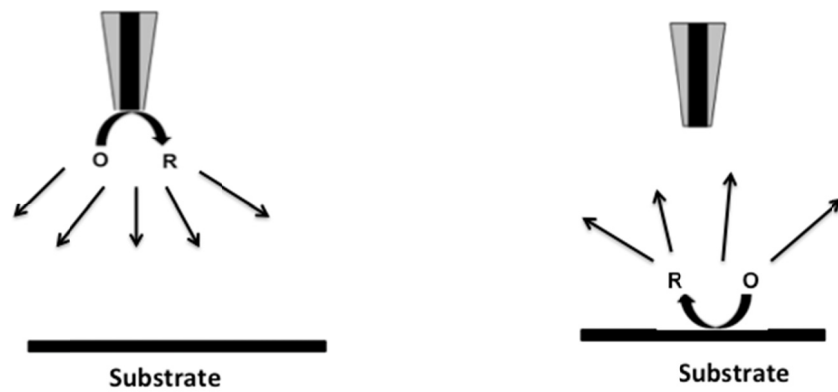


Figure 1.5: SECM generation-collection mode of operation.

(Left) Tip generation and substrate collection (TG/SC) mode *(Right)* Substrate generation-tip collection (SG/TC) mode of operation.

1.3 SECM STUDIES WITH LIVING CELLS

Since its early inception in electrochemical studies, SECM has been applied to a wide variety of fields such as biology, material science, semiconductors etc. (12-14). However in this dissertation, we will confine our discussion about the applications of SECM to studying biological systems.

One of the SECM based multidrug resistance (MDR) study with live and intact liver cancer cells were first reported by Mauzeroll et al. (15,16). Menadione added to hepatocytes can pass through the cell membrane due to its hydrophobic nature. Once inside the cells, it generates reactive oxygen species (ROS) and hydroxyl radicals, which are extremely toxic to the cells. To protect the cell from oxidative stress, glutathione present inside the cell conjugates with menadione in the presence of a GS-transferase enzyme to produce a menadione-glutathione conjugate or thiodione. Thiodione, being too hydrophilic, cannot be transported by passive transport to the extracellular environment. However, thiodione is recognized by an MDR pump due to its glutathione moiety and hence pumped out by the cells with the aid of an ATP-driven GS-X pump. SECM has been used to detect thiodione pumping out of the cell by bringing the tip (10 μm Pt) close to the cells (around 80 μm from cell surface). Selective detection of thiodione in the presence of menadione is achieved because thiodione showed a unique oxidation peak at 0.74V (vs NHE). Glutathione is not electroactive in this potential window at the Pt electrode. However, menadione and thiodione both exhibit two-electron reduction at -0.1V (vs. NHE). The $E^{1/2}$ of thiodione is only 150 mV more negative than menadione. Thiodione pumped out by a monolayer of cells is measured to be 80 μM after addition of 80 μM of menadione. The thiodione flux is reported to be $4.7 \pm 0.3 \times 10^{-12}$ mol/cm²/sec for a highly confluent monolayer of cells. The flux of each cell is 1×10^{-17} mol/cell/sec or 6×10^6 molecules/cell/sec. SECM-based electrochemical imaging of hepatocytes pumping out thiodione is shown in Figure 1.6.

A doxorubicin-mediated MDR phenomenon was also studied in a Chinese Hamster ovarian cancer cell line (17). A carbon fiber UME was used to detect very low concentration (~ 1 nM) of doxorubicin effluxed out of a single living cell previously loaded with doxorubicin. However in this case the UME was brought in close proximity to the cells by aid of an optical microscope. Electrochemical cleaning and adsorptive pre-concentration were used to detect the low drug concentration with temporal resolution.

Besides studying mammalian cells SECM has also been used to study behavior of different bacteria in presence of diverse antimicrobial agents such as silver. Because of the widespread usage of silver in treating microbial infections in wound bandages it is important to study the effects of silver on microbes to determine the mechanism by which silver kills or disables different bacteria. The inhibitory effect of Ag^+ on the respiratory chain of *Escherichia coli* was studied electrochemically by Katherine et al. (18). Respiration was monitored by measuring bulk oxygen concentration in the presence of $\sim \mu\text{M}$ Ag^+ concentration using a Clark ultramicroelectrode. $1 \mu\text{M}$ Ag^+ was reported to be sufficient to uncouple the respiratory chain causing an increase in oxygen uptake by *E. coli* followed by complete cessation of oxygen respiration by bacteria. Ag^+ uptake was measured by peak height of stripping voltammetry using a $25 \mu\text{m}$ Pt UME. SECM was used to quantify the silver uptake and efflux from a monolayer of immobilized *E. coli* on a glass slide. It was reported that approximately 60% of the Ag^+ uptake was intracellular and the remaining 40% resided on the bacterial cell wall.

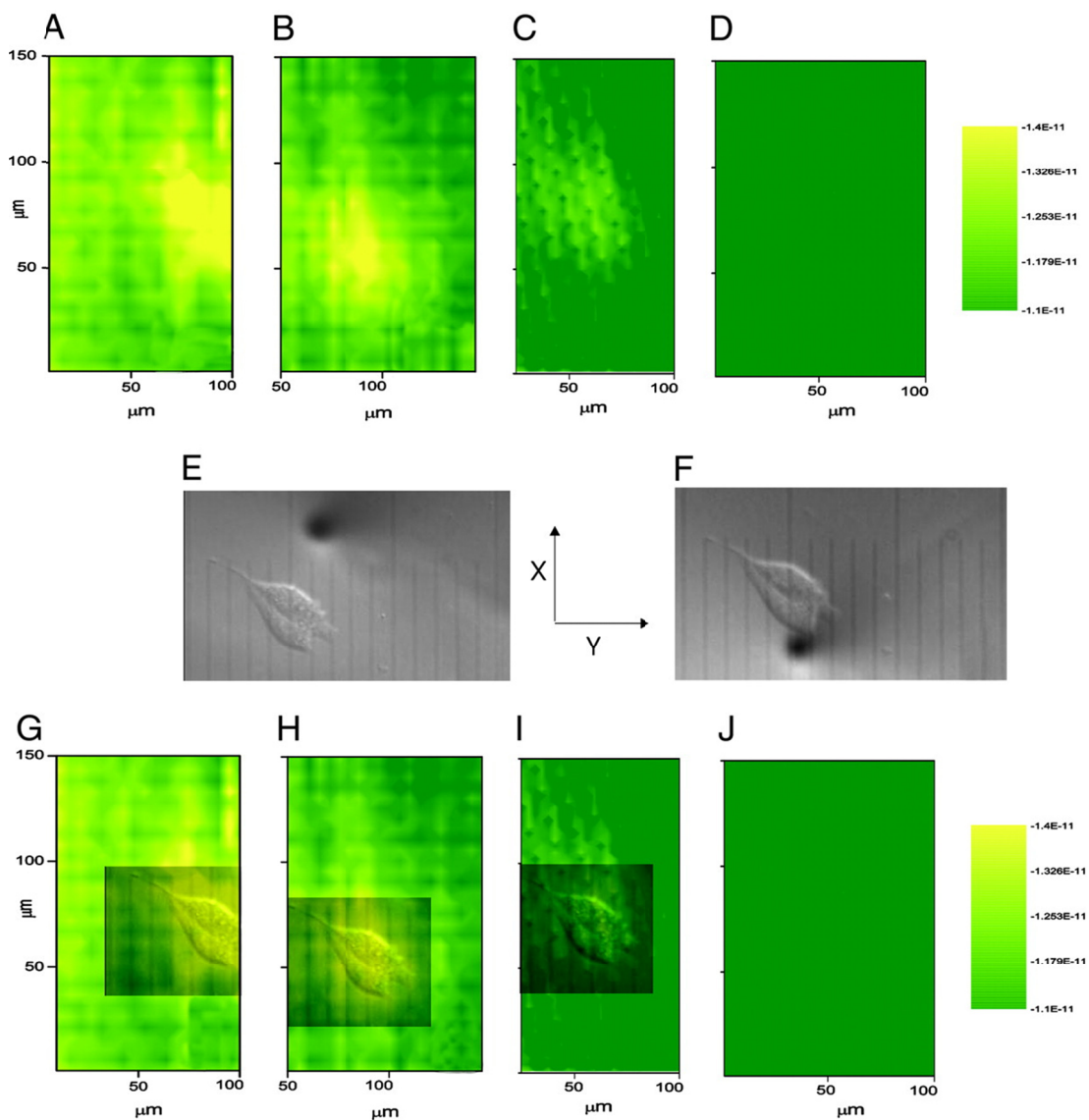


Figure 1.6: SECM image of thiodione transport from a single living cell

(A–D) Time-dependent SECM imaging of thiodione transport by two adjacent cells. Images were obtained in substrate generation-tip collection mode (SG/TC). (E and F) Optical images of the cell. (G–J) Superimposed optical micrograph on the SECM image. The tip potential: + 0.55 V vs. Hg/Hg₂SO₄ and scanned at 150 μm/sec. (Adapted from reference 16)

Besides solid metal electrodes of gold and platinum, metal electrodes in a liquid-liquid interface based pipette can also be used as a SECM tip; also known as ITIES Tip (interface between two immiscible electrolyte solutions, also called a liquid/liquid (L/L) or water/oil (W/O) interface). Recent studies by Zhan et al. (19) have shown that this ITIES tip can be used in SECM to study the toxicity of Ag⁺ uptake by fibroblast cells. A calixarene-based Ag⁺ ionophore (IV) was dissolved in 1,2-dichloroethane to make a liquid-liquid interface inside a micrometer sized glass pipette or ITIES tip. Local micromolar Ag⁺ concentrations thus can be monitored by this ITIES based SECM tip giving a unique opportunity to monitor the Ag⁺ uptake but also give spatial information about Ag⁺ distribution above the fibroblast cells.

The ITIES based SECM tip was further extended to study the Ag⁺ uptake of both fibroblasts as well as *E. coli* (20). It has been reported that the Ag⁺ uptake was enhanced for both *E. coli* as well as fibroblasts in presence of a known potassium ion channel blocker, 4-aminopyridine (4-AP). This observation is important in the light that silver acts as an antimicrobial and suggests that 4-AP can be added along with Ag⁺ to enhance its effectiveness. Ag⁺ uptake was monitored by SECM using an Ag⁺ ion-selective electrode (Ag⁺-ISE) as an electrochemical probe. The internal solution of the ITIES pipette tip (Ag⁺-ISE) contained 5 mM silver ionophore IV and 5 mM bis(triphenylphosphoranylidene) ammonium tetrakis (4-chloro- phenyl) borate (BTTPATPBCl) dissolved in 1,2-dichloroethane (DCE). For mammalian cells the Ag⁺ uptake was increased to 1.0×10^8 ions/cell/sec in presence of 4mM 4-AP in comparison to 0.47×10^8 ions/cell/sec without any blocker. For *E. coli* Ag⁺ uptake was reported to be 5.9×10^4 ions/cell/sec in presence of 1mM 4-AP in comparison to 1.5×10^4 ions/cell/sec without any blocker.

Other interesting SECM applications in studying different biological systems can be found in references (21-25).

1.4 SQUARE WAVE VOLTAMMETRY (SWV)

Since chapter 4 deals with square wave voltammetry to detect pyocyanin, it is appropriate to introduce the concept here. Square wave voltammetry (SWV) was first invented by Ramley and Krause and later developed by Osteryoungs. SWV has the advantages of lower background and greater sensitivity besides its diagnostic aspects to interrogate products by reverse pulse voltammetry. As a result low detection limits can be achieved besides giving diagnostic information similar to Cyclic Voltammetry (CV). The schematic of the applied waveform and the corresponding current recorded by an electrode are shown in Figure 1.8. The square wave is characterized by pulse width (t_p) and pulse height (ΔE). SWV frequency is defined as $f = 1/2t_p$. If ΔE_s is the increment in pulse potential, the corresponding scan rate can be calculated from $v = \Delta E_s/2t_p = f * \Delta E_s$. Currents are recorded at the end of each forward and reverse pulse period. A difference of forward (i_f) and reverse (i_r) current is calculated and plotted with respect to potential. Since the forward and reverse current have diagnostic data, they are also stored separately. Thus, SWV gives us three sets of data: forward scan, reverse scan and the difference of the two.

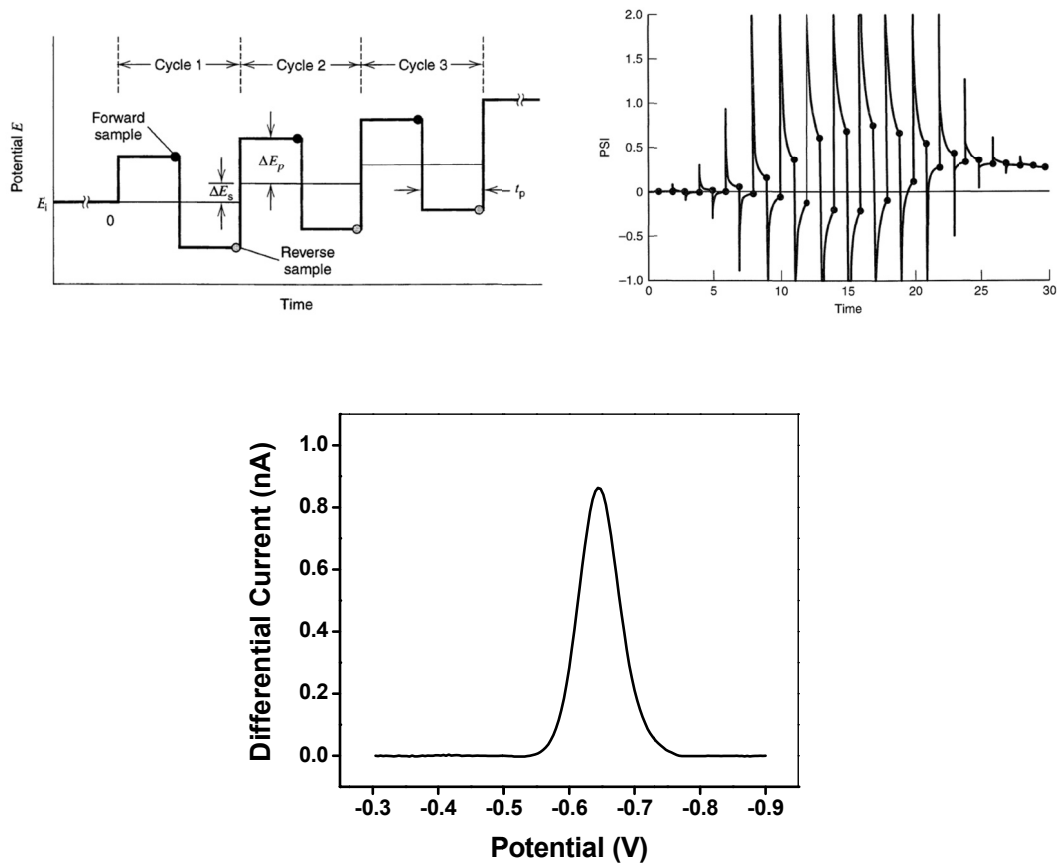


Figure 1.7: Square wave voltammetry

(*Top Left*) Schematic representation of the potential wave. (*Top Right*) Current recorded after each pulse. (*Bottom*) Typical square wave voltammogram. (Adapted from reference 26)

1.5 REFERENCES

- ¹ Adams KL, Puchades M, Ewing AG (2008) In Vitro Electrochemistry of Biological Systems. *Annu. Rev. Anal. Chem. (Palo Alto, Calif.)* 1:329.
- ² Adams RN (1976) Probing brain chemistry with electroanalytical techniques. *Anal. Chem.* 48:1126A-1138A.
- ³ Feng JX, Brazell M, Renner K, Kasser R, Adams RN (1987) Electrochemical pretreatment of carbon fibers for in vivo electrochemistry: effects on sensitivity and response time. *Anal. Chem.* 59:1863-1867.
- ⁴ Wightman RM (1991) Temporally Resolved Catecholamine Spikes Correspond to Single Vesicle Release from Individual Chromaffin Cells. *Proc. Natl. Acad. Sci. U.S.A.* 88:10754-10758.
- ⁵ Montenegro, M.I., Queir'os, M.A., Daschbach, J.L. (Eds.), (1991) *Biological Systems in Microelectrodes: Theory and Applications*. (Kluwer Academic Publishing, Dordrecht) pp. 453–462.
- ⁶ Bard AJ ed. (2007) *Encyclopedia of Electrochemistry* (Wiley-VCH Verlag GmbH & Co. KGaA, Weinheim, Germany).
- ⁷ Cooper, J.M., Jung, S.-K., 2001. In: Bard, A.J., Stratman, M., Wilson, G.S. (Eds.), *Encyclopedia of Electrochemistry*, vol. 9. Wiley-VCH, pp. 31–49.
- ⁸ Gao N, Zhao M, Zhang X, Jin W (2006) Measurement of enzyme activity in single cells by voltammetry using a microcell with a positionable dual electrode. *Anal. Chem.* 78:231-8.
- ⁹ Cannon DM, Winograd N, Ewing AG (2000) Quantitative chemical analysis of single cells. *Annu. Rev. Biophys.* 29:239-63.
- ¹⁰ Bard AJ, Mirkin MV, eds. (2001) *Scanning Electrochemical Microscopy* (Merzel Dekker, New York).

- ¹¹ Bard AJ, Denuault G, Lee C, Mandler D, Wipf DO (1990) Scanning electrochemical microscopy - a new technique for the characterization and modification of surfaces. *Acc. Chem. Res.* 23:357-363.
- ¹² Amemiya S, Guo J, Xiong H, Gross D a (2006) Biological applications of scanning electrochemical microscopy: chemical imaging of single living cells and beyond. *Anal. Bioanal. Chem.* 386:458-71.
- ¹³ Amemiya S, Bard AJ, Fan F-RF, Mirkin MV, Unwin PR (2008) Scanning Electrochemical Microscopy. *Annu. Rev. Anal. Chem.* (2008) 1:95-131.
- ¹⁴ Bard AJ, Li X, Zhan W (2006) Chemically imaging living cells by scanning electrochemical microscopy. *Biosens. Bioelectron.* 22:461-72.
- ¹⁵ Mauzeroll J, Bard AJ (2004) Scanning electrochemical microscopy of menadione-glutathione conjugate export from yeast cells. *Proc. Natl. Acad. Sci. U.S.A.* 101:7862-7.
- ¹⁶ Mauzeroll J, Bard AJ, Owhadian O, Monks TJ (2004) Menadione metabolism to thiodione in hepatoblastoma by scanning electrochemical microscopy. *Proc. Natl. Acad. Sci. U.S.A.* 101:17582-7.
- ¹⁷ Lu H, Gratzl M (1999) Monitoring drug efflux from sensitive and multidrug-resistant single cancer cells with microvoltammetry. *Anal. Chem.* 71:2821-30.
- ¹⁸ Holt KB, Bard AJ (2005) Interaction of silver(I) ions with the respiratory chain of *Escherichia coli*: an electrochemical and scanning electrochemical microscopy study of the antimicrobial mechanism of micromolar Ag⁺. *Biochemistry* 44:13214-23.
- ¹⁹ Zhan D, Li X, Zhan W, Fan F-RF, Bard AJ (2007) Scanning electrochemical microscopy. 58. Application of a micropipet-supported ITIES tip to detect Ag⁺ and study its effect on fibroblast cells. *Anal. Chem.* 79:5225-31.
- ²⁰ Zhan D, Fan F-RF, Bard AJ (2008) The Kv channel blocker 4-aminopyridine enhances Ag⁺ uptake: a scanning electrochemical microscopy study of single living cells. *Proc. Natl. Acad. Sci. U.S.A.* 105:12118-22.

- ²¹ Li X, Bard AJ (2009) Scanning electrochemical microscopy of HeLa cells – Effects of ferrocene methanol and silver ion. *J. Electroanal. Chem.* 628:35-42.
- ²² Sun P et al. (2008) Nanoelectrochemistry of mammalian cells. *Proc. Natl. Acad. Sci. U.S.A.* 105:443-8.
- ²³ Gonsalves M et al. (2000) Scanning electrochemical microscopy as a local probe of oxygen permeability in cartilage. *Biophys. J.* 78:1578-88.
- ²⁴ Liu B, Rotenberg SA, Mirkin MV (2000) Scanning electrochemical microscopy of living cells: different redox activities of nonmetastatic and metastatic human breast cells. *Proc. Natl. Acad. Sci. U.S.A.* 97:9855-60.
- ²⁵ Kaya T, Torisawa Y-suke, Oyamatsu D, Nishizawa M, Matsue T (2003) Monitoring the cellular activity of a cultured single cell by scanning electrochemical microscopy (SECM). A comparison with fluorescence viability monitoring. *Biosens. Bioelectron.* 18:1379-83.
- ²⁶ Bard, A. J. & Faulkner, L. R. (2001) *Electrochemical Methods* (Wiley, New York), 2nd Ed., p. 294-296.

CHAPTER 2: Effects of Triton X-100 on Membrane Permeability of a Single HeLa cell as Studied by SECM

ABSTRACT

Changes in HeLa cell morphology, membrane permeability, and viability caused by the presence of Triton X-100 (TX100), a nonionic surfactant, were studied by scanning electrochemical microscopy (SECM). No change in membrane permeability was found at concentrations of 0.15 mM or lower during an experimental period of 30 to 60 min. Permeability of the cell membrane to the otherwise impermeable, highly charged hydrophilic molecule ferrocyanide was seen starting at concentrations of TX100 of about 0.17 mM. This concentration level of TX100 did not affect cell viability. Based on a simulation model, the membrane permeability for ferrocyanide molecules passing through the live cell membrane was $6.5 \pm 2.0 \times 10^{-6}$ m/s. Cells underwent irreversible permeabilization of the membrane and structural collapse when the TX100 concentration reached the critical micelle concentration (CMC), in the range of 0.19 to 0.20 mM. The impermeability of ferrocyanide molecules in the absence of surfactant was also used to determine the height and diameter of a single living cell with the aid of the approach curve and probe scan methods in SECM.

2.1 INTRODUCTION

Detergents are widely used in biology for protein extraction from cell membranes, in the crystallization of proteins, as stabilizing and denaturing agents, and as membrane permeabilizing agents. Triton X-100 (TX100) is one of the most widely used nonionic surfactants for lysing cells to extract protein and other cellular organelles or to permeabilize the living cell membrane for transfection (1–3). However, if large amounts are added or the cells are subject to prolonged exposure to TX100, the cells die (4–7). This toxicity of TX100 molecules arises because of the disrupting action of its polar head group on the hydrogen-bonding present within the cell's lipid bilayer, leading to the destruction of the compactness and integrity of the lipid membrane. The insertion of detergent monomer into the lipid membrane begins at low concentrations. This leads to a disruption of cellular structure and eventual overpermeabilization of the cell membrane at concentrations above the critical micelle concentration (CMC) from the bilayer–micelle transition. Because cell viability is extremely sensitive within a narrow range of surfactant concentrations, especially near LD_{50} , controlling the TX100 concentration for transfection, e.g., the introduction of hydrophilic species without damaging cells, is difficult. Moreover, cholesterol or similar molecule-rich membrane domains are reported to be more tolerant toward detergents such as TX100 molecules in comparison to other parts of the lipid bilayer. (8–14).

Scanning electrochemical microscopy (SECM) has found increasing application in recent years to the study of living cells as well as biological systems in general (15). A number of studies have dealt with the permeability of redox species into the live cell. These have shown that highly charged hydrophilic molecules such as $Ru(CN)_6^{4-}$, $Ru(NH_3)_6^{3+}$, $Fe(CN)_6^{4-}$, and $Fe(CN)_6^{3-}$, as well as ferrocene carboxylate, cannot penetrate the intact cell membrane while hydrophobic molecules such as menadione, 1,2-naphthaquinone and MV_2^+ can. Thus while the molecules ferrocene methanol and

tetramethyl-*p*-phenylenediamine (TMPD) show positive feedback behavior in SECM, signaling reduction of the oxidized form from interacting with the cell, molecules such as $\text{Co}(\text{bpy})_3^{2+}$ and $\text{Co}(\text{phen})_3^{2+}$, show negative feedback over live HeLa cells. Redox molecules inside the cell have also been shown to exchange electrons with redox molecules outside the membrane in the solution (16). SECM has also been used to find the local permeability of an isolated *Xenopus* oocyte nucleus for redox molecules as $>9.8 \times 10^6$ molecules/Nuclear. Pore Complex (NPC)/s (17). Fully automated time lapse SECM monitored single Hep G2 cell topography in the presence of antifreeze proteins over a period of 8 h at 4 °C (18). SECM has also been used in the induced transfer mode to measure the permeability of MV^{2+} through bovine articular cartilage, while topographic information was obtained with the membrane impermeable to $\text{Ru}(\text{CN})_6^{4-}$ as a redox mediator (19). Heterogeneity in the permeability of oxygen across cartilage has also been observed by SECM imaging especially near the μm -size cellular and pericellular domain (20).

Although there have been many quantitative studies of the TX100 molecule and its interaction with artificial lipid bilayers (21–25), there have been none with a living cell membrane and its behavior in terms of its permeability, morphology, and metabolic behavior in real time. We report here how the single live cell permeability and morphology are affected by TX100, the most commonly used surfactant for permeabilization in many fluorescent and toxicological studies. Most modern studies are based on fluorescent tagging of antibodies in which one of the essential steps involved is to permeabilize the cell membrane by a surfactant to access the cellular interior targeted by the antibody fluorescent tag. Yet little is known about what happens to the cell when its membrane is permeabilized. Moreover, almost all the studies have been designed to show the permeability of redox species, but there are no reports on the effect of nonelectroactive species on cellular permeability. In this work we provide quantitative

data on the permeability of the cell membrane in the presence of nonelectroactive molecules like TX100 as well as how this permeability actually affects the hydrophobicity of the cellular membrane.

2.2 MATERIALS AND METHODS

Chemicals

All of the chemicals were used as received. $K_4[(Fe(CN)_6)] \cdot 3H_2O$, $MgSO_4$, $CaSO_4$ and K_2SO_4 were obtained from Fisher Scientific. D-glucose, HEPES and TX100 (T 9284) were from Sigma-Aldrich. All solutions were made with 18 M Ω Milli-Q (Millipore) reagent water.

Cell Culture

HeLa cells were purchased from ATCC (catalog number CCL-2) and cultured as per instructions provided by ATCC. In brief, cells were grown and maintained in “ATCC-formulated Eagle’s Minimum Essential Medium” (ATCC 30-2003) culture medium supplemented with 10% fetal bovine serum (ATCC 30-2020) on tissue culture Petri dish (Falcon 353801). Temperature was maintained at 37 °C in a water-jacketed incubator (model 2310, VWR Scientific) with 95% air and 5% CO₂.

Cell coverage of about 50% on the Petri dish was used in all the experiments. When appropriate cell coverage was obtained, the dish was taken out of the incubator and the cells were washed with buffer solution (10mM HEPES, 5.55 mM glucose, 75 mM Na₂SO₄, 1 mM MgSO₄ and 3 mM K₂SO₄) twice and then incubated with 1 mL of buffer solution at room temperature for 1 h. The buffer solution was then replaced by the appropriate experimental solution prepared with buffer.

Fluorescent Based Viability Assay

The fluorescent-based viability assay kit (Biotium Inc.) was used to detect living and dead cells simultaneously in the sample. This assay employs two dyes, calcein AM (green dye) and EthD-III (red dye). Calcein AM has the ability to pass through an intact cell membrane and react with the intracellular enzyme esterase, which converts it into an intensely green fluorescent calcein dye (excitation/emission 495 nm/515 nm). The polyanionic calcein dye remained confined inside intact cell membranes so the living cells were easily visible through an inverted microscope (Eclipse TE300 Nikon Inverted Microscope, Melville, NY). EthD-III could permeate only through damaged membranes and reacted with intracellular nucleic acid to emit intense red fluorescence inside dead cells (excitation/ emission 530 nm/635 nm). This assay was very useful for detecting both live and dead cells at the same time without any pretreatment of the samples. In this work, 1 mL of 2 μ M calcein AM and 4 μ M EthD-III was used to detect the viability of the cells either without, or in presence of, different concentrations of TX100 for different periods of time. The green and red stained cell photos were then processed by Image J software (available from the NIH website) to count the number of live and dead cells.

SECM Experiments

Electrochemistry and Electrode Fabrication

Ultramicroelectrodes (UME) of 10 μ m diameter platinum wire disks (Goodfellow Cambridge Limited, UK) were used in the experiments. Detailed steps for fabrication and characterization have been reported elsewhere (15). 0.5 mm Pt wire (Goodfellow Cambridge Limited, UK) and Hg/Hg₂SO₄ (Radiometer, Copenhagen) were used as counter and reference electrodes respectively. All potentials reported here were referred to Hg/Hg₂SO₄. The SECM (model 900B, CH Instruments, Austin, TX) was used for all electrochemical experiments.

X-scan Over Single Cell Experiment

HeLa cells were cultured in approximately one 1 cm spot on the Petri dish inside the incubator until the cell coverage was about 50%. The cells were washed with buffer solution twice and then incubated with buffer solution for 1–2 h at room temperature. During that time period the Petri dish with cells, tip, reference electrode, and counter electrode were set up on a SECM stage as shown in Figure 2.1. The buffer-only solution was then replaced by a 4 mM ferrocyanide solution prepared with the same buffer. Approach curves were obtained at 0.5 V at three different points outside the cellular spot to adjust the tilt of the SECM stage. Tip-substrate (Petri dish) distance, as shown in Figure 2.1, was determined by negative feedback approach curve using Fe(II)/Fe(III) as redox couple (Figure 2.2 A and B). The HeLa cells were then located by constant height (16–20 μm) SECM imaging with ferrocyanide as redox mediator at 0.5 V (Figure 2.2C). The location of a single cell in the x-y direction was then narrowed down by x and y scanning of the tip at a fixed height ($\sim 16 \mu\text{m}$) and potential (at 0.5 V) over the cell at a speed of 5 $\mu\text{m/s}$. No TX100 was added to the cells at this time. After identifying a cell, the 4 mM redox solution was then replaced by a solution containing different concentrations of TX100 along with 4 mM ferrocyanide. An x-direction scan was then carried out over that particular single cell several times.

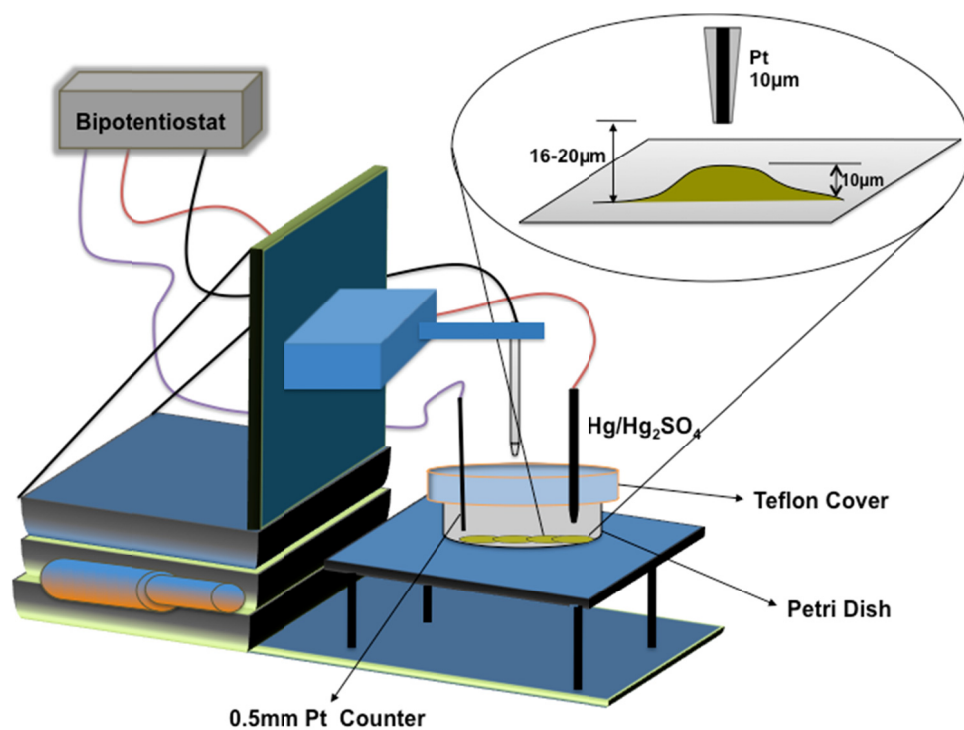


Figure 2.1: Experimental setup for SECM experiment.

The tip used was 10 µm Pt (RG = 5). Counter and reference electrode was 0.5 mm Pt wire and Hg/Hg₂SO₄ respectively.

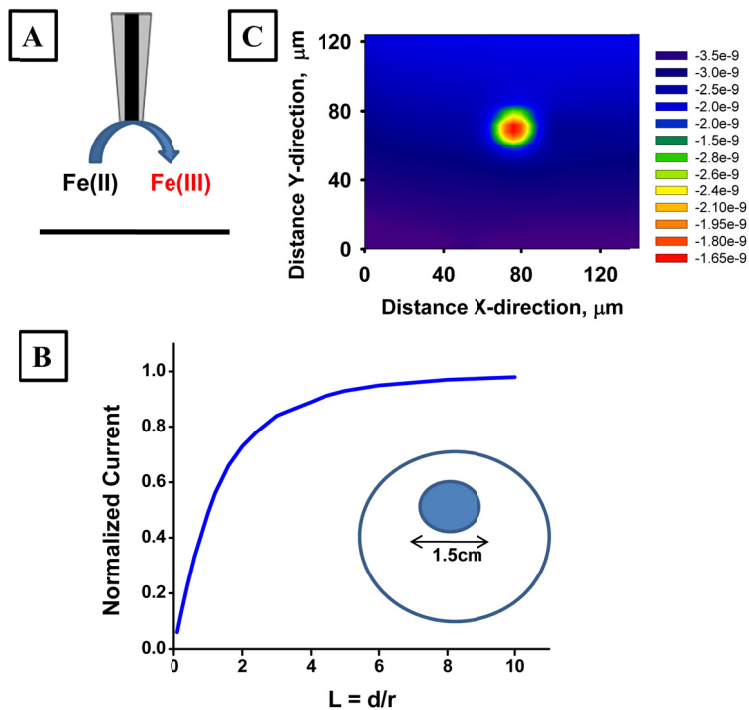


Figure 2.2: Topographical SECM image of a single HeLa cell

(A and B) 4 mM ferrocyanide was used as redox couple to perform the negative feedback approach curve on the Petri dish. (Inset) HeLa cells were cultured in a 1.5 cm spot on a Petri dish. (C) SECM image of a single living HeLa cell (red circle). Lower current (red color) over the cell signifies the cell was sticking out of the dish. Cells were found and identified by SECM image at a constant height of 16 μm away from dish and at +0.5 V potential vs. $\text{Hg}/\text{Hg}_2\text{SO}_4$ in presence of 4 mM of ferrocyanide in HEPES buffer (as described in cell culture subsection).

Approach Curve Over Single Cell Experiment

The method was nearly identical to that above. In brief the cells were found by SECM imaging and then the x-y scan was zoomed in for higher resolution. The tip was then moved above a cell and an approach curve was done at 0.5 V over the single cell with 4 mM ferrocyanide only in the solution to obtain topographic information. The redox solution then was replaced by different concentrations of TX100 and 4 mM ferrocyanide solution and approach curve experiments were performed over the cell for different periods of time.

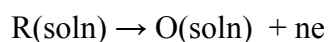
I-t Experiment Over Single Cell

The cells were first put on the SECM stage and approach curve and x-scan experiments were performed with redox mediator only in solution as described previously. The 10 μm Pt tip was then held at a constant height ($\sim 5 \mu\text{m}$ above the highest point of the cell) and current was recorded at a constant potential of 0.5 V for 120 s every 5 min. The current in the bulk solution, 500 μm away from the cells, was also recorded by following the same procedures.

2.3 SIMULATION

The simulation was performed with Comsol Multiphysics 3.3 on a 2.8 GHz Intel Pentium IV processor and 2 GB RAM desktop PC.

We assumed that the redox mediator (ferrocyanide) present in the solution underwent a simple one electron transfer as shown below and the tip was held at diffusion controlled potential to avoid any kinetics complications.



where, R represents ferrocyanide species and O represents ferrocyanoide species.

Because the redox species O and R moved toward and away from the electrode surface only by concentration gradient Fick's second law of diffusion was used in the simulation. The concentration of species R is given as $C_R(r,z,t)$ and the diffusion equation in cylindrical coordinates is described as

$$\frac{\partial c_R}{\partial t} = D \left(\frac{\partial^2 c_R}{\partial r^2} + \frac{1}{r} \frac{\partial c_R}{\partial r} + \frac{\partial^2 c_R}{\partial z^2} \right)$$

where r and z are the coordinates as shown in Figure 2.3; t represents time; c and D represent the concentration and diffusion coefficient of species R

The boundary conditions at $t > 0$

At the tip: $0 < r < a, z = h1$

$$c_R(r,h1) = 0$$

$$c_O(r,h1) = 4$$

At the substrate: $0 < r < r_m, z = h2$

$$\frac{\partial c}{\partial z} = 0$$

At the cell membrane: $acr1, d < z < h2$

$$\text{Flux of R across the } acr1 = P*(R-R1)$$

where, P (m/s) is the permeability of species R across membrane or $acr1$ in the simulation. R and $R1$ represent the species outside and inside the cell respectively. Also, the glass sheath surrounding the electrode was considered as an insulator. Initially the concentration inside the cell was zero and the concentration in the bulk solution was 4 mM or 4 mol/m³. The species R was consumed by the cell depending on the permeability value of the membrane as well as by the tip located at 16 μm away from the substrate. The current at the electrode was determined by formula

$$I_{\text{tip}} = \int_{r=0}^{r=a} 2\pi n F D_R r \frac{\partial c_R(r, h^2)}{\partial z} dr$$

Where, $n = 1$; $F = 96485 \text{ C/mol}$; and $D_R = 1 \times 10^{-9} \text{ m}^2/\text{s}$;

The simulation model described above was solved by finite element method where the mesh was increased in exponential grid fashion to generate two-dimensional grid at the regions where sharp change in the concentration gradients were noticed.

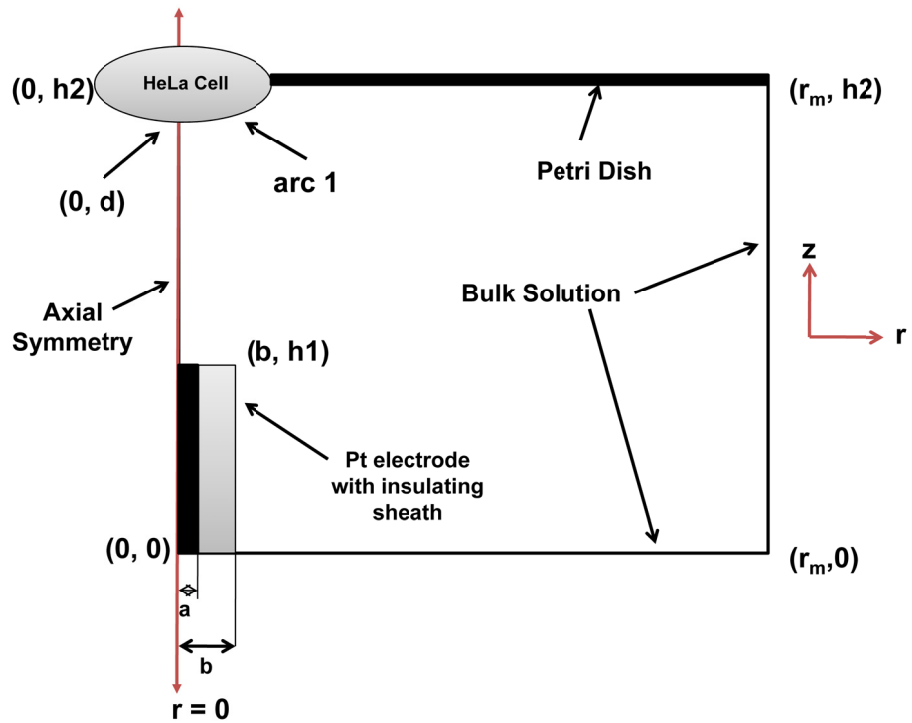


Figure 2.3: The schematics of simulation model in 2D axial symmetry.

X-Scan Simulation

HeLa cell was assumed to be semielliptical shape with symmetry along z -axis as showed in Figure 2.3. In this model, permeability was assumed to be zero along cell membrane or arc 1 since topography was the subject of interest here. The $10\ \mu\text{m}$ tip with $RG = 10$ was also considered symmetrical along z -axis (Figure 2.3). The tip was held at diffusion controlled potential at all times over the cell or arc 1 and the model was solved in steady state solver condition with the aid of Comsol Multiphysics software. The tip to dish distance was maintained at $16\ \mu\text{m}$ at all times. Each red dot in Figure 2.4B corresponds to simulated tip current calculated over a specified position on arc 1. For example, the lowest normalized peak current in Figure 2.4B was calculated over the highest point of arc 1 as showed in Figure 2.3. To measure the tip current at different position over the cell, the arc 1 was moved toward left by a distance of $1\ \mu\text{m}$ out of the active simulation sub domain instead of tip moving over the arc 1. This imitates the same condition such as a tip was moving over a cell in x -direction. Due to symmetry of cell along z -axis, scanning along arc 1 was adequate to obtain the full-simulated x -scan over the cell. Both height and radius of cell were considered as adjustable simulation parameters and were fitted with experimental data as showed in Figure 2.4B.

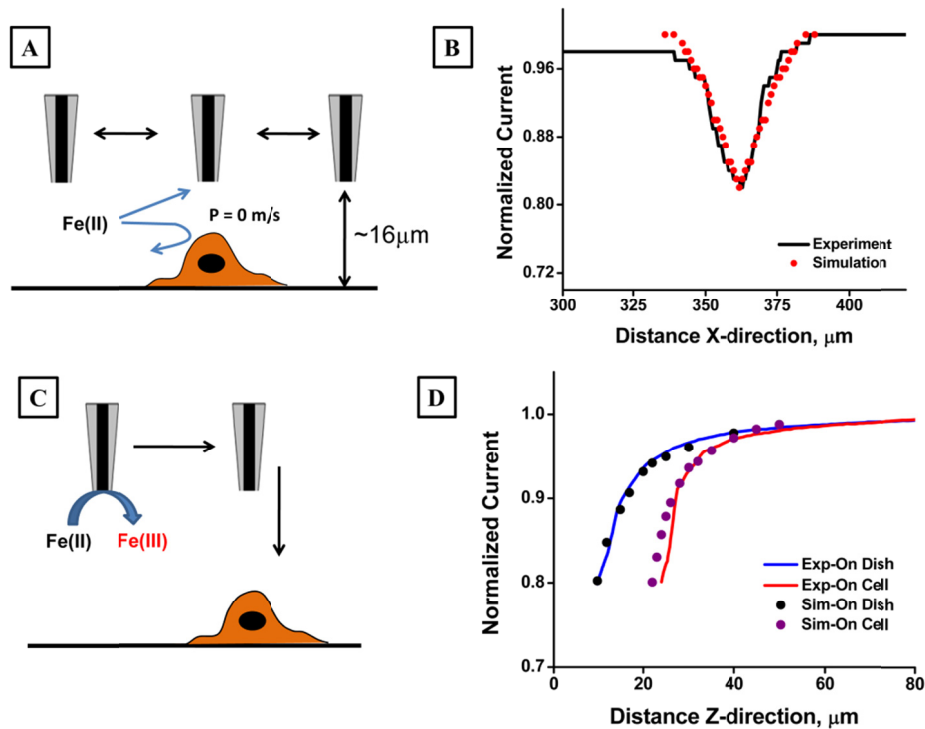


Figure 2.4: Determination of height of a single HeLa cell

(A) Tip-dish distance was adjusted to approximately 16 μm and then scanned over a single cell in x-direction at $E_T = 0.5\text{ V}$ with 4 mM of ferrocyanide in solution. (B) Cellular topography observed by x-scan experiment (solid line) on single cell at $E_T = 0.5\text{ V}$ with 4mM ferrocyanide in buffer. The x-axis distance was an arbitrary distance. Y-axis current was normalized against background current over dish. The simulated x-scan data fit with experiment data for the following simulation parameters: tip: 10 μm ($RG = 10$); bulk concentration: 4 mM; tip-dish distance: 16 μm ; cell diameter: 60 μm ; cell height: 9.8 μm . The simulation was performed in 2D-axial symmetry using Fick's second law of diffusion. The cell height was determined by simulated data fitting with experimental ones. (C) Approach curves over dish and over single cell at $E_T = 0.5\text{ V}$ with 4 mM ferrocyanide in buffer. (D) Experimental approach curves on dish and HeLa cell compared to simulated approach curves for total negative feedback.

Permeability Measurement

Simulations were done first with $P = 0$ at arc1 (i.e., without any added surfactant) to determine the current at the tip for the certain fixed height of the cell. Then after that different value of P in the range of zero to 8.7×10^{-6} m/s was used in the simulation to fit the experiment data. The tip current was always calculated with the tip located right above the highest point of the cell height. For example, when $P = 1.5 \times 10^{-6}$ m/s the concentration inside and outside the cell was calculated until $t = 1$ min and then the tip was brought close to the cell top i.e. $16 \mu\text{m}$ away from the dish and held there for 0.1 s (because the speed of tip x-scan was $1 \mu\text{m} / 0.1 \text{ s}$) to record the current at $t = 1.1$ min. The tip was then withdrawn from the top of the cell and the concentration gradient across the cell was again calculated with new value of parameter of P . The steps were repeated until $t = 60$ min.

2.4 RESULTS

Fluorescence-Based Cell Viability

The cytotoxicity of TX100 on HeLa cells were recorded at different concentrations for 5, 10 and 15 min (Figure 2.5A). The TX100 molecules were known to form micelles in the 0.22 to 0.24 mM range (26). In our cytotoxic test the cell viability dropped sharply when the TX100 concentration reached close to the CMC. Because the viability test was based on the integrity of the cell membrane, the micelle clearly showed a greater detergent action on the lipid bilayer than the individual surfactant molecule and hence was more toxic (27). Thus most of the studies by SECM were performed in the concentration range below the CMC to have enough time to observe the permeabilizing action on the cellular membrane by TX100 molecules.

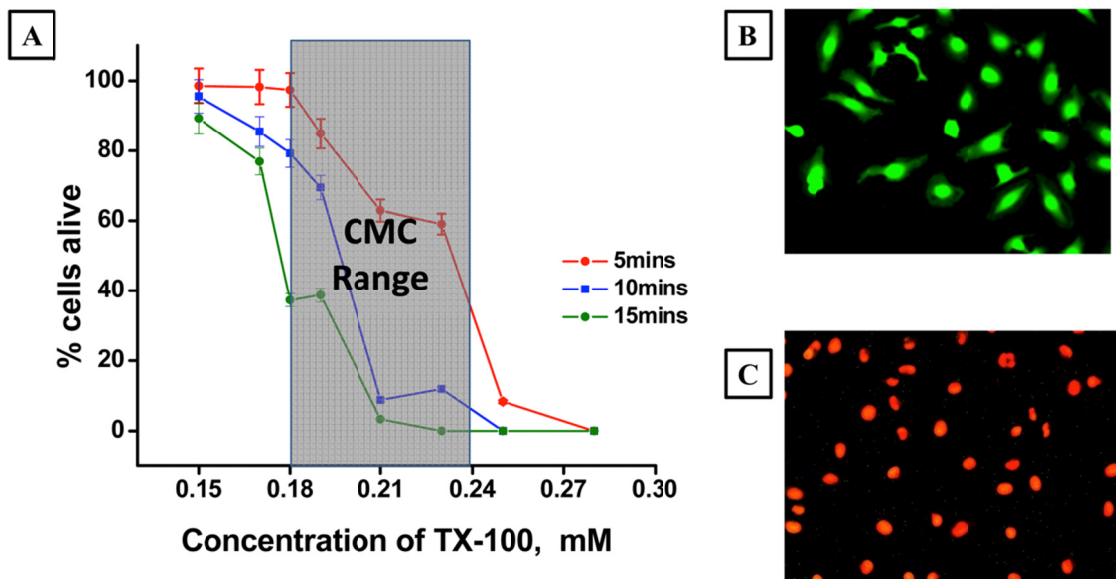


Figure 2.5: Viability test of HeLa cells in presence of varying concentration of TX-100

(A) Fluorescence based viability assay to HeLa cells exposed to different concentrations of TX100 for 5, 10, and 15 min. (B) Optical microscope image of green dyed cells representing the intact membranes of living cells and (C) of red dyed cells representing the collapsed membrane of dead cells.

Cellular Topography without Surfactant

HeLa cells, when alive, are anchored to the surface of the Petri dish and tend to be stretched out to maintain their normal cellular functions. Hence with the aid of SECM, the height and diameter of the cells on the dish surface could be measured. Figure 2.4 shows the cellular topography obtained from an x-scan SECM experiment. Here, a highly hydrophilic charged ion like ferrocyanide, and hence impermeable, was used as redox mediator. When the tip was scanned over the cell (Figure 2.4A), the diffusion of ferrocyanide molecules to the tip was blocked (so-called negative feedback) (15) depending on the topographical variation of the living cell, so the diameter, shape, and size of the cell could easily be determined. X-scan data, i.e., current vs. absolute distance in the x-direction scan (Figure 2.4B), can be converted to cellular height vs. absolute x-direction distance with the aid of a simulated negative feedback approach curve on the dish. By using experimental data, cell height was determined to be 9 to 12 μm and the diameter was in the range of 50 to 60 μm . Simulated x-scan data was fitted with the experimental data with a precision range of $\pm 1 \mu\text{m}$ (Figure 2.4B). Because SECM gives z-direction topographic feature information very accurately, approach curves on a single cell were carried out to obtain additional cell heights. Figure 2.4D shows the comparative approach curve on the dish and single cells. To confirm the cell height the simulated approach curve had been fitted with both experimental approach curves. From the fitting in Figure 2.4D the cell height was $14 \pm 1 \mu\text{m}$.

Cell Membrane Permeability

SECM scans as above were carried out in the presence of TX100. Here, the 10 μm Pt tip was scanned in the x-direction over a single cell at a fixed height of approximately 16 μm and at a potential of 0.35 V. The current-distance profile with respect to time in the presence of 0.17 mM and 0.19 mM TX100 and 4 mM ferrocyanide was obtained as

shown in Figure 2.6 A and B. The normalized minimum current or the peak current against the background current from the x-scan was plotted against time, including results with 1.9 mM TX100, is shown in Figure 2.6C. In the presence of 0.19 mM of TX100 (Figure 2.6C) the normalized peak current went to the background current ($i_{T,\infty}$) within 2 min. This result clearly indicates that TX100 at these concentrations was lethal to cells causing the cell membrane to break apart and detach completely from the surface of the Petri dish. When 0.17 mM TX100 was added, however, the normalized minimum current decreased about 20% from the pre-TX100 treatment before essentially recovering after about 20 min in some cases. The recovery period and state of recovery varied from cell to cell as shown in Figure 2.6C. The observed current decrease could be attributed to either an increase in permeability of the cell membrane or to an increase in topographical height. If the permeability increase model was correct, then the decrease was due to competitive consumption of ferrocyanide molecules both by SECM tip and by the cell. The rise of minimum current or the peak current to the pre-TX100 current level after 20–30 min may signal the cessation of competitive consumption of ferrocyanide molecules. This would indicate recovery of the cell membrane from the permeabilization action of 0.17 mM TX100 without the cell dying.

The cell height and topographic features from the x-scan in the absence of surfactant yielded a cell diameter and height of 50 μm and 10 μm , respectively. Permeability parameters for the cell membranes or boundaries were then introduced into the simulation model. The simulated x-scan data was then fitted with the experimental data at the same fixed height. Because the permeability changed with the exposure time of cells to 0.17 mM TX100, simulations were done to fit each curve to determine the permeability of the membrane at that particular time. This gave a range of permeability values from 4.0 to 8.7×10^{-6} m/s for the ferrocyanide molecules permeating through a live cell membrane. Hence, with the average permeability value of $6.5 \pm 2.0 \times 10^{-6}$ m²/s, number of ferrocyanide molecules inside a single cell after 32 min was determined to be

$1.06 \pm 0.54 \times 10^6$ in presence of 0.17mM TX100. This model assumed that the cells maintained their integrity, i.e., the cell height and diameter were constant throughout the experiment. The permeability, P, is defined here as the velocity of a molecule of interest through a membrane; where $P = KD/L$, K is the partition constant between the molecule and the membrane, D is the diffusion coefficient of the molecule, and L is the length through which the molecule travels, i.e., the thickness of the membrane. Because the SECM tip was always held at the potential for ferrocyanide oxidation, the tip was not sensitive to ferricyanide, so only the ferrocyanide molecules permeating through the cell membrane effect the SECM tip current.

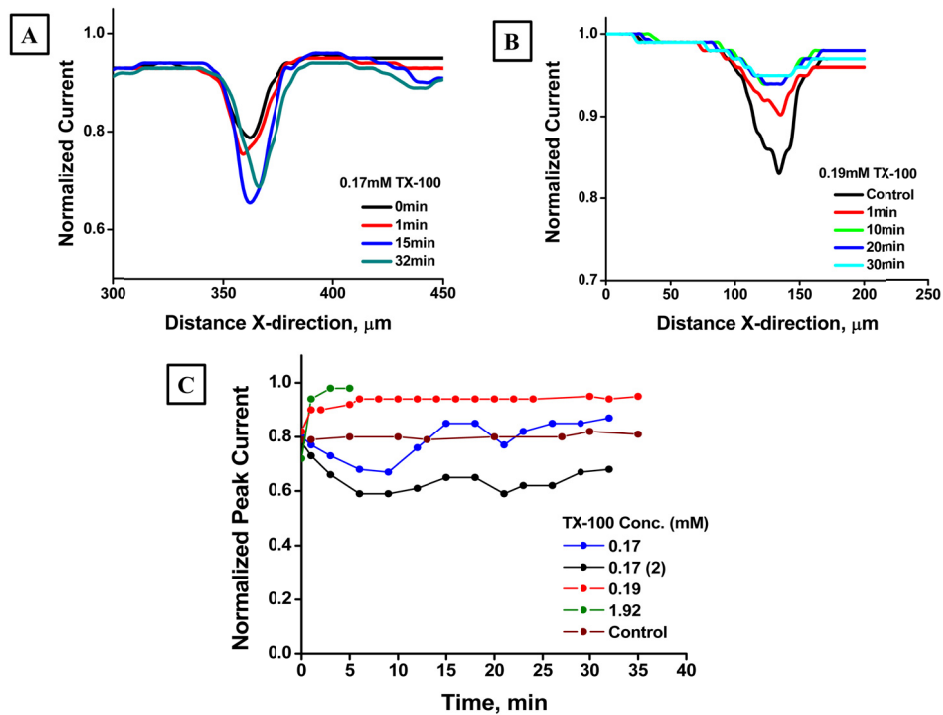


Figure 2.6: Permeability measurement of a single HeLa cell in presence of varying concentrations of TX-100

X-scan experiments with (A) 0.17 mM or (B) 0.19 mM TX100 and 4 mM ferrocyanide in solution. (C) Normalized peak current was plotted against time for different concentrations of TX100 exposed to HeLa cell. Permeability of a single cell in presence of 0.17 mM TX100 was fitted to be $6.5 \pm 2.0 \times 10^{-6}$ m/s.

Cellular Topography in Presence of TX100

SECM approach curves have been used in many previous studies to estimate surface topography. During the probe scan experiment the tip was moved over the cell at a very slow scan rate ($\sim 5 \mu\text{m/s}$). The decrease of current that was observed might have occurred due to an increase in cell height, e.g., by swelling of the cell volume, but may also have been caused by changes in permeability of the membrane. To distinguish between these effects, time dependent approach curves on a single cell were performed in the presence of different concentrations of TX100 as shown in Figure 2.7A. For a z-scan rate of approximately $5 \mu\text{m/s}$, the time to record a single approach curve takes about 20 sec. Figure 2.7B represents the actual cell height variation with time. The cell height was taken as the difference between the approach curve to the Petri dish and to single cell. The average cell height was $10 \pm 2 \mu\text{m}$. Cells exposed to 0.17mM or less of TX100 solution, the z-direction topography, and the cellular height did not change significantly from that in its absence. When 0.19 mM of TX100 was added, the cells started losing their topographical features as seen in Figure 2.7B, where the cell height approached zero after 30 min of exposure to 0.19 mM of TX100. This shows a loss of viability at this concentration, as also observed in the fluorescence-based viability tests (Figure 2.5). This demonstrates that obtaining SECM approach curves on a single cell is a good technique to monitor the cell height.

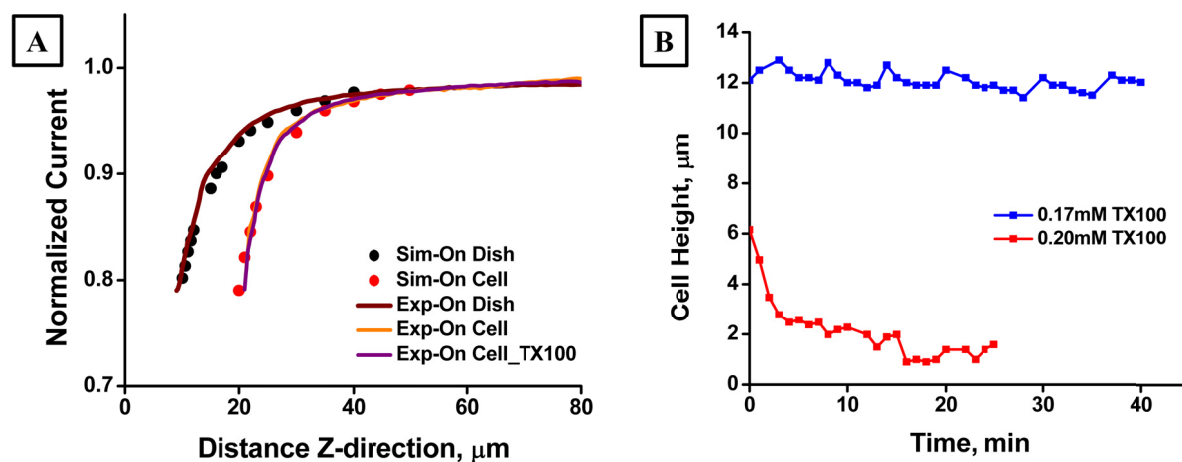


Figure 2.7: Topographical variation of a single HeLa cell in presence of TX-100

(A) Approach curves over dish and on single cell in absence and presence of 0.17mM of TX100 and 4mM redox mediator in solution. The experimental approach curve fitted to theoretical negative feedback approach curve over dish and over cell to determine the pre-TX100 treated cell height. (B) The apparent cell height vs. time in presence of 0.17 mM and 0.20 mM of TX100 respectively.

Current-time (i_T vs. t) Response over a Single Cell

These curves were taken to study effects at longer times. Figure 2.8B shows a i_T vs. t response curve when the 10 μm tip was held approximately 5 μm away from the surface of the cell in presence of 4 mM ferrocyanide and 0.17 mM TX100. The current recorded was plotted against time with the tip both above the cell and at approximately 500 μm away from the dish (Figure 2.8C). The current above the cell decreases with time while the bulk current remains constant throughout the experimental time period. This indicates that the cells consume ferrocyanide molecules competitively with the tip held at the diffusion-controlled potential. No change in the cell height was also confirmed from the approach curve before and after 40 min of exposure of 0.17 mM TX100 (Figure 2.8D).

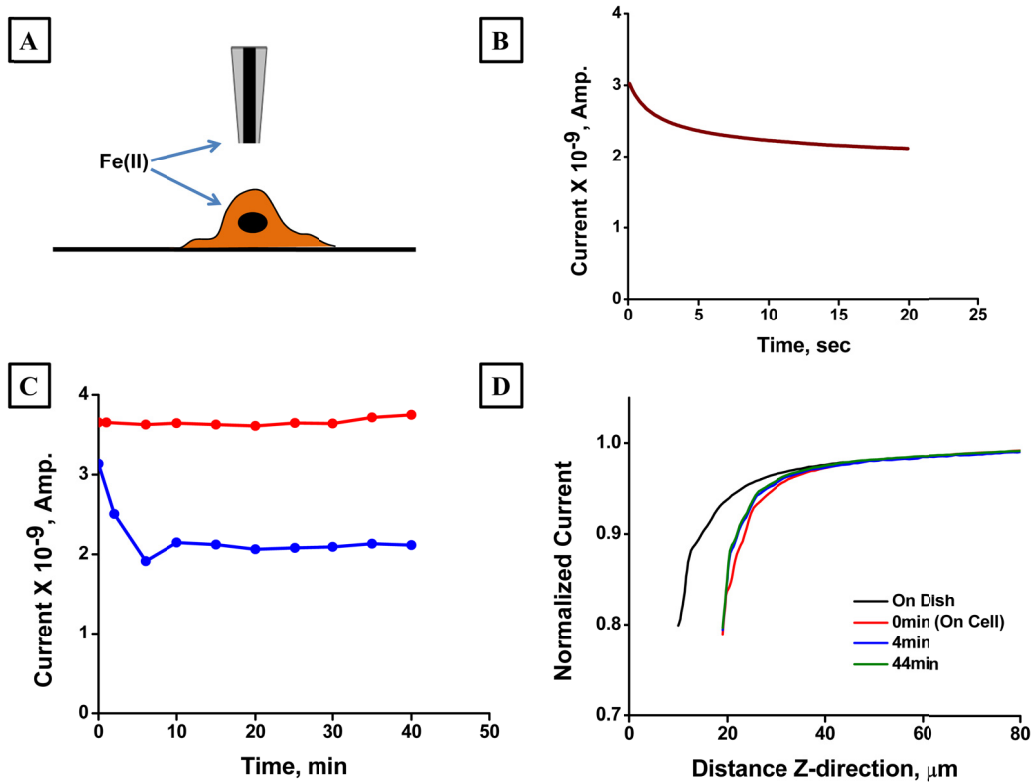


Figure 2.8: I-t experiment over a single HeLa cell in presence of TX-100

Tip currents and approach curves after different exposure times. (A) Schematic representation of the 10 μm Pt tip held 5 μm above a single cell at a constant potential of 0.5 V in buffer containing 4 mM ferrocyanide and 0.17 mM of TX100. (B) Current-time response over the cell. (C) Sampled current at $t = 20$ s was plotted against time of exposure of cell to TX100. Red and blue lines represent the sampled current response in the bulk solution ($i_{T,\infty}$) and over the cell, respectively. (D) Approach curves over dish and over single cell in the absence and presence of 0.17 mM of TX100.

2.5 DISCUSSION

When the concentration of TX100 is below the CMC range (i.e. 0.17 mM and less) the surfactant may act as a permeabilizing agent depending on the dose and duration of exposure to cells. This is a good range for transfection of the cell with an added agent, but prolonged exposure to cells even at these low concentrations can lead to some cell death. When concentrations of TX100 in the CMC range, >0.18 mM, are used, the cell membrane disintegrated causing a collapse of the entire cell structure and cell death within a few minutes.

SECM allows one to follow a series of changes a cell undergoes in terms of its size, shape, and membrane permeability. At 0.17 mM or lower TX100 concentration provides enough time to study the cell behavior and allows interpretation of the data. When 0.17 mM TX100 solution is added to the cell, the membrane first becomes permeabilized sufficiently to allow hydrophilic molecules, like ferrocyanide, to permeate the cell membrane, while the cell height remains unaffected. Even when exposed for a long time (≥ 20 min) cells recover from membrane damage after the surfactant is removed. Occasionally the cell undergoes a reduction in height during its recovery from periods of increased permeability. When 0.20 mM TX100 is added, the cell membrane becomes “overpermeabilized” within 1 min, when irreversible damage from the surfactant occurs. Eventually the cell loses its integrity and collapses, which can be observed by SECM as a higher current in an x-scan or an approach curve very much the same as the approach taken over the dish. Solubilization of the lipid bilayer may be caused by disruption of the lipid–lipid interaction due to enhanced lipid-detergent micelle interactions. The insertion of individual detergent molecules or small aggregates at concentrations just below the CMC causes the membrane to become more permeable to a wide variety of molecules which otherwise cannot enter inside the cell allowing transfection. However at detergent concentrations where micelles form (at or above the CMC range), rapid breakdown of the membrane occur (11, 28–31).

2.6 CONCLUSION

Any concentration of TX100 at or above its CMC concentration (0.18 to 0.24 mM) in the solution is fatal to HeLa cells. This can be observed by SECM and confirmed by fluorescent tests. Damage to the cell membrane was irreversible when the cells were exposed to TX100 concentrations above CMC concentration for 10 to 30 s. However, no such effect on cell membrane permeability was observed at a concentration significantly lower (<0.15 mM) than the CMC.

When the concentration of TX100 was at or near 0.17 mM, the HeLa cell membranes became permeable after an exposure of less than 20 min. After this exposure, the cells were able to recover upon removal of surfactant solution. The permeability was estimated to be $6.5 \pm 2.0 \times 10^{-6} \text{ m}^2/\text{s}$ when exposed to 0.17 mM TX100 for 32 min. Within this permeability range highly charged hydrophilic redox molecules, such as ferrocyanide, were able to pass through a live cell membrane, which would otherwise be an impermeable barrier to these redox mediators. The number of ferrocyanide molecules passed through single cell membrane after 32 min was calculated to be $1.06 \pm 0.54 \times 10^6$ in presence of 0.17 mM TX100. Thus SECM can provide not only cell viability information at the single cell level but can also give quantitative information about the cell membrane permeability. The generality of these guidelines for transfection of other cells is under investigation.

2.7 ACKNOWLEDGEMENT

We thank the National Science Foundation (CHE 0808927) and the Robert A. Welch Foundation (F-0021) for support of this work.

2.8 REFERENCE

- ¹ Gennuso F, et al. (2004) Bilirubin protects astrocytes from its own toxicity by inducing up-regulation and translocation of multidrug resistance-associated protein 1 (mrp1). *Proc Natl Acad Sci USA* 101:2470–2475.
- ² Rajagopal A, Pant AC, Simon SM, Chen Y (2002) In Vivo analysis of human multidrug resistance protein (MRP1) activity using transient expression of fluorescently Tagged MRP1. *Cancer Res* 62:391–396.
- ³ Hipfner DR, Gauldie SD, Deeley RG, Cole SPC (1994) Detection of theMr 190,000 multidrug resistance protein, MRP, with monoclonal antibodies. *Cancer Res* 54:5788–5792.
- ⁴ Borner MM, et al. (1994) The detergent TX100 induces a death pattern in human carcinoma cell lines that resembles cytotoxic lymphocyte-induced apoptosis. *FEBS Lett* 353:129–132.
- ⁵ Benoit J, Cormier M, Wepierre J (1988) Comparative effects of four surfactants on growth, contraction and adhesion of cultured human fibroblasts. *Cell Biol Toxicol* 4(1):111–122.
- ⁶ Dayeh VR, Chow SL, Schirmer K, Lynn DH, Bols NC (2004) Evaluating the toxicity of TX100 to protozoan, fish, and mammalian cells using fluorescent dyes as indicators of cell viability. *Ecotox Environ Safe* 57:375–382.
- ⁷ Laouar L, Lowe KC, Mulligan BJ (1996) Yeast response to nonionic surfactants. *Enzyme Microb Tech* 18:433–438.
- ⁸ Barnett SM, Dracheva S, Hendler RW, Levin IW (1996) Lipid-induced conformational change of an integral membrane protein: An infrared spectroscopic study of the effects of TX100 treatment on the purple membrane of *Halobacterium halobium* ET1001. *Biochemistry* 35:4558–4567.
- ⁹ Aránzazu MP, Ostolaza H, Goñi FM, Barberá-Guillem E (1990) Surfactant-induced cell toxicity and cell lysis a study using B16 melanoma cells. *Biochem Pharmacol* 40(6):1323–1328.

- ¹⁰ Benoit J, Cormier M, Wepierre J (1988) Comparative effects of four surfactants on growth, contraction and adhesion of cultured human fibroblasts. *Cell Biol Toxicol* 4(1):111–122.
- ¹¹ Maire ML, Champeil P, Moller JV (2000) Interaction of membrane proteins and lipids with solubilizing detergents. *Biochim Biophys Acta* 1508:86–111.
- ¹² Fontaine P, et al. (2007) Unexpected stability of phospholipid langmuir monolayers deposited on TX100 aqueous solutions. *Langmuir* 23:12959–12965.
- ¹³ Nyholm T, Slotte JP (2001) Comparison of TX100 penetration into phosphatidylcholine and sphingomyelin mono- and bilayers. *Langmuir* 17:4724–4730.
- ¹⁴ London E, Brown DA (2000) Insolubility of lipids in TX100: Physical origin and relationship to sphingolipid/cholesterol membrane domains (rafts). *Biochim Biophys Acta* 1508:182–195.
- ¹⁵ Bard AJ, Mirkin MV, eds. (2001) Scanning Electrochemical Microscopy (Mercel Dekker, New York).
- ¹⁶ Li X, Bard AJ (2009) Scanning electrochemical microscopy of HeLa cells—Effects of ferrocene methanol and silver ion. *J Electroanal Chem* 628:35–42.
- ¹⁷ Guo J, Amemiya S (2005) Permeability of the nuclear envelope at isolated *Xenopus* Oocyte nuclei studied by scanning electrochemical microscopy. *Anal Chem* 77(7):2147–2156.
- ¹⁸ Hirano Y, et al. (2008) Construction of time-lapse scanning electrochemical microscopy with temperature control and its applications to evaluate the preservation effects of antifreeze proteins on living cells. *Anal Chem* 80:9349–9354.
- ¹⁹ Gonsalves M, Macpherson JV, O’Hare D, Winlove CP, Unwin PR (2000) High resolution imaging of the distribution and permeability of methyl viologen dication in bovine articular cartilage using scanning electrochemical microscopy. *BBA-Gen Subjects* 1524(1):66–74.

- ²⁰ Gonsalves M, et al. (2000) Scanning electrochemical microscopy as a local probe of oxygen permeability in cartilage. *Biophys J* 78:1578–1588.
- ²¹ London E, Brown DA (2000) Insolubility of lipids in TX100: Physical origin and relationship to sphingolipid/cholesterol membrane domains (rafts). *Biochim Biophys Acta* 1508:182–195.
- ²² Lanyi JK (1973) Influence of electron transport on the interaction between membrane lipids and TX100 in halobacterium cutirubrum. *Biochemistry* 12(7):1433–1438.
- ²³ Maire ML, Champeil P, Moller JV (2000) Interaction of membrane proteins and lipids with solubilizing detergents. *Biochim Biophys Acta* 1508:86–111.
- ²⁴ Fontaine P, et al. (2007) Unexpected stability of phospholipid langmuir monolayers deposited on TX100 aqueous solutions. *Langmuir* 23:12959–12965.
- ²⁵ Troiano GC, Tung L, Sharma V, Stebe JK (1998) The reduction in electroporation voltages by the addition of a surfactant to planar lipid bilayers. *Biophys J* 75:880–888.
- ²⁶ Sigma-Aldrich Co (1999) TX100, T9284 product information sheet (Sigma-Aldrich, St. Louis).
- ²⁷ Rafat M, et al. (2008) Association (micellization) and partitioning of aglycon triterpenoids. *J Colloid Interface Sci* 325(2):324–330.
- ²⁸ Morandat S, Kirat EK (2006) Membrane resistance to TX100 explored by real time atomic force microscopy. *Langmuir* 22:5786–5791.
- ²⁹ Paternostre MT, Roux M, Rigaud JL (1988) Mechanisms of membrane protein insertion into liposomes during reconstitution procedures involving the use of detergents. 1.Solubilization of large unilamellar liposomes (prepared by reverse-phase evaporation) by TX100, Octyl Glucoside, and Sodium Cholate. *Biochemistry* 27:2668–2677.
- ³⁰ Rigaud JL, Paternostre MT, Bluzat A (1988) Mechanisms of membrane protein insertion into liposomes during reconstitution procedures involving the use of

detergents. 2. Incorporation of the light-driven proton pump bacteriorhodopsin. *Biochemistry* 27:2677–2688.

- ³¹ Nyholm T, Slotte JP (2001) Comparison of TX100 penetration into phosphatidylcholine and sphingomyelin mono- and bilayers. *Langmuir* 17:4724–4730.

Chapter-3: Inhibition of the MRP1-Mediated Transport of the Menadione-Glutathione Conjugate (Thiodione) in HeLa Cells as Studied by Scanning Electrochemical Microscopy

ABSTRACT

Oxidative stress induced in live HeLa cells by menadione (2-methyl-1,4-naphthaquinone) was studied in real time by scanning electrochemical microscopy (SECM). The hydrophobic molecule menadione diffuses through a living cell membrane where it is toxic to the cell. However, in the cell it is conjugated with glutathione to form thiodione. Thiodione is then recognized and transported across the cell membrane via the ATP-driven MRP1 pump. In the extracellular environment, thiodione was detected by the SECM tip and was 140, 70 and 35 μM upon exposure of the cells to menadione concentrations of 500, 250 and 125 μM , respectively. With the aid of finite element modeling, the kinetics of thiodione transport was determined to be 1.6×10^{-7} m/s and was 10 times faster than menadione uptake. Selective inhibition of these MRP1 pumps inside live HeLa cells by 5-(3-(2-(7-chloroquinolin-2-yl) ethenyl) phenyl)-8-dimethylcarbonyl-4,6-dithiaoctanoic acid (MK571) was also studied in real time by SECM. The thiodione efflux was reduced to 50 μM in the presence of 500 μM menadione and 50 μM MK571. A similar observation was made with monoclonal antibody QCRL-4 as a selective blocking agent to the MRP1 pumps in live cells. The thiodione flux from a monolayer of transfected HeLa cells in the presence of 500 μM menadione dropped by about 50%. The reduced thiodione flux confirmed that thiodione was transported by MRP1, and that glutathione is an essential substrate for MRP1 mediated transport. This finding suggests that monoclonal antibodies can be a useful tool in inhibiting the transport of these MDR pumps and thereby aiding in overcoming multidrug resistance.

3.1 INTRODUCTION

Multidrug resistance (MDR) pumps play a critical role in the detoxification pathway and cell survival under the oxidative stress caused by quinone or quinone-based chemotherapeutic drugs. Among the MDR pumps, the multidrug resistance protein (MRP1) pump is known to pump a broad variety of organic anions out of cells (1). According to the accepted model, MRP1 pumps out glutathione-S-conjugates (GS-conjugates), oxidized glutathione (GSSH), and reduced glutathione (GSH) as well as the unmodified drugs in the presence of physiological concentration of GSH; for example vincristine or daunorubicin are transported out of the cells by MRP1 in unmodified form in the presence of GSH (2). The cytotoxicity of a particular drug also depends on the types of MDR pumps and whether they are over-expressed in a cell under oxidative stress. For example, MRP pumps are known to be highly expressed in colon, breast and ovarian cancer cells whereas P-glycoprotein (Pgp) pumps are widely expressed in colon, renal and liver cancer cells but poorly expressed in breast, lung, and ovarian tumors (3). Hence, there are differences between the oxidative stress response of one type of cell to another and this is significant when comparing the effects of xenobiotics being added to different cells. In rat platelets, 85% intracellular GSH was reported to deplete as menadione-GSH conjugate, whereas in hepatocytes, 75% of intracellular GSH was depleted by menadione due to formation of GSSG (4).

Depending on their modifications, quinones induce cytotoxicity on living cells by different pathways (4). A recycler such as 2,3-dimethoxy-1,4-naphthaquinone exhibits oxidative stress purely by redox cycling, forming semiquinones, superoxide and hydroxyl radicals; thus depleting the reduced glutathione or GSH pool present inside the cell by forming oxidized glutathione or GSSH. A second type of quinone, an arylator such as 1,4-benzoquinone, exhibits cytotoxicity through arylation, forming GS-conjugates and thus depleting the intracellular GSH. Quinone-based oxidative stress in living cells differs from oxidative stress based on extracellularly administered hydrogen peroxide. The later

agent is capable of inducing lipid peroxidation and subsequently rupturing the cell membrane before even entering the cell. Other types of quinone such as menadione (2-methoxy-1,4-naphthaquinone) can act as both a redox cycler and arlyator. Because of its hydrophobicity, menadione can pass through an intact cell membrane and induce oxidative stress by producing superoxide and hydroxyl radical. As part of the cells defense against such oxidative stress, GSH present inside the cell subsequently undergoes sacrificial nucleophilic addition or arylation with menadione in presence of the GS-transferase enzyme, forming menadione-S-glutathione (thiodione). However, the conjugate retains the ability to carry out redox recycling to form superoxide and hydroxyl radical, and this is not, by itself, an effective detoxification pathway unless the thiodione has been recognized by GS-X or MDR pumps as a substrate and pumped out of the cell by an ATP-driven process (Figure 3.1) (5-10).

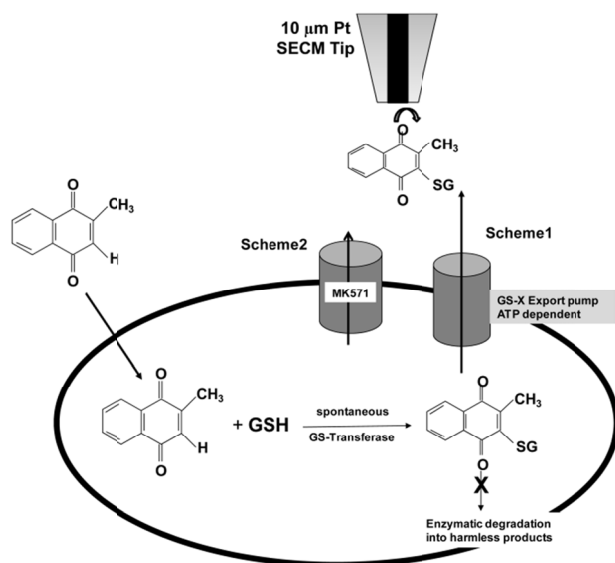


Figure 3.1: Schematic diagram of cellular response to menadione in the presence or absence of MRP1 blocker MK571.

MRP1 transports both endogenous substrates such as glutathione, steroids, LTC₄, LTD₄, LTE₄ as well as substrates like doxorubicin, daunorubicin, GS-conjugates, vinblastine. However, LTC₄ has the highest affinity for MRP1 (2, 6, 9, 11-15). The inhibition of these MRP1 pumps increases the accumulation of intracellular xenobiotics or their conjugates; which therefore increases the cytotoxicity of the drugs towards the cell. MK571 (5-(3-(2-(7-chloroquinolin-2-yl) ethenyl) phenyl)-8-dimethylcarbamyl-4,6-dithiaoctanoic acid), a LTD₄ receptor antagonist, has been reported to act as competitive inhibitor for MRP1 mediated transport, both for GS-conjugate transport (such as thiodione) as well as for the transport of unconjugated GSH mediated xenobiotics transport such as daunorubicin (15-26).

To understand mechanistically the function of this MRP1 pump in physiological condition, several immunoblot, immunoprecipitate and immunofluorescence based studies (27-35) have been made with MRP1 specific antibodies such as QCRL-1, QCRL-2, QCRL-3, QCRL-4 and QCRL-6. These IgG class antibodies have been developed to recognize a specific sequence of amino acids in the MRP proteins. For example, QCRL-1, -2, -3 recognize 918-924, 617-858, 617-932 amino acid sequences respectively; whereas QCRL-4 and QCRL-6 bind overlapping sequences of 1294-1531 amino acids, –COOH proximal nucleotide binding site (NBD2). Hipfner and Cole (27-30) have used these antibodies to map the topology of this entire transmembrane protein. An inhibitory effect of this antibody has also been reported with the endogenous substrate, LTC₄, whereas QCRL-3 has been reported (30, 35) to inhibit the photolabeling of MRP1 by LTC₄, proving that the 617-932 sequence is the major substrate binding site. Thus different kinds of antibodies can be used to understand the functionally important domain of the MRP1 pump, especially in terms of binding sites of different xenobiotic substrates and pumping out by an ATP-driven process.

Although there have been numerous studies on oxidative stress with different arrays of drugs and xenobiotics on diverse mammalian cell lines, most of them have been

done with assays developed on lysed cells after they were exposed to xenobiotics. Very few quantitative studies have been performed using live intact cells and their response in presence of xenobiotics, and fewer, particularly in terms of transmembrane flux affected by various antibodies recognizing different epitopes. Most of the immunoblot-based studies with antibodies and MDR pumps used antibodies to detect the pumps qualitatively, but very few studies have been done to demonstrate the blocking of a MRP1 pump efflux with an antibody in the dynamic environment of a live intact cell.

In previous studies, (36,37) we studied this process in yeast and heptablastoma cells with the SECM. In this paper we show that HeLa cells exposed to menadione form the GS-conjugate, which is then pumped into the extracellular environment by ATP-driven MDR pumps. The quantitative estimation of thiodione flux out of the living cells was measured by SECM on a real time basis. The selective blocking by MK571 of these MRP1 pumps present in a live HeLa cell was also demonstrated; thus confirming that thiodione is indeed a substrate for MRP1 pumps and plays an important role in the cellular defense mechanism against quinone-based oxidative stress. In addition, a monoclonal antibody such as QCRL-4 was able to inhibit the thiodione flux under oxidative stress, again demonstrating the relevant function of MRP1.

3.2 MATERIALS & METHODS

Chemicals

Menadione was purchased from Sigma Aldrich (M57405) and recrystallized from ethanol before use. All other chemicals were used as received. MgSO₄, CaSO₄ and K₂SO₄ were obtained from Fischer Scientific. D-glucose and HEPES were from Sigma-Aldrich. MK571 was obtained from Axxora (catalog number ALX-340-021) and QCRL-4 antibody (catalog number sc-18874) and Lipodin-Ab (catalog number 500115) from

Santa Cruz Biotechnology and Abbiotec respectively. All solutions were made with 18 MΩ Milli-Q (Millipore) reagent water treated with UV irradiation for 1 h.

Cell Culture

HeLa cells were purchased from ATCC (catalog number CCL-2) and cultured as per instructions provided by ATCC. Briefly, cells were grown and maintained in “ATCC-formulated Eagle’s Minimum Essential Medium” (ATCC 30-2003) culture medium supplemented with 10% fetal bovine serum (ATCC 30-2020) on a tissue culture Petri dish (Falcon 353801). The temperature was maintained at 37 °C in a water-jacketed incubator (model 2310, VWR Scientific) with 95% air and 5% CO₂. The cells were serum starved with 0.1% serum for 18-20 h inside the incubator before any SECM or cytotoxicity experiment.

When an appropriate cell coverage on the petri dish was obtained, the dish was taken out of the incubator, and the cells were washed with buffer solution (10 mM HEPES, 5.55 mM glucose, 75 mM Na₂SO₄, 1 mM MgSO₄ and 3 mM K₂SO₄) twice. The cells were then incubated with 1 mL of buffer solution at room temperature for 1 h. The buffer solution was later replaced by the appropriate experimental solution prepared with buffer.

Cytotoxicity Assay

We performed two types of cytotoxicity assays to determine the cell viability: trypan blue, and fluorescent-based cytotoxicity assay.

Trypan Blue Based Viability Test: When an appropriate coverage of cells was achieved, the Petri dish was taken out of the incubator and HEPES buffer was added for one hour at room temperature. The buffer was then replaced by an appropriate concentration of menadione solution in buffer for varying periods of time. The

menadione solution was then replaced, the cells were washed with only buffer twice, and then trypsin was added to dish for five minutes. The cell suspension was then centrifuged and washed with buffer before dispensing the cell suspension on the Coulter counter. If the cell membrane collapses, the blue dye (trypan blue) can pass through the membrane, and the cell will be stained with blue color. The blue dye cannot pass through the intact membrane of a living cell, and so the living cells will look transparent under microscope. The blue-color-stained and non-stained cells were then counted under optical microscope.

Fluorescent Based Viability Test: The fluorescent-based viability assay kit (Biotium Inc., USA) was used to detect living and dead cells simultaneously in the sample. This assay employs two dyes, calcein AM (green dye) and EthD-III (red dye). In this work, 1 mL of 2 μ M calcein AM and 4 μ M EthD-III was used to detect the viability of the cells. Calcein AM has the ability to pass through an intact cell membrane and react with the intracellular enzyme esterase, which converts it into an intensely green fluorescent calcein dye (excitation/emission 495nm/515nm). The polyanionic calcein dye remains confined inside intact cell membranes so the living cells are easily visible through a microscope. EthD-III can permeate only through damaged membranes and reacts with intracellular nucleic acid to emit intense red fluorescence inside dead cells (excitation/emission 530nm/635nm). So, a green color represents live intact cell membranes whereas the red color represents ruptured cell membranes or dead cells. This assay is very useful for detecting both live and dead cells at the same time without any pre-treatment of the samples. The green and red stained cell photos were then processed by Image J software (available from the NIH website) to count the number of live and dead cells.

SECM Experiment

A 10 μm diameter Pt ultramicroelectrode (UME) was used in SECM experiments. A detailed description of UME fabrication can be found elsewhere (38). Pt wire (0.5 mm) and Hg/Hg₂SO₄ were used as counter and reference electrodes, respectively. All the potentials given in this paper are *vs.* Hg/Hg₂SO₄.

A Petri dish containing 80% coverage of HeLa cells was taken out of the incubator and placed on an SECM (Model 900B, CH Instruments, Austin, TX) stage as shown in Figure 3.2A. The cells were then washed twice with 1 mL of buffer solution and were subsequently incubated for 1 h in buffer-only solution. During the 1 h incubation period, an approach curve with oxygen as a mediator was performed to fix the tip-substrate (Petri dish) distance at 100 μm . Buffer was then replaced by an appropriate concentration of menadione solution. Cyclic voltammograms (CV) were taken between -0.8 to +0.65 V at approximately every 1 min to measure the concentration of thiodione being pumped out of the cellular monolayer attached to the dish. The basic electrochemistry of menadione, thiodione and glutathione has been described in an earlier publication (36). Briefly, both menadione and thiodione reduce at -0.7 V, whereas thiodione shows a unique oxidation peak at 0.1 V. Glutathione is not electroactive in this potential range.

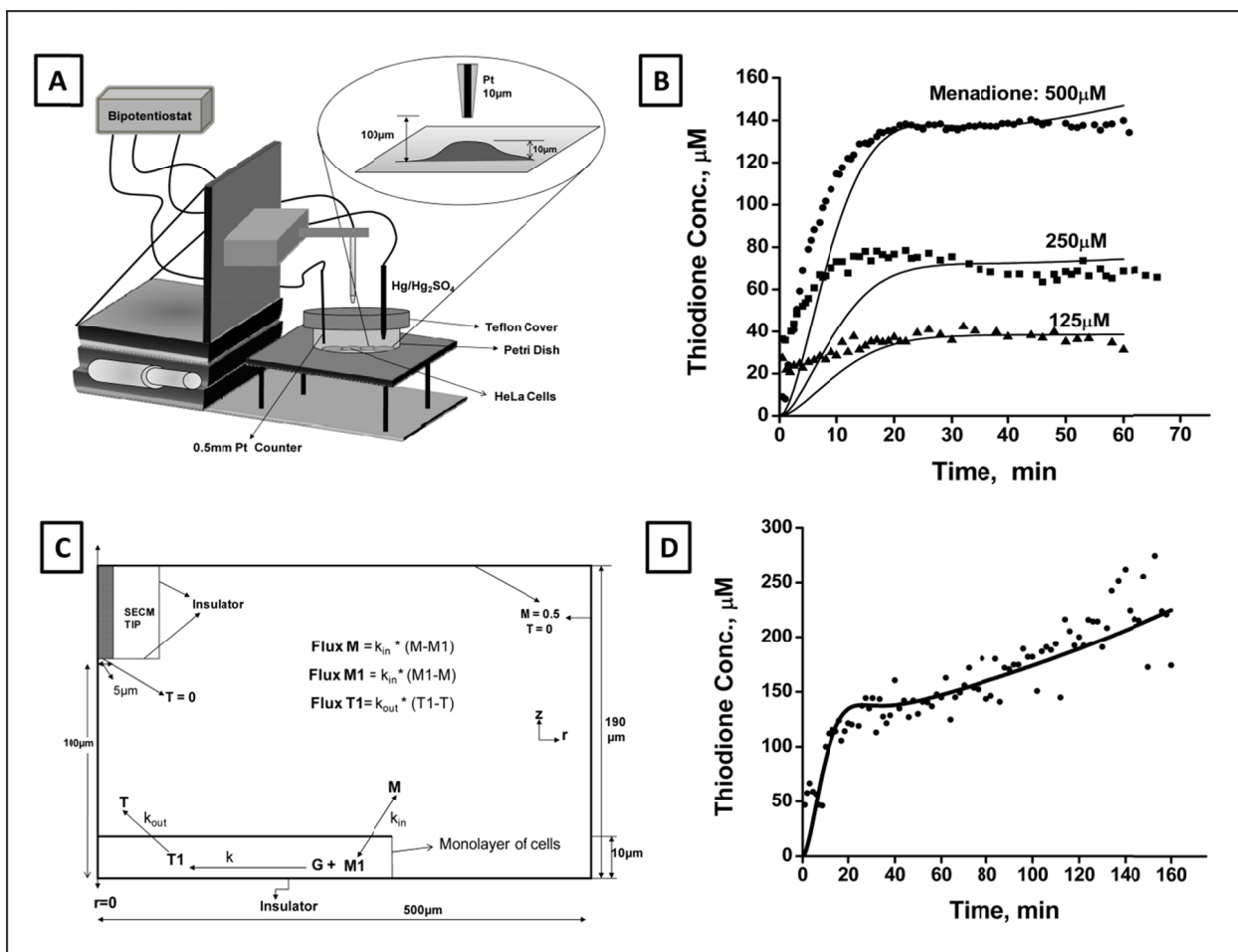


Figure 3.2: Cellular response to varying concentration of menadione

(A) Schematic diagram of SECM set-up for direct electrochemical detection of thiodione efflux from a monolayer of living HeLa cells. (B) : The thiodione concentration with time (min) when cells were exposed to 500 μM (solid circle), 250 μM (solid square) and 125 μM (solid triangle) concentrations of menadione. The solid line represents the fitting of simulated curve with experimental data (dotted points). Simulation parameters: k_{in} : 1.6×10^{-8} m/s; k_{out} : 1.6×10^{-7} m/s; (C): Schematic diagram of the simulation model to determine the kinetics of menadione (M) permeating through the cell membrane and thiodione (T) efflux by MDR pumps. M1: menadione inside cell; G: Glutathione; T1: Thiodione inside cell. The concentration of bulk solution was 0.5 mM for 500 μM menadione solution experiment. (D): Thiodione response to 500 μM menadione added to HeLa cells for 160 min (solid circle points). Solid line represents the simulated curve.

MK571 Inhibition Experiments: The Petri dish with appropriate cell coverage was removed from the incubator and incubated on the SECM stage in buffer-only solution as described above. The cells were then further incubated for 1 h in 50 μM MK571 buffer solution, which were then replaced by 50 μM MK571 and 500 μM menadione solutions. The procedures thereafter were similar to those described above.

QCRL-4 Antibody Blocking Experiments: The cells were cultured in a 1 cm diameter spot over a tissue-culture Petri dish for 16 h inside the cell culture incubator as described in the Cell Culture section. The following antibody transfection procedure was performed for one dish only. 20 μL of antibody solution (4 μg) was mixed thoroughly with 4 μL Lipodin-Ab solution and incubated for 15 min at room temperature. 100 μL of medium-only (without serum) solution was added to the antibody/Lipodin-Ab solution, and then immediately added to the cells. The cells were washed with 100 μL medium-only solution once before the antibody/Lipodin-Ab solution was added. The dish was then put back in the incubator for 5-6 h, then removed and washed twice with 400 μL of buffer. The dish was put on the SECM stage and incubated there for 1 h at room temperature. The buffer was replaced with 400 μL of 1 mM ferrocene methanol solution to perform an approach curve within 10-15 min. The tip-to-substrate distance was fixed at 80 μm . The cells were washed thrice with buffer solution after replacing the ferrocene methanol solution. A 500 μL drop of menadione solution was then added to the marked 1 cm spot of cells. Cyclic voltammograms were recorded between -0.65 to +0.65 V over 2 min intervals for 30 min.

Simulation Model

A schematic view of the simulation model is shown in Figure 3.2C. The model was used to determine the kinetics of menadione uptake and thiodione release by a monolayer of living HeLa cells. We assumed the cells formed a perfect monolayer in the

simulation model. The simulation was done in axial symmetry coordinates using Comsol Multiphysics software (Figure 3.3). The flux of menadione passing through the cell membrane was taken as $\pm k_{in} * (M-M1)$ where, M and $M1$ (mol/m^3) are the menadione concentrations outside and inside the cell; k_{in} (m/s) represents the kinetics of menadione uptake by live cells. The flux of menadione was considered in both directions between inside and outside the cell, because the movement of menadione molecules was taken as purely driven by the concentration gradient. Flux of thiodione through the cell membrane was considered as $k_{out} * (T1-T)$ where, $T1$ and T represent the thiodione concentrations inside and outside the cell; k_{out} represents kinetics of MDR-pump-mediated thiodione transport through cellular membrane. Here the flux was considered unidirectional, since the thiodione molecules were only being pumped out of the cells by the ATP-driven MDR pumps. Initially there is no menadione present inside the cell, and the tip was held at a potential where the reaction, thiodione oxidation, was diffusion controlled at all times.

We assumed that the thiodione present in the solution undergoes simple two-electron transfer as shown below, and the tip was held at diffusion-controlled potential to avoid any kinetics complications.



Where, T represents thiodione species.

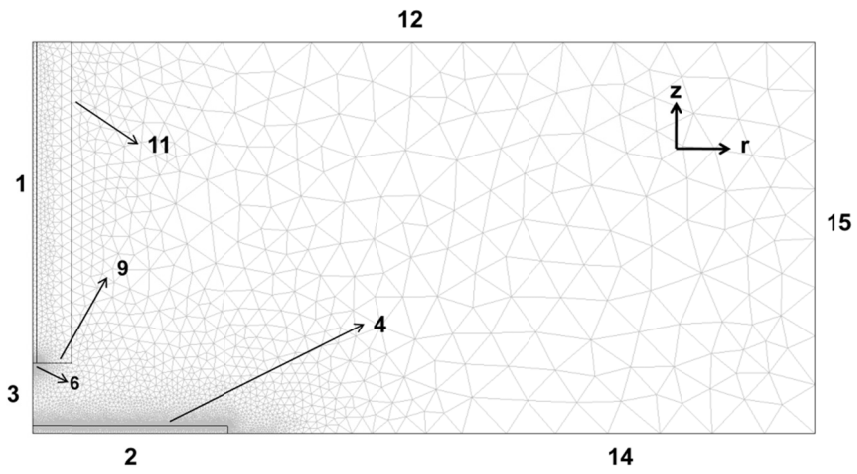


Figure 3.3: The mesh distribution of Comsol Multiphysics model in 2-D axial symmetry.

Since the redox species T and oxidized T moved toward and away from the electrode surface only by concentration gradient, Fick's second law of diffusion was used in the simulation. The concentration of species T was given as $c_T(r,z,t)$ and the diffusion equation in cylindrical coordinates was described as

$$\frac{\partial c_R}{\partial t} = D \left(\frac{\partial^2 c_R}{\partial r^2} + \frac{1}{r} \frac{\partial c_R}{\partial r} + \frac{\partial^2 c_R}{\partial z^2} \right)$$

Where, r and z are the coordinates as shown in Figure 3.3; t represents time; c and D represent the concentration and diffusion coefficient of species R. The other species used in the simulation were as follows: M = menadione outside cell; M1 = menadione inside cell; T = thiodione outside cell; T1= thiodione inside cell; G = glutathione inside cell

The simulation model described above was solved by a finite element method where the mesh was increased in exponential grid fashion to generate a two-dimensional grid. Finer mesh distribution was used at the regions where sharp changes in the concentration gradients were noticed. The details about the boundary conditions are described in table below (Table 3.1):

Boundary in COMSOL model	Description	Boundary Conditions
1, 3	Axial symmetry	Symmetry
6	Electrode Surface	$T = 0$
2, 9,11 & 14	Insulation sheath	Insulation
4	Cellular membrane	Flux of M = $-k_{in}*(R-R1)$ Flux of M1= $k_{in}*(R1-R)$ Flux of T= $P*(T1-T)$
12 & 15	Bulk Solution	$T = 0$ $M = 0.5$

Table 3.1: The boundaries in comsol multiphysics model showed in figure 3.3 and their corresponding boundary conditions.

Initially the menadione concentration inside the cell was zero and the concentration in the bulk solution was 0.5 mM or 0.5 mol/m³. Appropriate menadione concentration was used for other thiodione concentration curve fitting. The diffusion coefficient of menadione outside the cell was considered as 8×10⁻¹⁰ m²/s and the diffusion coefficient of all species inside cell was assumed as 1×10⁻¹⁰ m²/s. The tip (RG=10) was located at 100 μm away from the substrate or 90 μm from cell surface. The current at the electrode was determined by

$$I_{\text{tip}} = \int_{r=0}^{r=a} 2\pi n F D_T r \frac{\partial c_T}{\partial z} dr$$

Where, n = 1; F= 96485 C/mol; and D_T = 4×10⁻¹⁰ m²/s; a = tip radius, m

The rate constant for homogeneous reaction between menadione and GSH was assumed to be fast, on the order of 4 to 6 × 10⁻³ s⁻¹, to maintain a balance between menadione diffusing inside the cell and undergoing conjugation reaction and thus avoiding any negative concentration both inside and outside cell. The adjusted parameters for three different concentrations of menadione are given in the table below (Table 3.2):

	Menadione Concentration		
	500 μM	250 μM	125 μM
Rate of menadione uptake, m/s	1.6×10^{-8}	1.6×10^{-8}	1.6×10^{-8}
Rate of thiodione transport, m/s	1.6×10^{-7}	1.6×10^{-7}	1.6×10^{-7}
Rate of homogeneous reaction, s^{-1}	4	5	6
Glutathione concentration, mol/m^3	20	10	5

Table 3.2: The fitted simulation parameters for respective menadione concentration.

3.3 RESULTS

Cytotoxicity Experiments

Cell viability tests showed that in the presence of 500 μM menadione (Figure 3.4) less than 40% of the cells were alive after 3 h; whereas viability was unaffected during a 60 min period. Hence all SECM experiments were performed within a 60 min time frame. Based on a viability assay (Figure 3.5) the HeLa cells maintained membrane integrity for 30 min after addition of 50 μM MK571 and 500 μM menadione. Hence, the cells were incubated for 60 min in 50 μM MK571 solution before replacing the solution with a suitable MK571 and menadione mixture for SECM experiments.

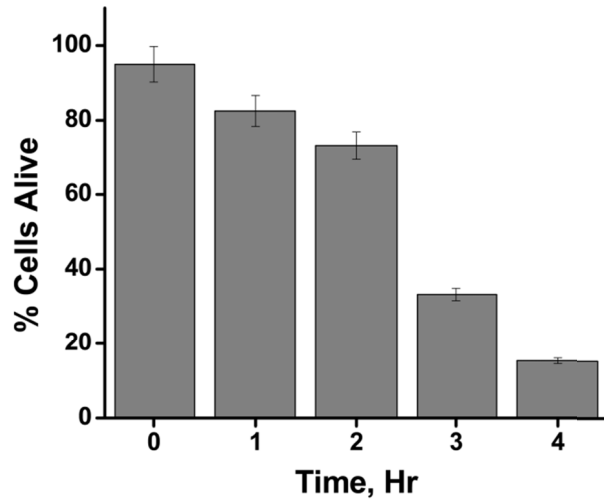


Figure 3.4: Cellular viability w.r.t time (h) in presence of 500 μM menadione in buffer solution.

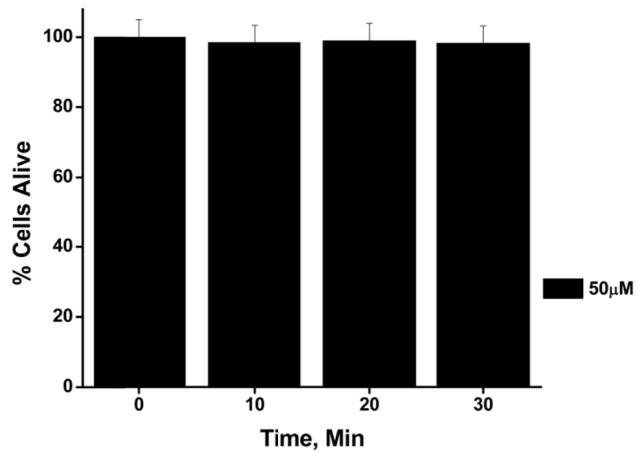


Figure 3.5: Cellular viability w.r.t time (min) on exposure of 500 μM menadione and 50 μM MK571.

The cells were incubated in 50 μM MK571 solution for 60min before adding menadione and MK571 solution.

Thiodione Flux from a Monolayer of HeLa Cells

The cellular response of varying concentration of menadione (500, 250, 125 μM) with time (min) is shown in Figure 3.2B. The thiodione concentration was detected with a 10 μm Pt tip at a distance of about 90 μm away from the cellular monolayer. The concentration was calculated from the cyclic voltammetry recorded at approximately one-minute intervals as shown in Figure 3.6. The current at +0.4 V was converted into concentration using the equation $i_{ss} = 4nFaDC^*$, where a is the radius of the electrode, D is the diffusion coefficient and C^* is the concentration. A gradual increase of thiodione concentration was recorded for 20 min after addition of 500 μM menadione, after which the concentration reached a quasi-steady state of 140 μM (Figure 3.2B). Quasi-steady state thiodione concentrations of 70 μM and 35 μM were also recorded for 250 μM and 100 μM menadione additions respectively. Assuming a constant flux of thiodione through the cellular monolayer at quasi-steady state, the number of molecules pumped out of the cells on exposure of 500 μM of menadione was calculated to be 2.6×10^{-17} moles/cell/s or 16×10^6 molecules/cell/s.

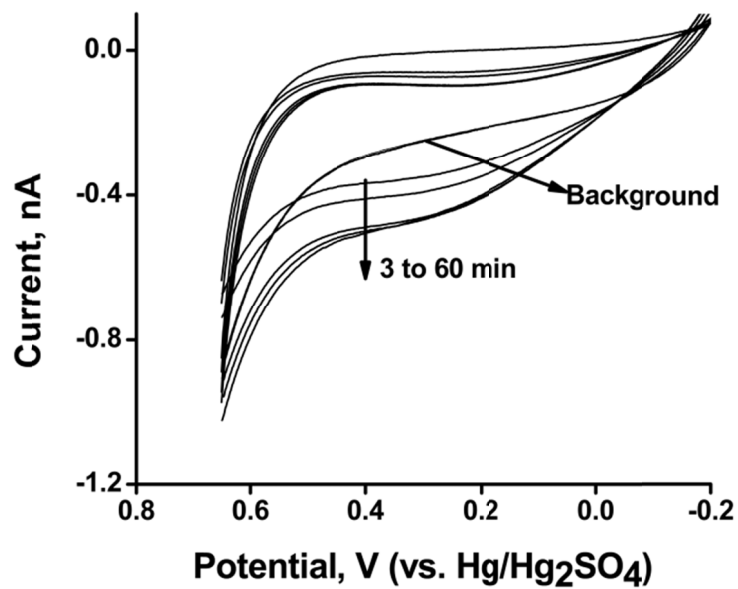


Figure 3.6: Cyclic voltammetry of thiodione efflux coming out from the monolayer of HeLa cells on exposure to 500 μ M menadione.

Tip: 10 μ m Pt; Counter: 0.5 mm Pt; Reference: Hg/Hg₂SO₄.

Model of Thiodione Release

Figure 2B shows the fitting of experimental (dotted points) and simulated response (solid lines) for a monolayer of HeLa cells in the presence of 500, 250 and 125 μM menadione. The kinetics of menadione uptake was 1.6×10^{-8} m/s, and rate of thiodione pumping out was calculated to be 1.6×10^{-7} m/s. The rate constant for the homogenous reaction between menadione and glutathione was adjusted to be between 4 to 10 s^{-1} and that of the intracellular glutathione concentration between 20 to 5 mol/m^3 for varying concentrations of menadione exposure. The simulation parameters were determined using 60 min (short-time) simulations. The comparison of simulation and experiment for long-time (160 min) SECM of 500 μM menadione response is shown in Figure 3.2D. Except for the duration, all simulation parameters were the same as the short-time simulation.

Inhibition of MRP1 Pump by MK571

Figure 3.7 shows the thiodione efflux from a monolayer of cells in the absence and presence of varying concentrations of MK571, a LTD_4 receptor antagonist and a notable MRP1 inhibitor. The thiodione concentration was observed to be $50 \mu\text{M} \pm 10 \mu\text{M}$ in presence of 50 μM MK571 and 500 μM menadione. The cells were incubated in 50 μM MK571 for 60 min before adding any menadione-MK571 solution. The control experiment was done following the same protocol except without any menadione in the solution.

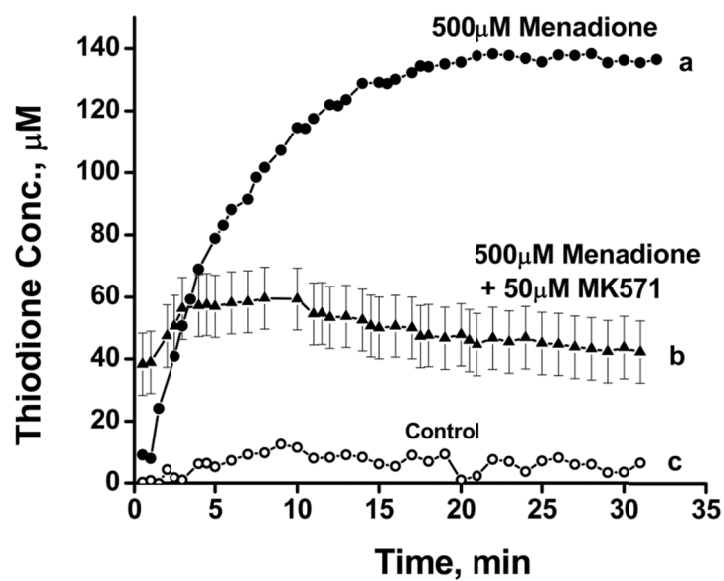


Figure 3.7: Cellular response to 500 μM menadione in presence of MK571 blocker

(a) The thiodione efflux from a monolayer of HeLa cells in the absence of MRP1 blocker MK571. (b) Thiodione concentration in the presence of 50 μM of MK571 and 500 μM menadione. (c) Control experiment in the presence of MK571 blocker. All the experimental conditions were the same except the control current was recorded without any menadione in the solution.

Inhibition of MRP1 Pump by QCRL-4 Antibody

Figure 3.8 shows the normalized thiodione concentration vs. time (min) in the absence (a) and presence (b) of QCRL-4 antibody. The effluxed thiodione concentration showed a drop of 50% when transfected with QCRL-4 antibodies. The thiodione concentration was normalized against the average thiodione concentration produced using the same set of experiments in the presence of 500 μM menadione without any blocker. The thiodione concentration was normalized due to variation of thiodione efflux from one set of experiments to another. The thiodione concentration (μM) vs. time (min) plots for four sets of independent experiments are given in the (Figure 3.9). In all four experiments in the Figure 3.9 (A-D), the thiodione concentration dropped on the average from $100 \pm 10 \mu\text{M}$ to $50 \pm 10 \mu\text{M}$ after the cells were transfected with QCRL-4 antibodies. A fluorescence-based viability test was also performed with transfected HeLa cells by adding 500 μM menadione. No additional loss in cell viability was observed beyond that observed due to addition of 500 μM menadione alone to non-transfected HeLa cells (Figure 3.4).

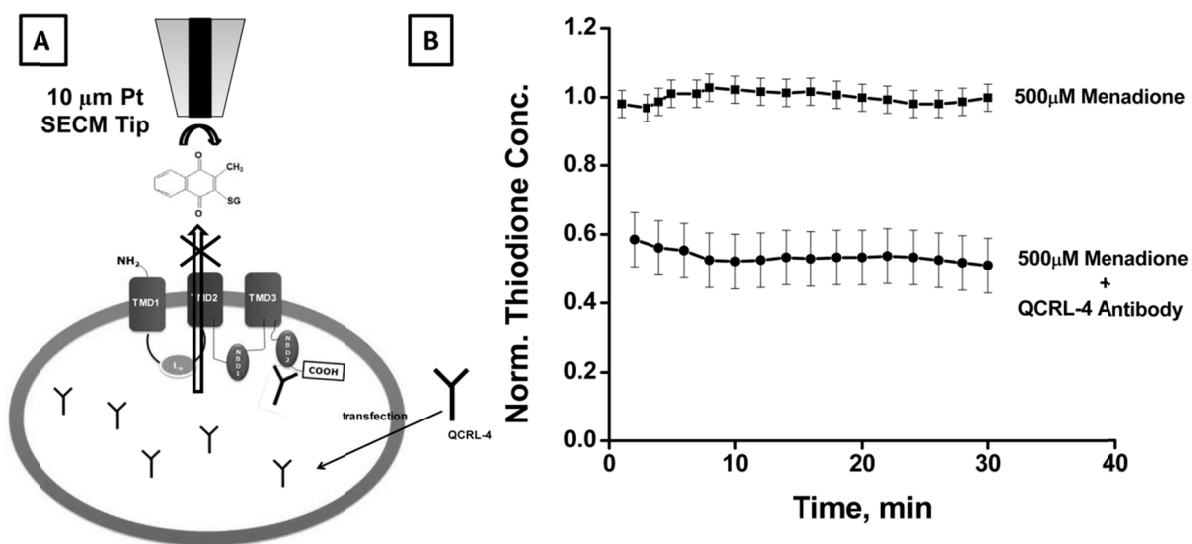


Figure 3.8: Cellular response to 500 μM menadione in presence of antibody based blocker

(A) Schematic diagram (not to scale) of transfection of QCRL-4 monoclonal antibody and subsequent binding to NBD2 domain of MRP1 pump. (B) Normalized thiodione concentration in presence of 500 μM menadione (a) without and (b) with antibody QCRL-4. Thiodione concentration is normalized against the average thiodione concentration produced in each individual experiment without any blocker antibody. Tip was positioned at 80 μm distance from Petri dish to record the thiodione efflux.

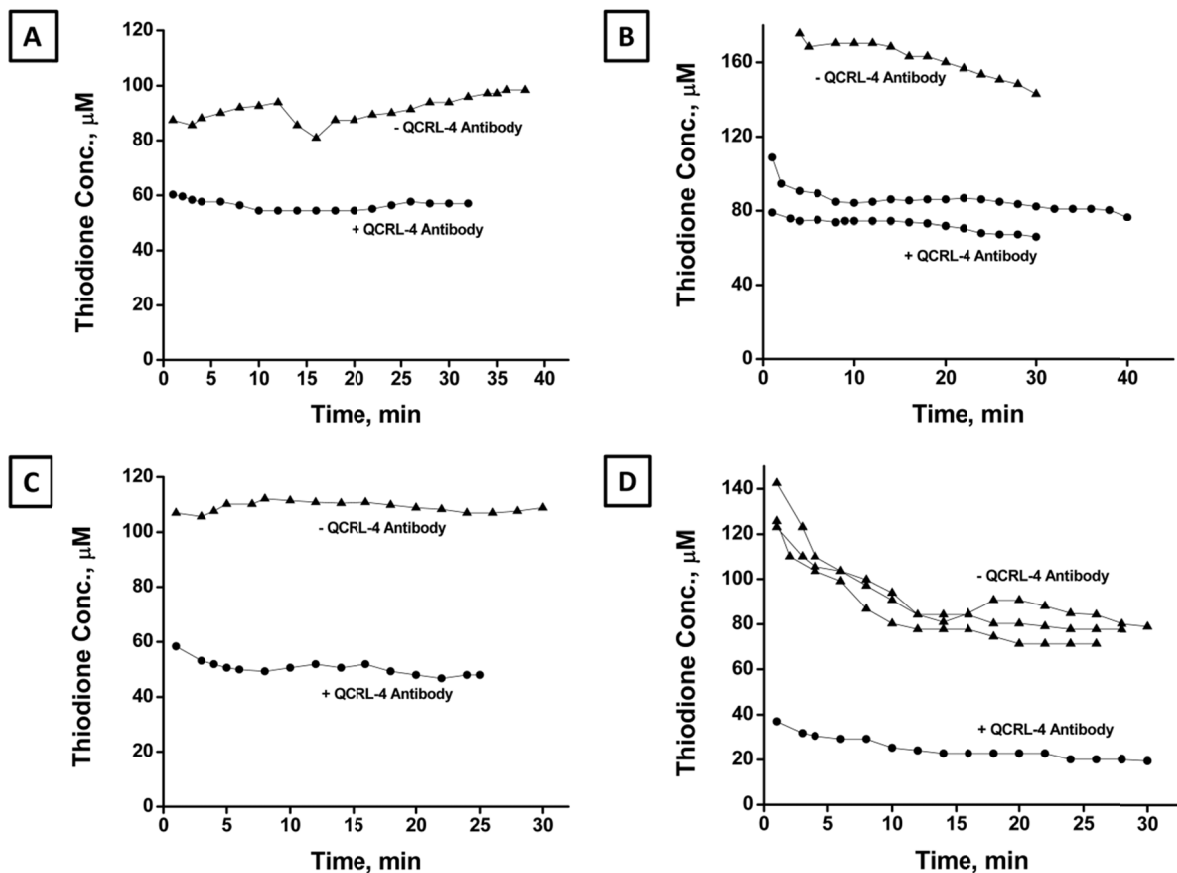


Figure 3.9: Thiodione concentration (μM) w.r.t time (min) in presence of QCRL-4 antibody

Thiodione concentration (μM) w.r.t time (min) when exposed to $500 \mu\text{M}$ menadione to transfected (solid circle) and non-transfected (solid triangle) HeLa cells with QCRL-4 antibody. (A-D) represents four independent set of experimental data. Tip-substrate distance in each experiment was maintained at $80 \mu\text{m}$.

3.4 DISCUSSION

Cellular Response to Menadione Induced Oxidative Stress

Quantitative detection of thiodione efflux (Figure 3.2B) due to the addition of menadione to HeLa cells confirmed the schematic model proposed in Figure 3.1. Menadione, an arylator and redox cycling molecule, can induce oxidative stress in HeLa cells by forming reactive oxygen species and highly destructive hydroxyl radicals. To protect itself from such oxidative stress, the cell maintains a pool of GSH in mM concentration. When the hydrophobic molecule menadione enters a live cell, it oxidizes the GSH and also forms GS-conjugates, thiodione, in the presence of the GST enzyme. This causes a disruption in the GSH/GSSG ratio as well as depletion of GSH. Thiodione formed inside the cell is recognized by the transmembrane MRP1 pump by its glutathione moiety and transported out of HeLa cells in an ATP-driven process. The extracellular thiodione in solution is then detected by an SECM tip located 80-90 μm away from the cells. Figure 2B shows such a cellular response upon exposure to varying concentrations of menadione and the resulting build-up of the thiodione concentration over the cellular monolayer in the extracellular environment. The gradual increase in thiodione concentration and maintenance of a quasi-steady state for 60 min also confirms that the thiodione is transported out of a cell in a controlled ATP-driven process instead of diffusing out of a leaking cell membrane. The cell is able to protect itself from oxidative stress for 60 min in the presence of 500 μM menadione. In addition, the viability and existence of intact cell membranes of the HeLa cells is also supported by an independent test of viability based on cell membrane integrity (Figure 3.4).

The detection of the varying concentration of thiodione (Figure 2B) outside cells suggests that thiodione transport is not only a controlled, ATP-driven, MDR-mediated process, but also that a live cell is able to up-regulate and down-regulate thiodione

transport as necessary. The cell is able to regulate transport by recruiting more MDR proteins (produced from golgi) in its membrane, as well as modulating its GSH-producing enzyme,(24) which may contribute to increased thiodione flux.

As shown in Figure 3.2B, thiodione has been effluxed to a concentration of 140 μM upon addition of 500 μM menadione, which is only 28% of the menadione concentration exposed. A similar response has been observed for 250 and 125 μM menadione exposure. In general the menadione concentration outside the cell should ultimately reach near the intracellular menadione concentration, which should lead to a higher thiodione concentration than that measured. Such a contrast has been reported before by our group (36, 37) for menadione transport with yeast and hepatoblastoma cell lines. For liver cancer cells the thiodione efflux recorded to be 100% of menadione exposed, whereas for yeast it is only reported to be 10% of the menadione exposed. This contrast may be due to the way a particular cell functions.

The thiodione molecule produced inside the cell enzymatically also retains the recycling property and has the ability to produce more superoxide or hydroxyl radical, and thus prove toxic to the cell. Therefore, any accumulated thiodione, in addition to any menadione present inside the cell, can also contribute to lipid peroxidation. A living cell can only survive under such a stressed condition if it can keep up with the rate of production of sacrificial GSH by pumping out thiodione. This may explain why the cell viability dropped from 70% to below 40% (viability assay) during a 2 to 3 h time period as well as from a long time (60 min) SECM experiment. Figure 3.2D shows further the monotonic rise of thiodione concentration outside the cell monolayer until 240 min after reaching a quasi steady state at 60 min. This could be taken as the beginning of uncontrolled leaking of thiodione outside the cell due to lipid peroxidation of cellular membrane. In addition, the trypan blue viability assay also confirms the rupture of cell membrane after 120 min due to the addition of 500 μM menadione.

Model of Thiodione Efflux from a Monolayer of HeLa Cells

To elucidate the processes occurring inside the cell, a mathematical model was proposed to represent the kinetics of menadione uptake and thiodione pumping out of cells (Figure 3.2C). The simulated fitted thiodione response curve (solid line) with respect to time (min) is shown in Figure 3.2B for 500, 250 and 125 μM menadione concentration exposure. The calculated kinetics value of thiodione transport is 1.6×10^{-7} m/s, 10 times faster than menadione uptake. The higher value of thiodione transport may represent an ATP-driven detoxification pathway; in contrast to menadione uptake which is solely a concentration gradient diffusion phenomenon across the cell membrane. A similar rate of thiodione pumping larger than menadione influx was found in earlier studies with yeast and heptablastoma cells (36, 37).

Figure 3.2D shows the simulated fitting (solid line) of the gradual increase in thiodione concentration during a 160 min time interval due to the addition of 500 μM menadione to HeLa cells. Such a thiodione response was explained in the previous section as leaking due to collapse of a cellular membrane. In the simulation it is represented by uncontrolled increase of thiodione above the cells.

Selective Blocking of MRP1 by MK571

Figure 3.7 shows a significant drop in thiodione efflux concentration from 140 μM to $50 \mu\text{M} \pm 10 \mu\text{M}$ in the presence of 50 μM MK571 along with 500 μM menadione. This drop in thiodione efflux was not due to dead cells as the independent viability assay (Figure 3.5) shows 90% of cells were alive during experimental period of 30 min. The viability assay also shows that MK571 by itself is toxic to the cell and does affect the cell membrane integrity. When the cells were incubated with 50 μM MK571, it could permeate through the cell membrane and enter the cell cytoplasm, affecting the

golgi body for producing and recruiting transmembrane proteins to the cell membrane. As mentioned above, the live cell undergoes rapid redistribution of transmembrane proteins or MRP pumps from the golgi body to the cytoplasm to the plasma membrane upon exposure to low concentrations of xenobiotics. In other words, exposure to a low concentration of menadione up-regulates the MRP1 expression and stimulates GSH synthesis. But when cells are exposed to MK571, it prevents such early translocation of MRP1 proteins mostly localized in the golgi (24). Hence the cell will have fewer pumps to transport thiodione outside of the cell, which in turn should contribute to less thiodione in the extracellular environment. In addition MK571, a LTD₄ receptor antagonist, also has the ability to competitively bind with the MRP1 inner leaflet drug binding site, decreasing the thiodione efflux. It can decrease both the flux of GSH as well as the drug efflux. The reduction in thiodione flux, demonstrates that thiodione is indeed pumped out of the cells by the MRP1 pumps.

Selective Blocking of MRP1 by QCRL-4 Antibody

As shown in Figures 3.8 and 3.9, the QCRL-4 antibody can be used to selectively block the MRP1 pump in a live intact HeLa cell. When delivered inside the cell, QCRL-4 binds to the epitope 1294-1531 of the MRP1 protein, which is in proximity to the -COOH second nucleotide binding domain (NBD2) site. This QCRL-4 antibody, once bound to the ATP binding site, prevents the MRP1 pump from changing its configuration, thus stopping any transport outside the cells. The specificity of QCRL-4 has been studied extensively by Hipfner and Cole et. al by immunoblotting and immunoprecipitation methods(30, 35) to show that this antibody selectively binds with the MRP1 protein sequence but not with any other protein such as Pgp. The monoclonal antibodies QCRL-2, -3, -4 have been shown to inhibit the transport of endogenous substrates such as LTC₄ and 17 β -estradiol 17-(β -D-glucuronide) besides externally administered drugs such as

daunorubicin and vincristine.(13, 19, 32, 33) In the above-mentioned studies, complete or near complete inhibition of uptake of these substrates by the MRP-enriched inside out plasma membrane vesicles has been reported. However, in our study thiodione efflux dropped from $100 \pm 10 \mu\text{M}$ to $50 \pm 10 \mu\text{M}$ from non-transfected to transfected live and intact HeLa cells. Here, such a difference is obvious as our study was done with live HeLa cells. To deliver the antibodies inside a live cell, one has to take into account the transfection efficiency of antibodies for a particular cell line. We assume in our case the transfection efficiency was about 50%. In addition, the live cell environment is dynamic and it can up-regulate and down-regulate MDR protein production when subjected to oxidative stress. In this study we have shown that if a sufficient amount of blocking antibodies are present inside the cells, the transporting functions of the MRP1 pumps can be impaired. This is confirmed with the 50% drop in thiodione efflux from transfected live HeLa cells in comparison to the non-transfected ones (Figure 3.8). This is one of the few studies where the thiodione efflux has been quantitatively determined to be decreased, overcoming the multidrug resistance phenomenon in live cells in the presence of a xenobiotic such as menadione and monoclonal antibodies simultaneously.

3.5 CONCLUSION

When added to HeLa cells, menadione can permeate inside an intact cell due to its hydrophobic nature, and can induce oxidative stress. HeLa cells were observed to form GS-conjugates or thiodione in the presence of the GS-transferase. Thiodione was then recognized by MRP1 pumps due to its glutathione moiety, and subsequently pumped outside to the extracellular environment. This extracellular thiodione was then detected quantitatively in real time by a SECM tip positioned 80 to 90 μm above the cellular monolayer. The quasi-steady state thiodione concentrations were 140, 70 and 35 μM after addition of 500, 250 and 125 μM menadione to the cells, respectively. Assuming a

constant thiodione flux, approximately 16×10^6 molecules were calculated to be pumped out of a single cell due to the addition of 500 μM menadione. The cells were able to up-regulate or down-regulate their MRP1 pumps to modulate the thiodione efflux accordingly to the menadione exposure. In this study, MK571, a known MRP1 blocker, was used to demonstrate that MRP1 was the major carrier for thiodione transport in live HeLa cells. The extracellular thiodione concentration was shown to decrease to $40 \pm 10 \mu\text{M}$ in presence of the class-I inhibitor, MK571. This confirmed that MRP1 pumps require the GSH moiety as a substrate to pump out any xenobiotics as a detoxification process. Additional experiments with MRP1-specific antibody QCRL-4 showed that it could selectively recognize the NBD2 binding site of MRP1; thus inhibiting the ATP-mediated thiodione efflux from live intact cells in the presence of menadione. Thiodione flux from transfected live HeLa cells was observed to drop by 50% from $100 \pm 10 \mu\text{M}$ to $50 \pm 10 \mu\text{M}$ in the presence of QCRL-4 monoclonal antibodies. This study henceforth can be extended to different antibodies capable of recognizing different epitopes of MRP1 in live intact cells. This would eventually help us to understand mechanistically the functions of these MDR pumps in live cells, pumping out different xenobiotics or chemotherapeutic agents. In the future, SECM can also be extended to identify any specific MDR pump for a particular xenobiotic transport used by a particular type of cell. It can also be used for rapid screening of different MRP1 blockers for a particular anti-cancer chemotherapeutic drug; and assist in designing pump inhibitors.

3.6 ACKNOWLEDGEMENT

Allen J Bard and Dipankar Koley thank National Science Foundation (CHE) for support of this work.

3.7 REFERENCES

- ¹ Higgins CF (2007) Multiple molecular mechanism for multidrug resistance transporters. *Nature* 446:749-757.
- ² Hooijberg JH, et al. (2000) The effect of glutathione on the ATPase activity of MRP 1 in its natural membranes. *FEBS Lett* 469:47-51.
- ³ Paul S, Breuninger LM, Tew KD, Shen H, Kruh GD (1996) ATP-dependent uptake of natural product cytotoxic drugs by membrane vesicles establishes MRP as a broad specificity transporter. *Proc Natl Acad Sci USA* 93:6929-6934.
- ⁴ Seung S, Lee JY, Lee MY, Park JS, Chung JH (1998) The relative importance of oxidative stress versus arylation in the mechanism of quinone –induced cytotoxicity to platelets. *Chem Biol Interact* 113:133-144.
- ⁵ Hultberg B, Anderson A, Isaksson A (1999) Thiol and redox reactive agents exert different effects on glutathione metabolism in HeLa cells culture. *Clin Chim Acta*, 283:21-32.
- ⁶ Monks TJ, Lau SS (1997) Biological reactivity of polyphenolic-glutathione conjugates. *Chem Res Toxicol* 10:1296-1313
- ⁷ Miller MG, Rodgers A, Cohen GM (1986) Mechanisms of toxicity of naphthoquinones to isolated hepatocytes. *Biochem Pharmacol* 35:1177-1184.
- ⁸ Eaton DL, Bammler TK (1999) Concise review of the glutathione S-Transferases and their Significance to Toxicology. *Toxicol Sci* 49:156-164.
- ⁹ Mueller CFH, et al. (2005) The role of multidrug resistance protein-1 in modulation of endothelial cell oxidative stress. *Circ Res* 97:637-644.
- ¹⁰ Roelofsen H, Hooiveld GJEJ, Koning H, Havinga R, Jansen PLM (1999) Glutathione S-conjugate transport in hepatocytes entering the cell cycle is preserved by a switch in expression from the apical MRP2 to the basolateral MRP1 transporting protein. *J Cell Sci* 112:1395-1404.
- ¹¹ Zaman GJR, et al. (1995) Role of glutathione in the export of compounds from cells by the multidrug resistance-associated protein. *Proc Natl Acad Sci USA* 92:7690-7694.
- ¹² Muller M, et al. (1994) Overexpression of the gene encoding the multidrug resistance-associated protein results in increased ATP-dependent glutathione S-conjugate transport. *Proc Natl Acad Sci USA* 91:13033-13037.
- ¹³ Renes J, Vries EGE, Nienhuis EF, Jansen PLM, Muller M (1999) ATP-and glutathione-dependent transport of chemotherapeutic drugs by the multidrug resistance protein MRP1. *Br J Pharmacol* 126:681-688.
- ¹⁴ Hipfner DR, Deeley RG, Cole SPC (1999) Structural, mechanistic and clinical aspects of MRP1. *BBA* 1461:359-376.
- ¹⁵ Jedlitschky G, et al. (1996) Transport of glutathione, glucuronate and sulfate conjugates by the MRP gene-encoded conjugate export pump. *Cancer Res* 56:988-994.

- ¹⁶ I. Leier, et al. (1994) The MRP gene encodes an ATP-dependent export pump for Leukotriene C4 and structurally related conjugates. *J Biol Chem* 269:27807-27810.
- ¹⁷ Shen H, et al. (1996) Cellular and in-vitro transport of glutathione conjugate by MRP. *Biochemistry* 35:5719-5725.
- ¹⁸ Karla PK, Pal D, Quinn T, Mitra AK (2007) Molecular evidence and functional expression of a novel drug efflux pump (ABCC2) in human corneal epithelium and rabbit cornea and its role in ocular drug efflux. *Int J Pharm* 336:12-21.
- ¹⁹ Tabas LB, Dantzig AH (2002) A high-throughput assay for measurement of multidrug resistance protein-mediated transport of leukotriene C4 into membrane vesicles. *Anal Biochem* 310:61-66.
- ²⁰ Decory HH, Dumas KMP, Sheu SS, Federoff HJ, Anders MW (2001) Efflux of glutathione conjugate of monochlorobimane from striatal and cortical neurons. *Drug Metab Dispos* 29:1256-1262.
- ²¹ Tabas LB, Dantzig AH (2002) A high-throughput assay for measurement of multidrug resistance protein-mediated transport of leukotriene C4 into membrane vesicles. *Anal Biochem* 310:61-66.
- ²² Rigato I, Pascolo L, Ferneti C, Ostrow JJD, Tiribelli C (2004) The human multidrug-resistance-associated protein MRP1 mediates ATP-dependent transport of unconjugated bilirubin. *Biochem J* 383:335-341.
- ²³ Gekeler V, Ise W, Sanders KH, Ulrich WR, Beck J (1995) The Leukotriene LTD4 receptor antagonist MK571 specifically modulates MRP associated multidrug resistance. *Biochem Biophys Res Commun* 208:345-352.
- ²⁴ Gennuso F, et al. (2004) Bilirubin protects astrocytes from its own toxicity by inducing up-regulation and translocation of multidrug resistance-associated protein 1 (Mrp1). *Proc Natl Acad Sci USA* 101:2470-2475.
- ²⁵ Salerno M, Loechariyakul P, Saengkhae C, Suillerot AG (2004) Relation between the ability of some compounds to modulate the MRP1-mediated efflux of glutathione and to inhibit the MRP1-mediated efflux of daunorubicin. *Biochem Pharmacol* 68:2159-2165.
- ²⁶ Jeong EJ, Jia X, Hu M (2005) Disposition of formononetin via enteric recycling: Metabolism and excretion in mouse intestinal perfusion and caco-2 cell models. *Mol Pharmaceutics* 2:319-328.
- ²⁷ Hipfner DR, Gauldie SD, Deeley RG, Cole SPC (1994) Detection of the Mr 190,000 Multidrug resistance protein, MRP, with monoclonal antibodies. *Cancer Res* 54:5788-5792.
- ²⁸ Hipfner DR, Almquist KC, Stride BD, Deeley RG, Cole SPC (1996) Location of a protease-hypersensitive region in the multidrug resistance protein (MRP) by mapping of the epitope of MRP-specific monoclonal antibody QCRL-1. *Cancer Res* 56:3307-3314.

- ²⁹ Hipfner DR, Mao Q, Qui W, Leslie EM, Gao M, Deeley RG, Cole SPC (1999) Monoclonal antibodies that inhibit the transport function of the 190-kDa multidrug resistance protein, MRP. *J Biol Chem* 274:15420-15426.
- ³⁰ Hipfner DR, Deeley RG, Cole SPC (1999) Structural mechanistic and clinical aspects of MRP1. *Biochim Biophys Acta* 1461:359-376.
- ³¹ Scheffer GL et. al. (2000) Specific detection of multidrug resistance proteins MRP1, MRP2, MRP3, MRP5, and MDR3 P-Glycoprotein with a panel of monoclonal antibodies. *Cancer Res* 60:5269-5277.
- ³² Loe DW, Almquist KC, Deeley RG, Cole SPC (1996) Multidrug resistance protein (MRP)-mediated transport of leukotriene C4 and chemotherapeutic agents in membrane vesicles. *J Biol Chem* 271:9675-9682.
- ³³ Loe DW, Deeley RG, Cole SPC (1998) Characterization of vincristine transport by the Mr 190,000 multidrug resistance protein (MRP): Evidence for cotransport with reduced glutathione. *Cancer Res* 58:5130-5136.
- ³⁴ Hipfner DR, Gao M, Scheffer, Scheper RJ, Deeley RG, Cole SPC (1998) Epitope mapping of monoclonal antibodies specific for the 190-kDa multidrug resistance protein (MRP). *Br J Pharmacol* 78:1134-1140.
- ³⁵ Cole SPC and Deeley RG (1998) Multidrug resistance mediated by the ATP-binding cassette transporter protein MRP. *BioEssays* 20:931-940.
- ³⁶ Mauzeroll J, Bard AJ (2004) Scanning electrochemical microscopy of menadione-glutathione conjugate export from yeast cells. *Proc Natl Acad Sci USA* 101:7862-7867.
- ³⁷ Mauzeroll J, Bard AJ, Owhadian O, Monks TJ (2004) Menadione metabolism to thiodione in hepatoblastoma by scanning electrochemical microscopy. *Proc Natl Acad Sci USA* 101:17582-17587.
- ³⁸ Bard AJ, Mirkin MV, Eds., Scanning Electrochemical Microscopy; Mercel Dekker, New York, 2001 p 75.

CHAPTER 4: Quorum Sensing & Electrochemistry: as Studied with *Pseudomonas aeruginosa* Biofilm using SECM

ABSTRACT

Phenazine derivatives such as pyocyanin (PYO) are produced by *P. aeruginosa* in early stationary phase. PYO production is induced by the quorum sensing (QS) signaling pathway of *P. aeruginosa*. PYO is an electroactive compound, which shows a reversible two-electron wave at $E_{1/2} = -0.04$ (vs. NHE). Real time quantitative detection of PYO produced by a *P. aeruginosa* biofilm was achieved by scanning electrochemical microscopy (SECM). Biofilm production of 60 μM PYO was measured using square wave voltammetry with a 10 μm Pt tip located at a distance of 20 μm from the biofilm surface. Spatial mapping of reduced and oxidized PYO produced by a *P. aeruginosa* biofilm has been achieved by SECM. We find that PYO produced by the *P. aeruginosa* biofilm is present primarily in reduced form and it maintains a reduced layer above the biofilm even in the presence of oxygen. The cyclic voltammetry inside and outside the reduced PYO layer confirmed 100% reduced PYO inside the layer at 37°C. It is hypothesized that bacteria are able to modulate this reduced PYO layer to scavenge iron from the surrounding environment. We demonstrate that electron flow from substrate oxidation to PYO reduction is dependent upon cytochrome bc1 and the activity of the *napA* nitrate reductase.

4.1 INTRODUCTION

Pseudomonas aeruginosa

P. aeruginosa is a Gram-negative bacterium whose dimensions are 0.5 to 0.8 μm by 1.5 to 3.0 μm . It is motile due to presence of a single polar flagellum and is generally found in soil and water environments. Most importantly, it is an opportunistic pathogen to humans where it exploits deficiencies in the host immune system to initiate an infection. *P. aeruginosa* is a model opportunistic pathogen for biofilm study as well as is of clinical importance in infections of cystic fibrosis, neutropenia, AIDS, cancer and burn patients. *P. aeruginosa* is a model organism in the study of quorum sensing (QS) and biofilm formation. At high cell densities, QS controlled signaling pathways induce *P. aeruginosa* to produce a distinguishing phenazine compound pyocyanin (PYO) in addition to several other phenazines which will be discussed in this introduction.

Quorum Sensing

Quorum sensing has been described as “the regulation of gene expression in response to fluctuations in cell-population density. Quorum sensing is a cell-cell communication process in which bacteria use the production and detection of extracellular chemicals called autoinducers to monitor cell population density.” (1)

Studies (1, 2) have shown that quorum sensing plays an integral role in shaping bacterial behavior in a population of its own species (intra-species) or other species (inter-species). Both Gram-positive and Gram-negative bacteria exhibit quorum sensing. A typical quorum sensing circuit diagram of Gram-negative bacteria is shown in Figure 4.1. For Gram-negative bacteria, acyl homoserine lactones (AHL) are major autoinducer signals especially for intra-species quorum sensing. AHL molecules consist of homoserine lactone as core molecules with the acyl chain modification and chain length varying from C4 to C18 depending on the bacterial species (Figure 4.2). In general

bacteria produce AHL molecules (produced by LuxI or homologues that catalyze acylation and lactonization reactions between the substrates S-adenosylmethionine (SAM) and hexanoyl-ACP) at all times and diffuse out into the extracellular environment when bacterial density is low. However, when the bacteria reach a high enough density, the autoinducer or quorum signal molecules reach a certain threshold concentration; where they bind with cytoplasmic receptor proteins (LuxR in the Figure 4.1 example) which in turn recognize and bind a consensus binding sequence (*lux* box) upstream of the *luxICDABE* operon to activate its expression. The LuxR protein is very unstable in absence of AHL or LuxR-AHL complex. In addition, LuxI is also activated by the AHL-LuxR complex that acts as a positive feedback control loop to synthesize more QS molecules thus flooding the entire system with quorum signal.

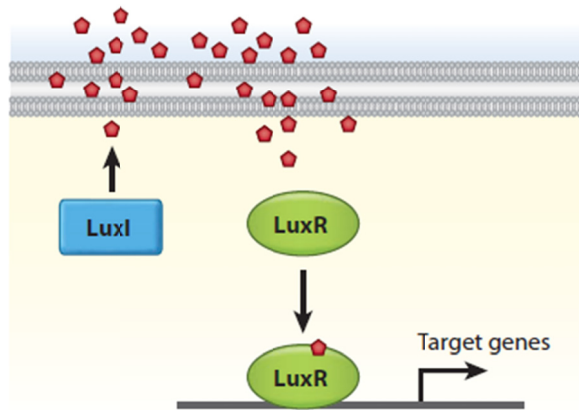


Figure 4.1: Schematic representation of a quorum sensing circuit of the Gram-negative bacteria (*Vibrio fischeri*).

Red pentagons represent autoinducer molecules or acyl homoserine lactones (AHL).
(Adapted from reference 1)

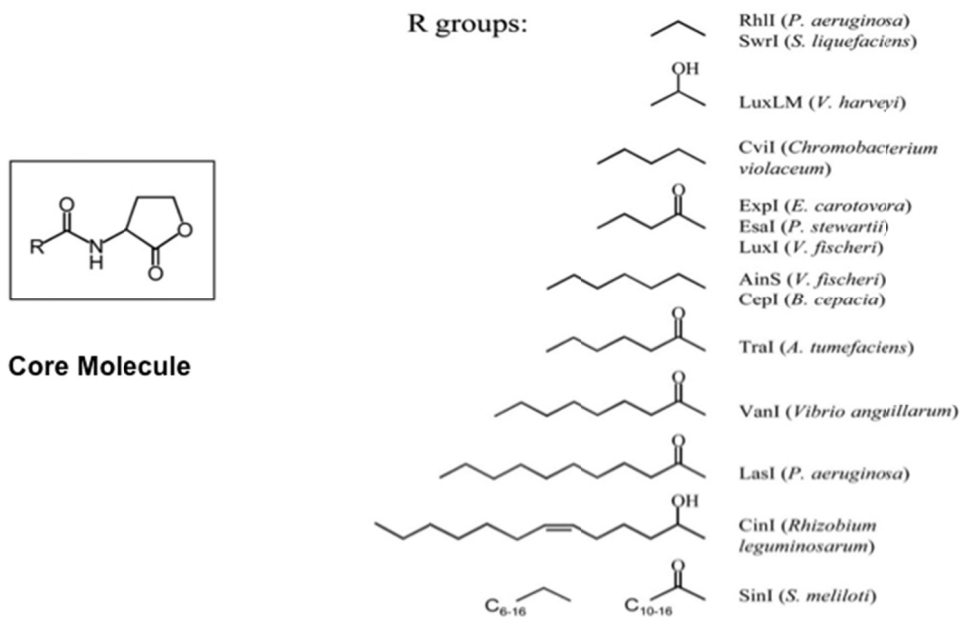


Figure 4.2: List of different autoinducers or quorum sensing (QS) molecules.

(Left) Core molecules for QS in Gram-negative bacteria. (Right) Side chain modifications of the core molecule used as QS signal molecules by different bacterial species. The acyl variation of an AHL molecule is unique to a particular bacterial species and function as private communication signals between its own species. (Adapted from reference 2)

Quorum Sensing (QS) Circuit for *P. aeruginosa*

The quorum sensing (QS) circuit for *P. aeruginosa* consists of two pairs of inducer/receptor units Las I/R and Rhl I/R. The detailed QS circuit diagram is shown in Figure 4.3 & 4.4. Quorum sensing molecules such as C₁₂-AHL and C₄-AHL are produced in the late exponential phase by LasI and RhlI. These AHL molecules then control the production of the Pseudomonas quinolone signal or PQS in the transition to the stationary growth phase (3). PQS upregulates the *phzA-G* genes to produce phenazine derivative compounds. One of these phenazine derivative compounds is pyocyanin (PYO) and is the molecule of interest in our study as it also plays a significant role in iron chelation as well as biofilm growth and morphology (4). Pyocyanin also is also hypothesized to act as an electron shuttling molecule from the oxygen deficient biofilm core to the exterior oxygen rich environment (5).

Biofilm Formation

We have so far discussed the basic mechanism of quorum sensing circuits for *P. aeruginosa*. Now we focus our discussion towards formation of structured multicellular communities or biofilms and how quorum signals play an important role in their formation. We will specifically discuss biofilm formation by the species used in our study, *P. aeruginosa*.

The schematic shown in Figure 4.5 demonstrate the basic steps involved in biofilm formation. Bacteria, when present in a low cell density (LCD) state, exist mostly as free-swimming planktonic organisms. At this stage, the first step of reversible attachment with the surface happens. As cell density increases collisions between bacteria and the surface increase and hence the probability that cells will adhere. At this stage, the second step of irreversible attachment happens. If favorable conditions exist, sufficient numbers of bacteria will adhere to the surface to form microcolonies (third step) (6,7).

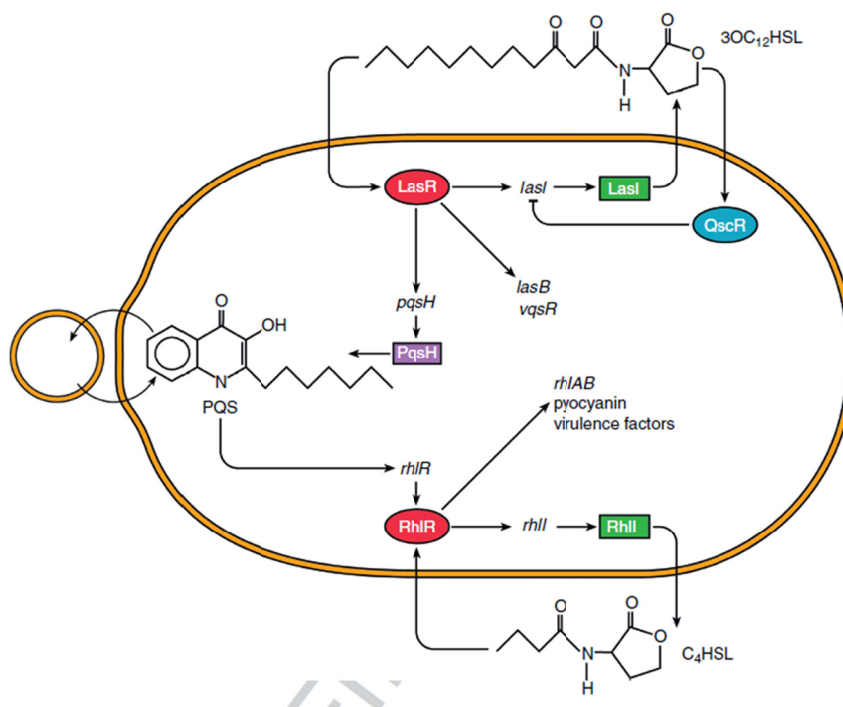


Figure 4.3: Quorum sensing circuit for *P. aeruginosa*. (Adapted from reference 3).

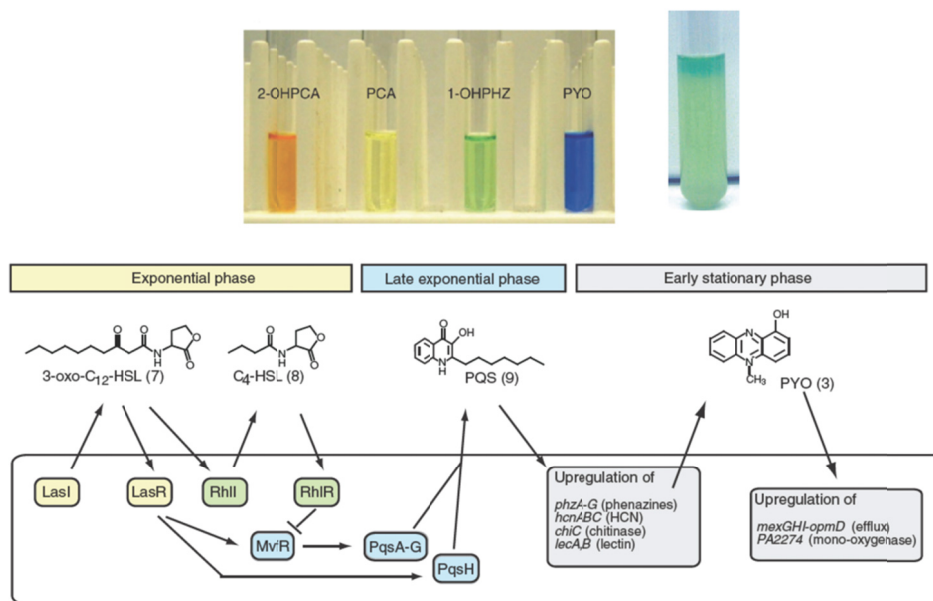


Figure 4.4: Colored phenazine compounds

(Top) The colored pigments of phenazine derivative compounds.(Bottom) Quorum sensing diagram for *P. aeruginosa*. HSL represents acyl homoserine lactones. (Adapted from reference 8)

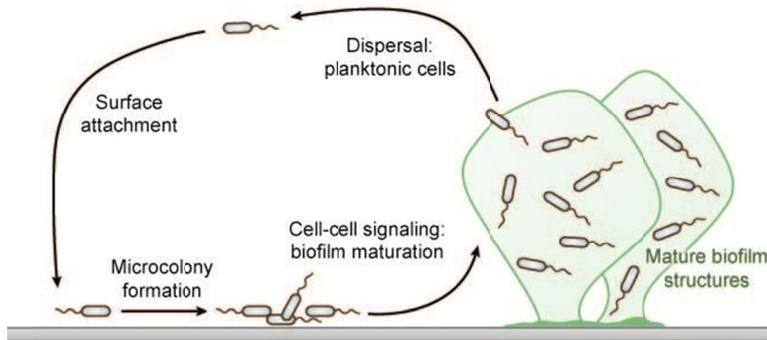


Figure 4.5: Schematic diagram of the different stages of *P. aeruginosa* biofilm formation.

(Adapted from reference 6)

As the bacterial micro-colony reaches high cell density, it activates the quorum-sensing pathway leading to the production of phenazine derivative compounds as well as the extracellular matrix (ECM). *P. aeruginosa* ECM is comprised of alginate, lectin and other carbohydrate polymers and helps establish one of the main components of the biofilms three-dimensional architecture. At the last stage of the biofilm development, biofilms reach a certain critical size and may enter programmed cell death or dispersion that will ultimately free some of the ECM liberating the bacteria at the core of the matrix to produce another micro-colony and eventually another three-dimensional bacterial colony. As previously mentioned, QS dependent signaling also induces the production of numerous phenazines. The detailed pathway of synthesis of such phenazine compounds from shikimic acid mediated by PCA has been shown in Figure 4.6. Figure 4.6 also shows the genes involved in phenazine synthesis from chorismate to PCA and onwards (8, 9, 10, 11). As previously mentioned, these phenazines may serve as extracellular redox carriers and may help provide cells inside of the biofilm with a mechanism to dump electrons via soluble phenazine electron carriers as electron donors become more limited at high cell density.

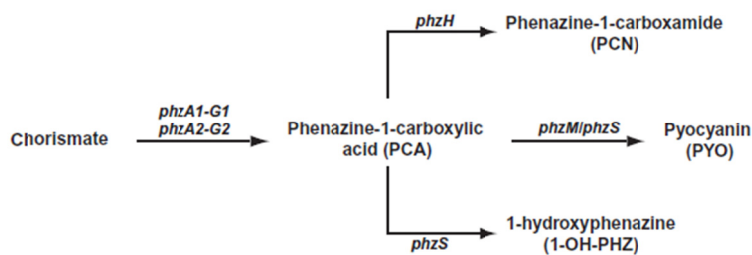
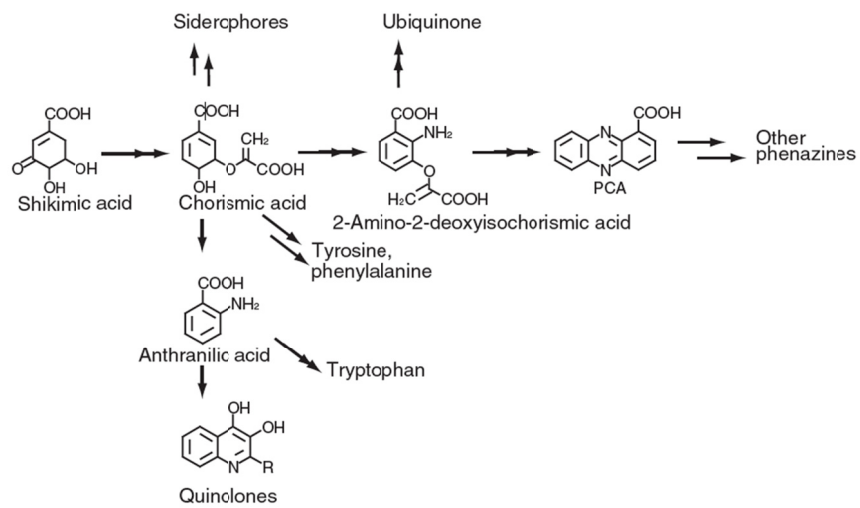


Figure 4.6: Phenazine synthesis pathway in *P. aeruginosa*

(*Top*) Schematic diagram of the phenazine synthesis pathway in *P. aeruginosa*. (*Bottom*) Phenazine production pathways from chorismate and the corresponding genes associated with them. (Adapted from reference 5 & 6)

Function of Phenazine compounds

Figure 4.7 shows various functions of the phenazine derivative compounds, which include pyocyanin. Particular attention has been given to the fact that several phenazines can generate reactive oxygen species (ROS). ROS generation can lend a powerful competitive advantage to bacteria in the environment (12). The *P. aeruginosa* produced phenazine pyocyanin has been studied as an antimicrobial compound for decades and is one of the primary pigments responsible for *P. aeruginosa*'s unique blue green color (Figure 4.4) upon isolation (13). Recent experiments have also demonstrated that phenazines can act as extracellular electron shuttles (5,8). These are hypothesized to either help dissipate electrons from bacteria when electron acceptors are limited (as may be the case in a dense biofilm environment) or to reduce and solublize certain metals *in situ* (14).

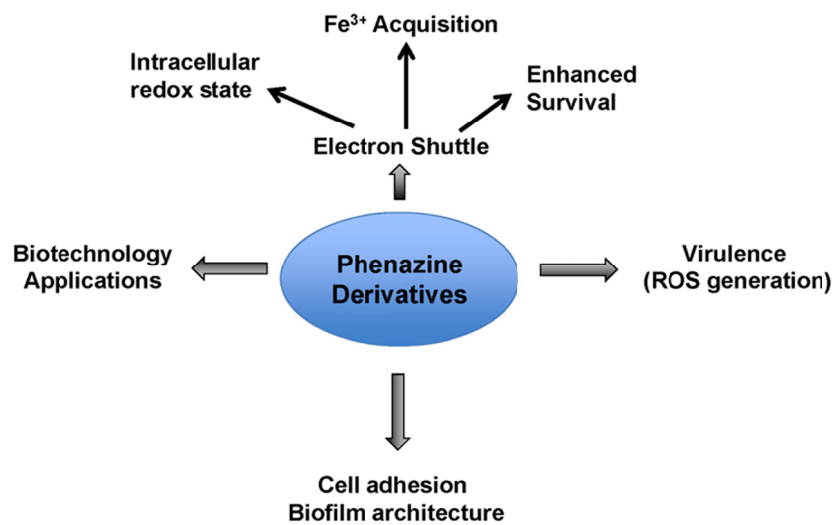


Figure 4.7: Schematic diagram of the different functions of phenazine compounds produced by bacteria.

Basic Electrochemistry of Phenazine Derivative Compounds

The structure and $E_{1/2}$ of commonly found phenazine derivative compounds is shown in Table 4.1. Pyocyanin (PYO) shows a two-electron reversible (Nernstian) behavior in the pH range of 5 to 8. The $E_{1/2}$ of the reaction is -0.04 V (vs. NHE) or -0.68 V (vs. Hg/Hg₂SO₄) at pH 7.0. It is probably an outer sphere reaction, since the $E_{1/2}$ position is independent of the type of electrode (Pt, Au, glassy carbon or mercury electrode) used.

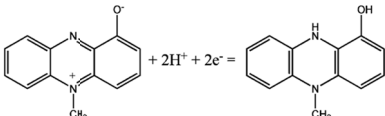
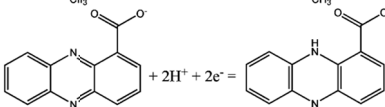
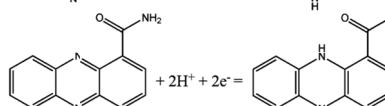
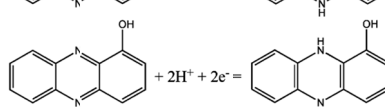
Chemical name (abbreviation)	Redox couple involving two-electron transfer	$E_{1/2}$ (vs. NHE) (mV)			
		pH 5	pH 6	pH 7	pH 8
pyocyanin (PYO)		69	8	-40 (-34) ^b	-103
phenazine-1-carboxylate (PCA)		12	-60	-116 (-177) ^c	-
phenazine-1-carboxamide (PCN)		-8	-81	-140 (-115) ^d	-
1-hydroxyphenazine (1-OHPHZ)		-57	-126	-174 (-172) ^e	-245

Table 4.1: List of electroactive phenazine derivative compounds and their respective half wave potential.

(Adapted from reference 15)

Bacterial iron acquisition

Iron is an essential nutrient for almost every bacterial species. In many environments, especially inside the body, iron is one of the limiting nutrients for invading bacteria. That is because *in vivo* free iron or Fe(II) is essentially nonexistent and is scavenged and stored in iron binding proteins such as transferrin (16). This is likely due to several reasons: ROS generated during aerobic respiration include hydrogen peroxide and the reaction of hydrogen peroxide with free, soluble ferrous iron yields the highly toxic hydroxyl radical and Fe(III). Thus, iron sequestration helps prevent generation of more potent ROS *in vivo*. Additionally the sequestration of iron makes it inherently difficult for bacteria to proliferate after gaining access to an infection site. Many pathogenesis studies have demonstrated that impairing bacteria in iron transport renders them far less virulent (17, 18, 19). As expected, bacteria have adapted and evolved many fascinating ways to obtain iron, including the predation of other bacterial species for iron and the liberation of iron from iron storage proteins such as transferrin (16, 20). In fact it has been demonstrated that pyocyanin can reduce iron, removing it from transferrin, allowing *P. aeruginosa* to grow in its presence (16).

P. aeruginosa has two primary ways to take up iron from the environment. First is siderophore (iron chelating compound) mediated iron uptake. Siderophore mediated uptake allows *P. aeruginosa* to scavenge insoluble Fe(III) from its environment. The two siderophores, pyochelin and pyoverdine are responsible for this energy intensive process and are taken up into the cell after excreted siderophores bind iron and come in contact with a specific receptor on the cell exterior (4). Second, *P. aeruginosa* possess genes analogous to the ferrous (*feo*) iron uptake system found in many other bacteria. The *feo* system allows for the transport of soluble Fe(II) across the bacterial inner membrane.

Motivation

A biofilm is a complex three-dimensional structure comprised of bacteria and other microorganisms which can be found anywhere from rocks to dental plaques to burn wound infections. Its unique nature of extremely high antibiotic resistance makes it important to study in a clinical setting. Besides being a model for biofilms and quorum sensing, *P. aeruginosa* poses an enormous threat to patients suffering from cystic fibrosis.

There is currently immense interest (21-24) in *Pseudomonas* biofilm studies especially regarding the impact that quorum signaling has on biofilm development. However, there is serious lack of quantitative study on biofilm metabolism and how metabolites are produced by a biofilm in real time. To understand how the cells communicate in their surrounding three-dimensional space it is important to detect and spatially monitor the metabolites quantitatively. Most present day biofilm studies are performed using confocal microscopy using green fluorescent protein or different bulk phase concentration measurements via HPLC or spectrophotometric methods. Most of these techniques are invasive and involve several steps of extraction, separation and measurement. There are very few techniques that will give real time quantitative information about metabolites produced from a biofilm.

In this study we have shown with the aid of scanning electrochemical microscopy (SECM) the real time quantitative detection of pyocyanin produced by a *P. aeruginosa* biofilm. Because pyocyanin is an electroactive compound it is possible to directly detect what redox state it exists in, spatially, in real time while it is produced by the biofilm. This gives us a unique opportunity to probe the local environment above the biofilm in real time, which helps in a biofilm behavioral study, since it is the *in situ* local concentration that matters most. Through this innovative technique we have shown that the pyocyanin produced by the biofilm exists predominately in a reduced state and forms a reduced layer above the biofilm of the order of 500 μm thick even in the presence of

oxygen. We have also demonstrated that under conditions where pyocyanin forms a substantial reducing layer there is large proportion iron in the form of Fe(II). We hypothesize that this Fe(II) enriched environment may be energetically favorable for the cell not only for transport but by the ability to solubilize Fe(III), which might be inaccessible to the organism.

4.2 MATERIALS & METHODS

Materials

All the chemicals were used as purchased without any further purification. Pyocyanin (catalog no. R9532) and potassium ferrocyanide were purchased from Sigma Aldrich. Falcon brand Petri dishes (catalog no 351008). 10 μ m Pt wire was purchased from Good fellow. Milli-Q-water, 18 M Ω deionized water, was used to prepare all solutions.

Preparation of Buffer

A 1/1 (v/v) mixture of MOPS and LB-broth was used as buffer in all the experiments. The pH of the buffer was adjusted to 7.2. MOPS buffer (25) contains 50 mM MOPS or 3-(N-morpholino)propanesulfonic acid), 93 mM NH₄Cl, 2 mM KH₂PO₄, 1 mM MgCl₂, 3.6 μ M Fe₂(SO₄)₃. LB-Broth buffer contains 5 g/L yeast extract, 10 g/L tryptone and 10 g/L NaCl. In select experiments cell supernatants were added. To generate supernatants, *P. aeruginosa* phzA2 mutant was inoculated into 3 mL of LB-MOPS medium and grown overnight. The culture was then diluted in fresh LB-MOPS to approximately 1x10⁹ cells per mL (A₆₀₀=1) and centrifuged in a 15 mL tube at 7000xg for 10 min at 25°C. Supernatants were decanted and stored at 4°C until used.

Bacteria Culture & Biofilm Sample Preparation

Unless indicated *P. aeruginosa* PA14 was used. The *phz* mutant was generated previously (26) and all other *P. aeruginosa* mutants were obtained from the PA14 nonredundant transposon library (27). Unless specified all planktonic cultures were grown at 37°C in Luria-Bertani (LB) broth, shaking at 250 RPM. PA14 strain was utilized for all *P. aeruginosa* experiments. When necessary, gentamicin was used at 50 µg/mL. For biofilm formation *P. aeruginosa* was grown planktonically overnight and resuspended to an A600 = 1. 5 µl of this suspension were added to the surface of a 25 mm polycarbonate membrane (Whatman #110606). Prior to inoculation, membranes were placed on a 100 mM Petri dish containing LB agar + 100 mM KNO₃. Membranes were then overlaid with a “stencil” made of Sylgard 184 PDMS (Dow Corning). PDMS stencils were fabricated by casting ~1.5 mL of PDMS into a 35 mm Petri dish with a 5 mm OD tube positioned flush with the center bottom of the well. Once polymerized the stencil was removed from the dish and the tubing was displaced leaving a 5 mm opening for biofilms to form. After inoculation, biofilms were allowed to form overnight at 37°C either aerobically or anaerobically in a Coy biofilm chamber with a 5% H₂, 10% CO₂, 85% N₂ atmosphere. Biofilms were then moved aerobically to room temperature where membranes were gently separated from the PDMS overlay. Films were transferred to the SECM apparatus mentioned in this section. Films were then overlaid with ~600 µL of LB-MOPS medium. LB-MOPS medium is a 1:1 ratio of LB medium and MOPS minimal medium with no added iron or carbon sources.

Measurement of pH and Pyocyanin Production by Planktonic Bacteria

1 mL of an overnight culture of *P. aeruginosa* was washed 2x in an equal volume of LB and the A600 determined. Washed cells were diluted into 50 mL of LB or LB-MOPS medium in a 250 mL Erlenmeyer flask and incubated at 37°C, shaking at

250 RPM. 1 mL was removed each hour for absorbance, pH and PYO measurements. Absorbance was measured at 600 nm to quantify cell growth. pH was determined by glass electrode pH meter and PYO concentration was determined by absorbency at 690 nm after chloroform extraction. Briefly, in a 1.5 mL polypropylene tube, 1 mL of medium was extracted by addition of 500 μ L chloroform and vortexed for 1 min. Samples were centrifuged for 5 min at 14,000xg and the organic phase was transferred to a 3 mL glass vial. Chloroform was removed by an N₂ stream until no visible solvent remained. The contents of the vial were resuspended in 250 μ L of MOPS buffer (pH=7) and concentration was determined using the molar extinction coefficient of PYO at 690 nm (4130 M⁻¹ cm⁻¹).

Detection of *phzA* Induction in a Colony Biofilm

phzA promoter fusions to GFP were a generous gift of the Aimee Wessel, modified from her previous study (28). These fusions were generated by replacement of the *rsaL* promoter region in vector pGJB5 with the *phzA1* promoter region creating pAW2, which was used here. *P. aeruginosa* containing the pAW2 were used to form 5 mm colony biofilms described in “Bacterial culture and biofilm preparation”. Biofilms were grown overnight anaerobically on LB agar +100 mM NO₃ to ensure that *phzA* and other phenazines would not be induced at the beginning of the assay. At t=0 plates were transferred to aerobic incubation at 37°C. At 1 h intervals a 10 μ L polypropylene micropipette tube was gently touched to an area of the biofilm and then used to aspirate 5 μ L of PBS buffer onto a microscope slide. Samples were covered with a #1 25x25 mm coverslip and visualized for epifluorescence microscopy at 1000x magnification on a Nikon 50i microscope with a 100x 1.4NA PLAN APO lens, Nikon DS-2MBW digital camera and Nikon NiS-Elements D v3.0 software. All images were taken with a gain of

1.0 and a 100 ms exposure time. The brightest 4 cells in each field of view were used as representatives in the figure.

Determination of Fe(II) in Presence of Pyocyanin (PYO)

Fe(II) measurements were performed as described by reference 29. Briefly, ferrozine solution was added to samples, incubated for 5 min at 25°C allowing ferrozine to complex with Fe(II) and read for absorbance at 562 nm. After reading, the solution was acidified and reduced by addition of 1.4 M hydroxylamine in 2 M HCl to convert any Fe(III) to Fe(II) which complexed with ferrozine. Solutions were neutralized by the addition of ammonium acetate and read again at 562 nm. Initial readings were divided by final readings to determine the percentage Fe(II) present in each sample.

Electrochemical Measurements

All the electrochemical measurements were acquired using scanning electrochemical microscopy (SECM) (CHI 920C, CH Instruments, Austin, Texas, USA). A 10 μm diameter Pt disk electrode was used as the SECM tip. Details about SECM tip fabrication can be found elsewhere (30). 0.5 mm Tungsten wire and Hg/Hg₂SO₄ (Radiometer, Copenhagen) was used as counter and reference electrode respectively. All the potentials henceforth mentioned here were referred vs. Hg/Hg₂SO₄/K₂SO₄(sat) (+0.64V vs. NHE).

Calibration Curve for Pyocyanin (PYO)

A biofilm was prepared as described in “Bacteria Culture & Biofilm Sample Preparation” section. After growing the *Δphz* mutant biofilm on a polycarbonate membrane in an anaerobic environment, it was carefully transferred on a 35 mm Petri

dish (Falcon, catalog no. 351008). A PDMS stencil was carefully placed over the membrane, as shown in Figure 4.8. 500 μL of buffer was then added to fill up the 1 cm diameter stencil chamber. The working (10 μm Pt), reference and counter electrodes were setup as shown in Figure 4.8 (*bottom*).

Aliquots of 1 mM PYO were then added to 500 μL of buffer to make 6, 10, 20, 50, 70 and 100 μM PYO solutions. Square wave voltammetry (SWV) was recorded at each PYO concentration in triplicate with a 10 μm tip located in bulk solution. The parameters for SWV were as follows: Initial potential: -0.35V, Final potential: -0.85V, Increment Potential: 0.004V, Amplitude: 0.025V, Frequency: 5Hz.

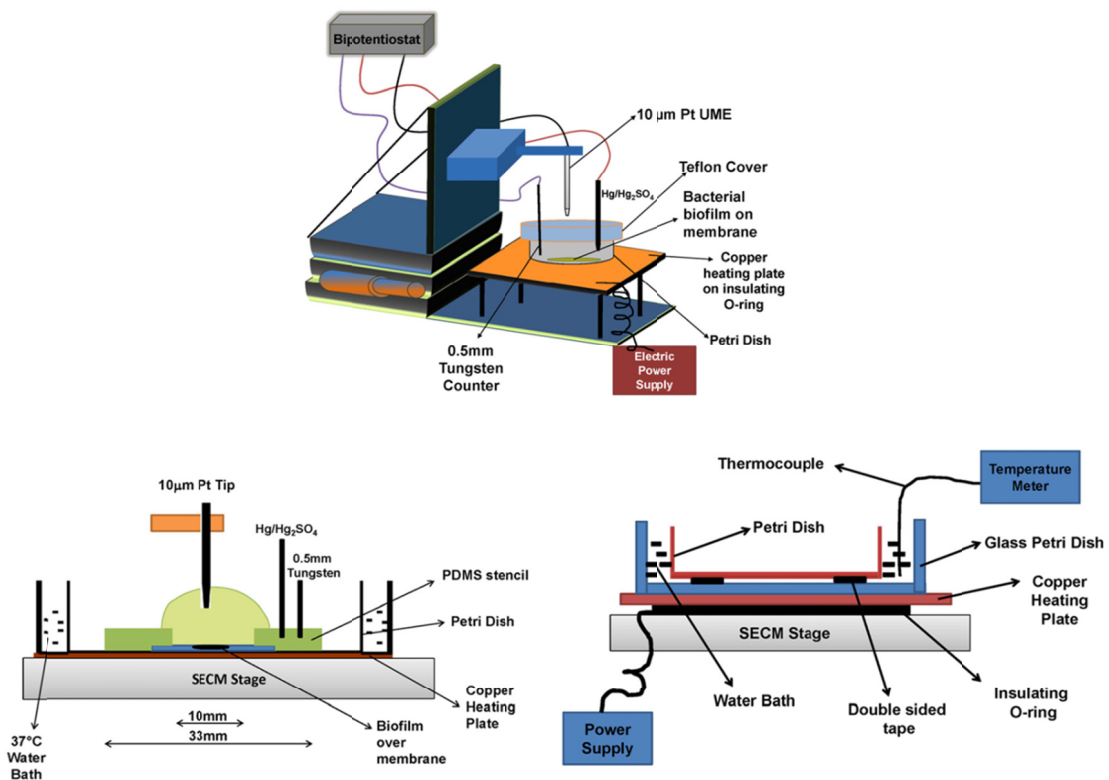


Figure 4.8: Schematics of SECM experimental setup

(Top) Schematics of SECM experimental setup for biofilm experiment. (Bottom) Detail close-up experimental setup for biofilm experiment.

Real Time Quantitative Detection of Pyocyanin (PYO) using SECM

The 5 mm wild type *P. aeruginosa* biofilm was setup on an SECM stage as described in the previous section. The biofilm was gently washed twice with 500 μL of buffer (1/1 MOPS-LB mixture). Tip-substrate (biofilm) distance, d , was then fixed at 20 μm with the aid of a negative feedback approach curve using 1mM ferrocyanide as a redox mediator. The solution was then replaced by 500 μL of fresh buffer solution. Cells were additionally washed with buffer twice to remove any ferrocyanide in the solution. Finally, 600 μL of supernatant was added to the chamber and background current using SWV was measured by SECM tip periodically. Once the background current was stabilized, the temperature of the water bath was increased to 36°C using the copper heating plate connected to a Variac power supply. The temperature was constantly monitored by a thermocouple dipped inside the water bath located outside the Petri dish. The time was set to zero when the temperature reached 36°C. 200 μL of buffer was added to the chamber after 1h 30 min to compensate for water loss due to evaporation. SWV was recorded at every 10 min until 5hr in the potential range of -0.35 to -0.85 V.

Mapping of Reduced / Oxidized Pyocyanin (PYO) Layer above Biofilm using SECM:

The biofilm was assembled on the SECM stage and an approach curve was performed to fix the tip-substrate distance as described in previous sections. Once the background was recorded, 125 μL of 1 mM PYO was added to 500 μL of buffer to make a 200 μM PYO solution. The biofilm was then incubated in the same solution for 30 min at 25°C. The tip was biased at -0.3V (oxidizing reduced PYO at tip) and then moved in the z-direction towards the biofilm from 2000 μm away at the speed of 0.1 μm / 0.02 s or 5 μm / s. Similarly, the tip was biased at -0.8V (reducing oxidized PYO at tip) to map the z-direction oxidized PYO profile above the biofilm.

Electrochemical Imaging of a Biofilm using SECM

A 1 mm *P. aeruginosa* biofilm was used for electrochemical imaging using SECM. The biofilm was grown and assembled on the SECM stage as described in previous sections. The SECM stage tilt was fixed by performing a negative feedback approach curve using ferrocyanide as a redox mediator. PYO was then added to 500 μ L buffer to prepare a 200 μ M PYO solution. A feedback mode SECM image of a wild type biofilm was acquired at 25°C by biasing the tip at -0.3V. The tip-substrate (biofilm) distance was kept constant at 20 μ m (approx.). Scanning speed was maintained at 8 μ m / 0.02 s.

4.3 RESULTS

Pyocyanin (PYO) Production by Planktonic Bacteria

To predict minimum incubation durations for our biofilm experiments we first determined the incubation time necessary for pyocyanin production in our media by planktonic cells. Additionally, pH measurements were needed to determine what pH shifts we would expect during the duration of our measurements. Data for PYO concentration alongwith bacteria growth curve is given in Figure 4.9A. A PYO concentration of about 10 μ M was detected at 4 h. A corresponding pH shift from 7.0 to 7.8 was also observed in Figure 4.9B over 9h.

Activation of QS Controlled Genes in a *P. aeruginosa* Colony Biofilm:

To demonstrate that QS controlled gene activation was occurring in our colony biofilm we utilized a *phzA* promoter – GFP fusion reporter construct which has been used previously to demonstrate the onset of QS dependent behavior (28). As Figure 4.10 shows, *phzA* promoter activity was observed in colony biofilms after transfer to fresh growth medium at 5-6 h period.

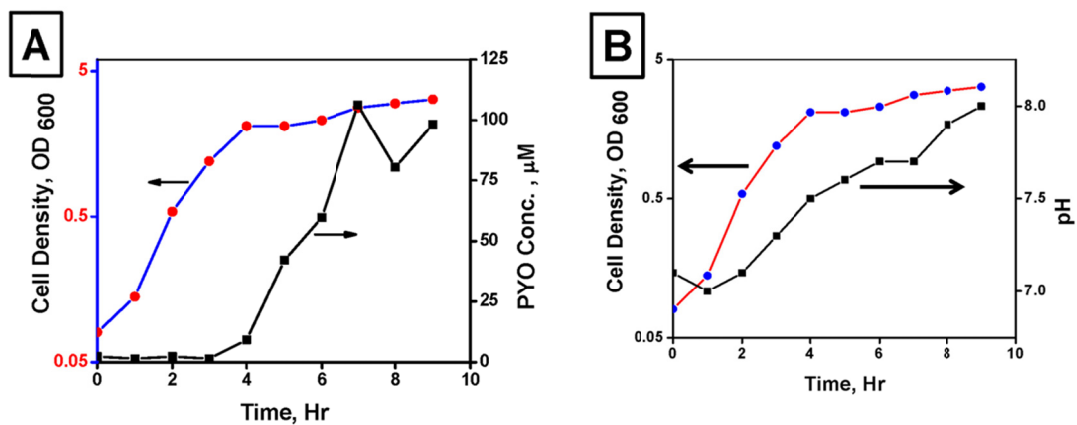


Figure 4.9: Bulk phase PYO and pH measurement in presence of planktonic bacteria

(A) PYO concentration and (B) pH changes with cell density over time (h). The y-axis in both figures for cell growth curve is plotted in logarithmic scale.

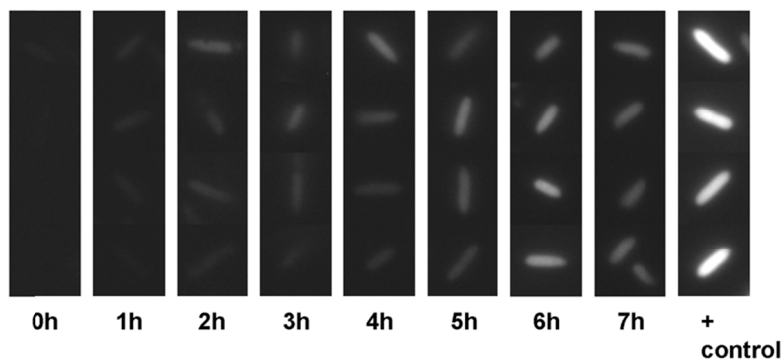


Figure 4.10: Activation of QS in *P. aeruginosa* biofilm (5 mm).

The brighter image represents QS activation. The cells were incubated in 1/1 MOPS-LB buffer at 37°C. Images were taken in 1000x magnification.

Calibration Curve for Pyocyanin (PYO)

Square wave voltammograms (SWV) at different concentrations (6 to 100 μM) of added PYO in supernatant buffer are shown in Figure 4.11 A. Figure 4.11 B shows a calibration curve for PYO in the range of 6-100 μM in supernatant buffer solution in presence of *Δphz* mutant biofilm. The calibration curves (Figure 4.11 C & D) show a linear relationship in the range of 6-200 μM PYO in presence of 1/1 MOPS-LB buffer in presence of *Δphz* mutant biofilm. The equation for figure B, C and D is $y=mx+c$ where, y represents SWV peak height (pA) and x corresponds to PYO concentration (μM) in their corresponding buffer. The calibration curve equations used are as follows:

Biofilm in supernatant buffer solution Y in Ampere and X in μM :

$$Y = (1.06\text{e-}12 * X) - 2.08\text{e-}12$$

Biofilm in 50/50 MOPS-LB buffer (low concentration range, 6-30 μM):

$$Y = (1.46\text{e-}12 * X) - 3.14\text{e-}12$$

Biofilm in 50/50 MOPS-LB buffer (high concentration range, 30-200 μM):

$$Y = (0.91\text{e-}12 * X) + 5.63\text{e-}12$$

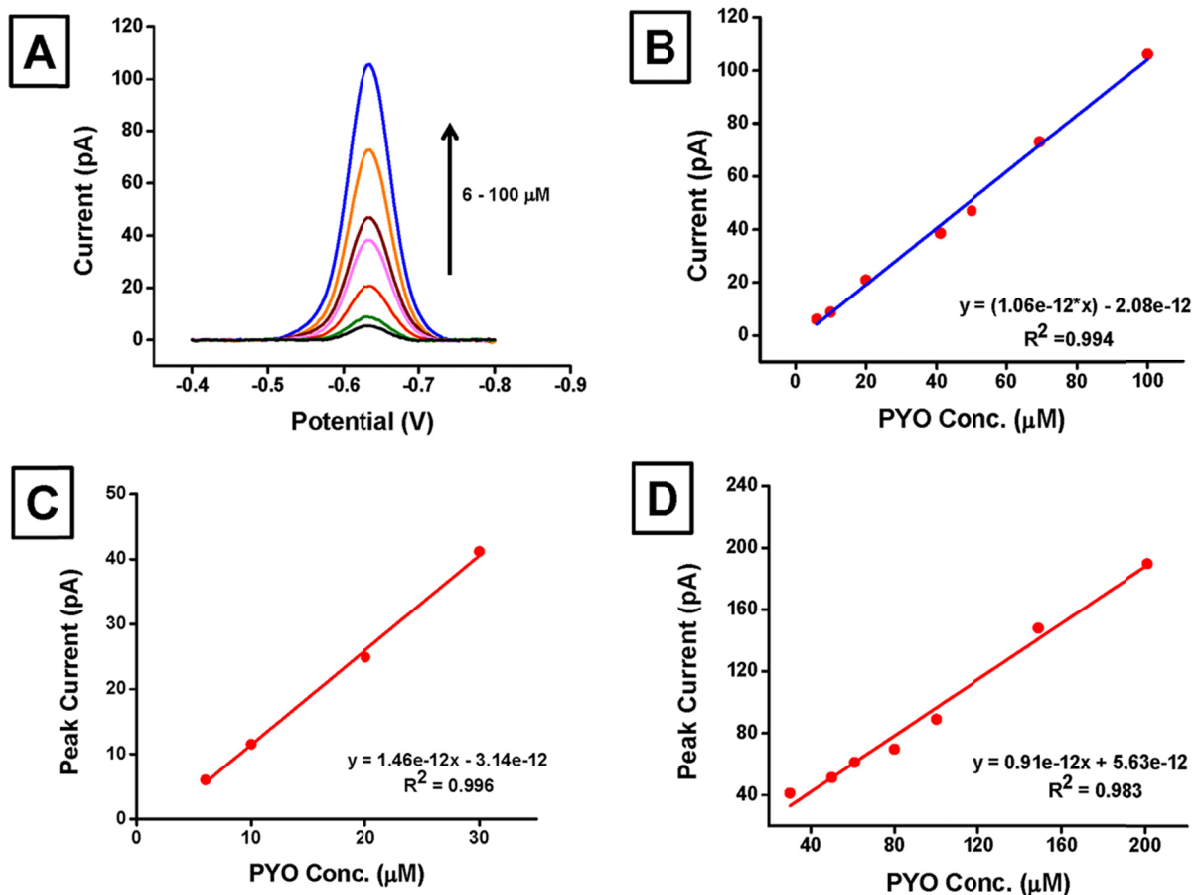


Figure 4.11: Calibration curve of PYO (6 – 200 μM range)

(A) & (B) Square wave voltammogram (SWV) and calibration curve at different concentration (6 to 100 μM) of PYO in the presence of supernatant buffer solution. (C) Calibration curve at varying concentrations of PYO in the range of 6-30 μM in 50/50 MOPS-LB buffer solution. (D) Calibration curve at varying concentrations of PYO in the range of 30 - 200 μM in 1/1 MOPS-LB buffer solution. Working electrode: 10 μm Pt. Reference electrode: $\text{Hg}/\text{Hg}_2\text{SO}_4$.

Real Time Quantitative Detection of Pyocyanin (PYO)

Figure 4.12 shows the real time quantitative detection of PYO produced from a *P. aeruginosa* 5 mm colony biofilm surface. Detectable amounts of PYO ($\sim 1 \mu\text{M}$) were produced at 90 min. The local PYO concentration (or 20 μm away from the biofilm surface) produced by the biofilm was $2.5 \mu\text{M}$ after 6 h. Figure 4.12 A shows gradual development of a characteristic PYO peak at -0.63V . The peak height was converted to PYO concentration by the calibration curve (Figure 4.11B). The time delay for the production of PYO was due to time required for accumulation of quorum signal to activate the quorum sensing circuit. Once PYO production was triggered it increased very rapidly. Similar PYO production patterns were noticed for *P. aeruginosa* grown planktonically in a shaken incubator at 37°C (Figure 4.9A).

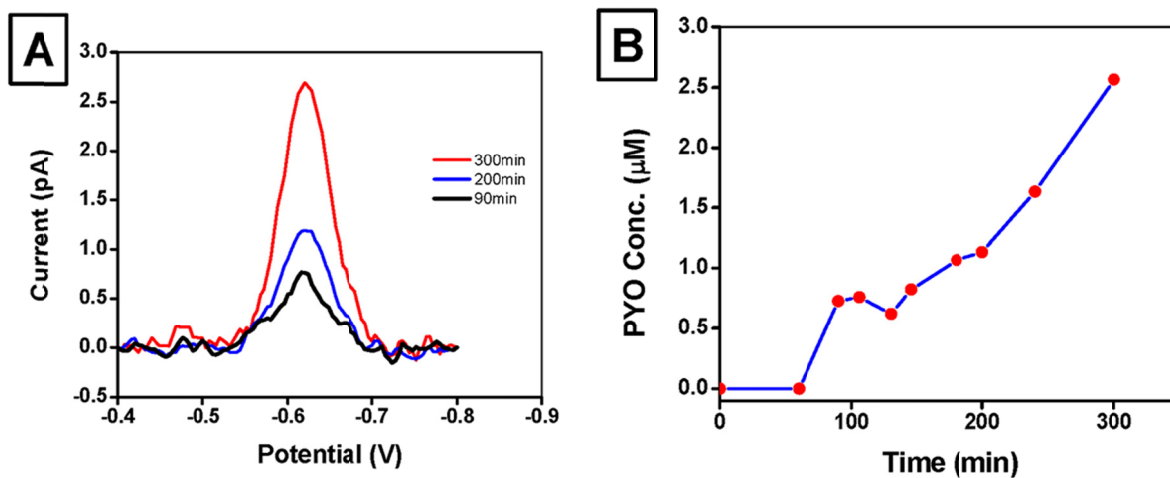


Figure 4.12: Real time quantitative detection of PYO produced from *P. aeruginosa* biofilm

(A) Square wave voltammogram (SWV) of PYO produced by *P. aeruginosa* biofilm in presence of supernatant buffer at 36°C. (B) Plot of PYO concentration (μM) w.r.t. time (min). Tip-substrate (biofilm) distance was 20 μm .

Spatial Mapping of Reduced/Oxidized Pyocyanin (PYO) above Biofilm

During measurements of PYO production from colony biofilms we noticed that PYO proximal to the biofilm was in a completely reduced state. To study this phenomenon, Z-direction spatial mapping of the reduced and oxidized PYO ratio above the wild type *P. aeruginosa* biofilm at 36°C was measured and shown in Figure 4.13 A. The tip was biased at -0.3V (oxidizing at tip) and -0.8V (reducing at tip) while moving towards the biofilm to map the reduced and oxidized PYO respectively. Zero on the x-axis represents the surface of the biofilm. The height of the reduced PYO layer was observed to be ~400 μm whereas the amount of reduced PYO was 9 μM at 60 μm away.

To alleviate the problems of variability of amount of PYO produced by the biofilm, 200 μM of oxidized PYO was added above the *Aphz* mutant biofilm (unable to produce PYO) to study the reduced layer behavior at different conditions. Figure 4.14 shows the z-direction spatial distribution of reduced PYO above the *Aphz* mutant biofilm in the presence of 200 μM PYO at 25°C and 36°C respectively. The height of reduced PYO layer has also been recorded to be 500 μm and 600 μm at 25°C and 36°C, respectively (Figure 4.14). The profile at 25°C (Figure 4.14) shows no reduced PYO at 1500 μm whereas almost 50% of the added oxidized PYO has been reduced at a distance of ~60 μm from biofilm. However, a ~5 times higher reduced PYO concentration was observed at 37°C at 100 μm from biofilm surface. Cyclic voltammograms (Figure 4.14) at 37°C also showed that all of the PYO is in reduced form at a distance of 100 μm ; whereas PYO exists 100% in the oxidized form 1500 μm from the biofilm. In both reduced PYO profiles, a drop in PYO concentration is observed as the tip approaches 60 μm or closer above the biofilm. When the tip is 2000 μm away from the biofilm, the tip is operating in generation –collection mode but when the tip is within the reduced PYO layer zone, it switches to feedback mode. When the tip moves even closer to the biofilm, i.e. 60 μm or less, the tip starts sensing the substrate or biofilm. As a result the response at the tip at ≤ 60 μm distance depends on how fast the oxidized PYO at the tip is being

reduced by the biofilm. In this case the kinetics of electron transfer from the biofilm is not fast enough to keep up with the rate of oxidation of reduced PYO at the tip, hence the current drops at $\leq 60 \mu\text{m}$. The z-direction oxidized PYO profile (Figure 4.15 A& B) complements the reduced profile. As observed before in Figure 4.14 that there is no oxidized PYO at $500 \mu\text{m}$ or less, the oxidized PYO layer resembles the enhanced negative feedback mode approach curve.

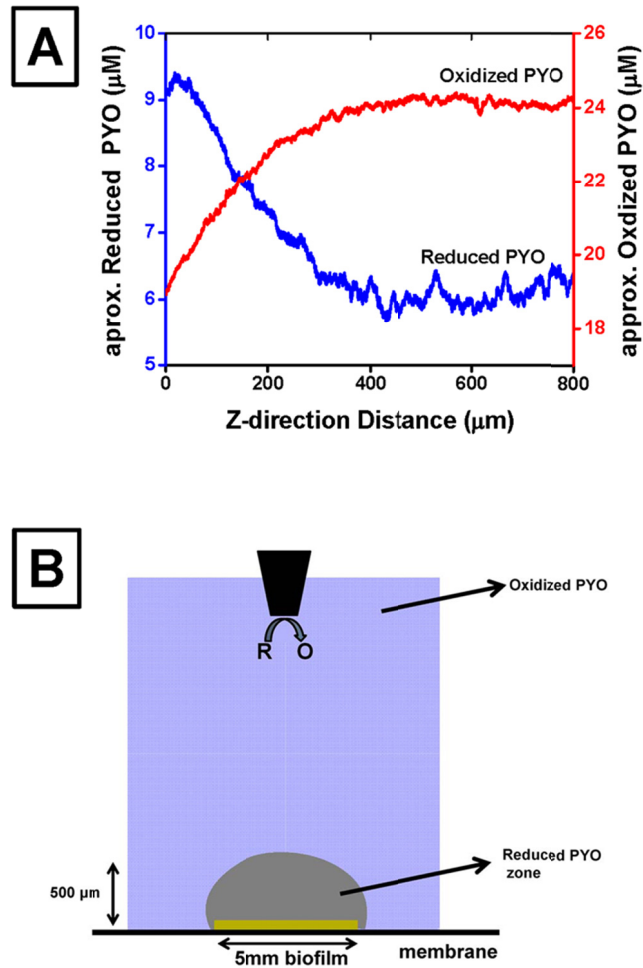


Figure 4.13: Z-direction naturally produced PYO profile above *P. aeruginosa* biofilm

(A) Z-direction profile of reduced and oxidized PYO profile produced by *P. aeruginosa* wild type biofilm. Zero on the x-axis represents the surface of biofilm. (B) Schematic model of the reduced PYO layer above the biofilm. To spatially map the reduced and oxidized PYO profile, the tip was biased at -0.3V (oxidizing potential) and -0.8 V (reducing potential), respectively.

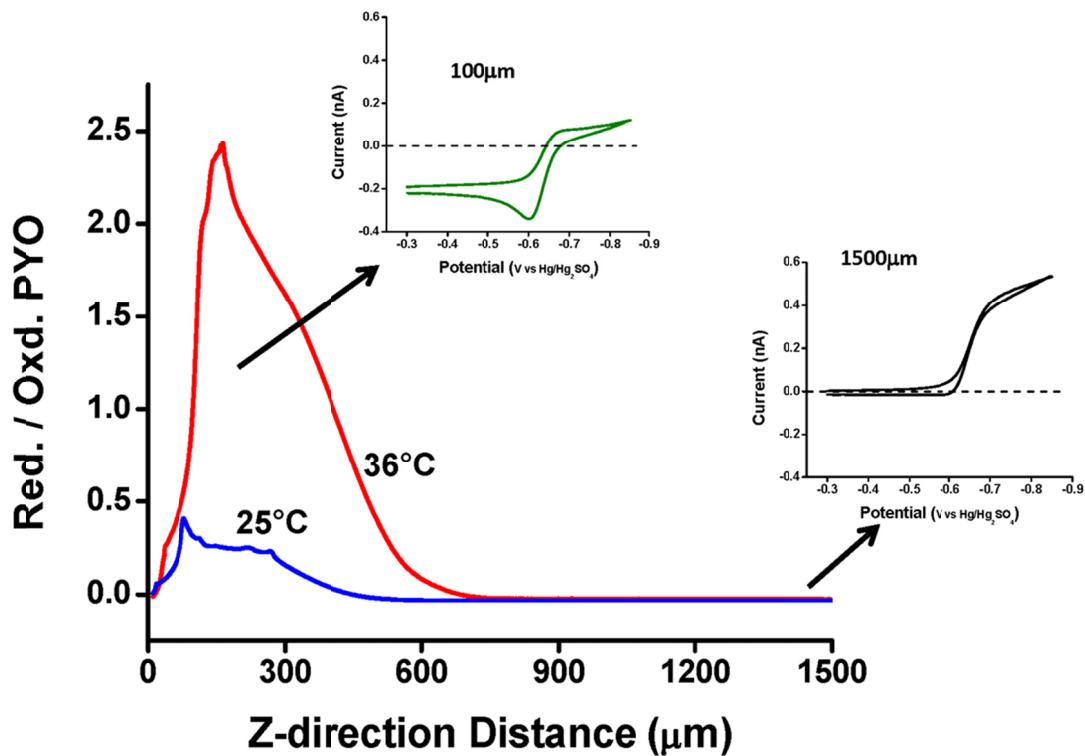


Figure 4.14: Z-direction PYO profile above Δphz biofilm at 25°C and 36°C

Z-direction reduced PYO profile above a Δphz biofilm at 25°C (blue line) and 36°C (red line). Cyclic voltammograms were taken at 1500 μm (black) and at 100 μm (green) at 36°C. The y-axis is normalized by 200 μM of added oxidized PYO.

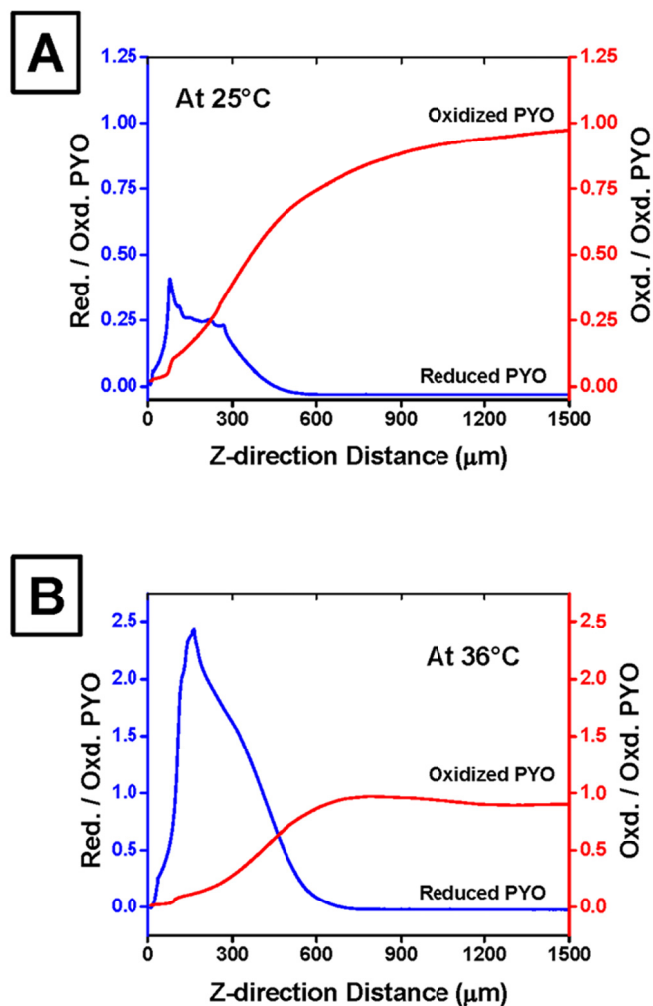


Figure 4.15: Comparison of Z-direction oxidized and reduced PYO profile above Δphz biofilm at 25°C and 36°C

Z-direction reduced (blue line) and oxidized (red) PYO profile above a Δphz mutant biofilm at (A) 25°C and (B) 36°C, respectively. Both y-axes are normalized by 200 μM of oxidized PYO added to the solution.

Determining the Mechanism of PYO Reduced Layer Development

We hypothesized that the PYO reduced layer development was caused by a flow of electrons from the biofilm by carbon source oxidation and that this flow could be diverted from PYO to NO_3^- instead. To predict the behavior of the reduced PYO layer above the *Δphz* mutant biofilm we added excess Fe(III) (100 μM , ten time more than usual) to facilitate the reoxidation of PYO or NO_3^- (100 mM) (Figure 4.16A) both in the presence of 200 μM PYO. The reduced PYO layer collapsed in the presence of excess NO_3^- (100 mM) whereas the layer height decreased by 100 μm in the presence of excess (100 μM) Fe(III) in the buffer. However the absolute value of the ratio of reduced/oxidized PYO remained the same. The oxidized PYO layer (Figure 4.16B) again showed a complimentary z-direction profile. For a *Δphz* mutant standard sample, the z-directional oxidized PYO profile confirmed the enhanced negative feedback or consumption of oxidized PYO above the biofilm. For an excess of NO_3^- sample the oxidized PYO layer showed similar behavior to that of a negative feedback approach curve confirming the absence of reduced PYO layer.

Figure 4.17 shows a model to explain the effect of electron flow inside the cells on a reduced PYO layer above the biofilm. The reduced PYO layer was 500 μm for both the *Δphz* mutant and the wild type *P. aeruginosa* biofilm, whereas the ratio of reduced/oxidized layer almost doubled for a *napA* mutant biofilm. This is hypothetically due to electron flow being diverted to PYO reduction instead of reduction of possible trace NO_3^- concentrations present in LB-MOPS (31). For the cytochrome *bc1* mutant biofilm the reduced PYO layer was reported to be almost zero in comparison to the standard sample (*Δphz* mutant) and is explained by the fact that cytochrome bc1 was reported to be the site at which PYO accepts electrons from *P. aeruginosa* (32). Heat killed dead control cells showed no reduced PYO layer above the biofilm (Figure 4.16A).

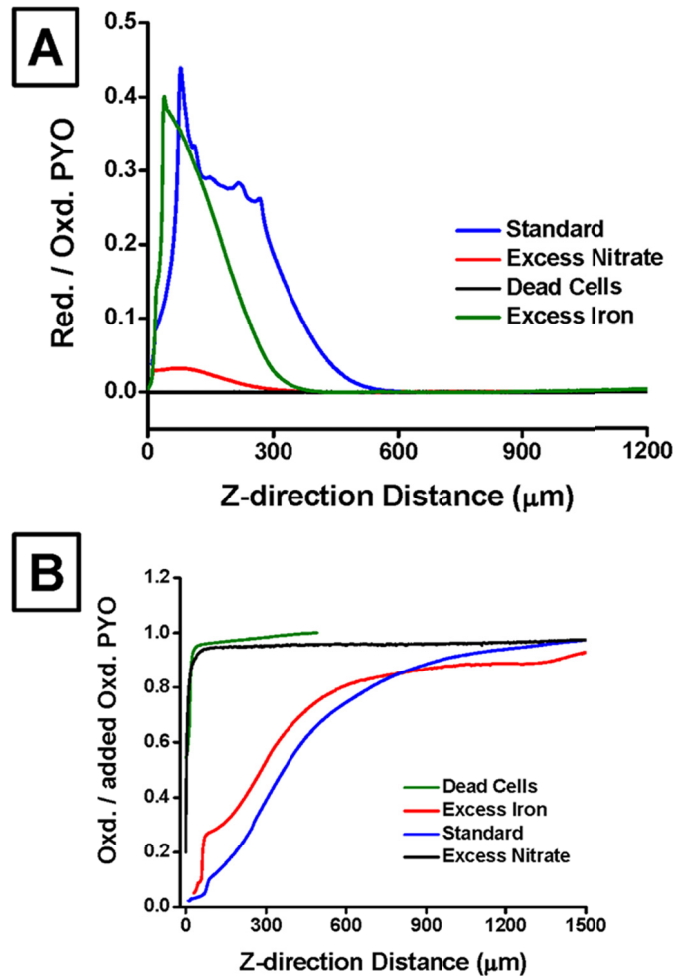


Figure 4.16: Z-direction oxidized and reduced PYO profile above *Aphz* biofilm in presence of excess iron or nitrate

(A) Z-direction reduced PYO profile above mutant *Aphz* biofilm. PYO was oxidizing at the tip while the tip approached the biofilm. (B) Z-direction oxidized PYO profile above the same set of biofilms. PYO was reducing at the tip in this experimental setup. In each experiment 200 μM of oxidized PYO was added at 25°C. Both reduced and oxidized PYO concentration in y-axis is normalized by 200 μM of oxidized PYO.

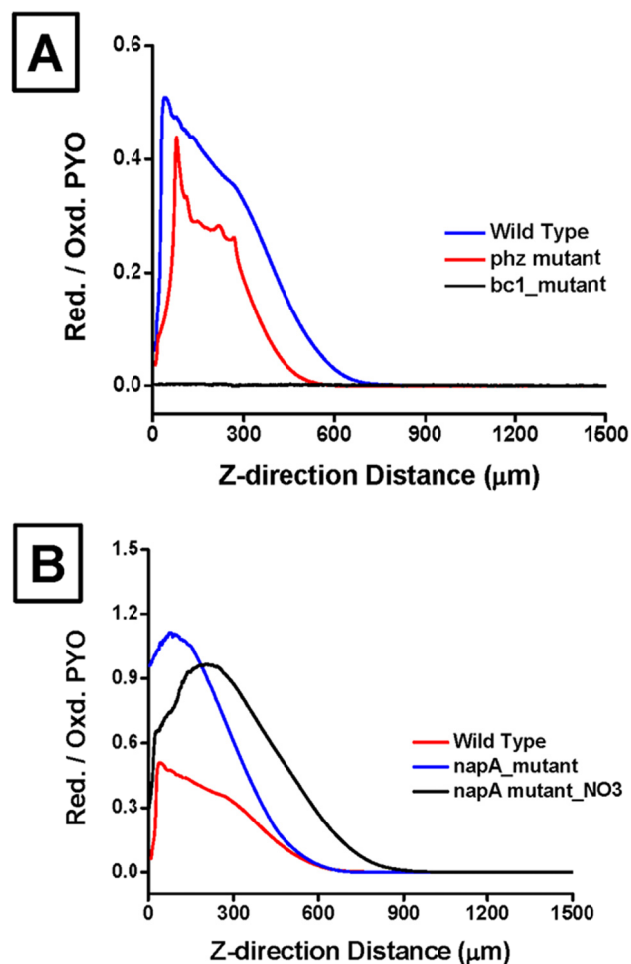


Figure 4.17: Z-direction oxidized and reduced PYO profile above different mutant of *P. aeruginosa* biofilm

(A) & (B) Z-direction profile of reduced PYO above biofilms of different mutant of *P. aeruginosa*. The tip was held at -0.3V or at oxidizing potential of reduced PYO. In each experiment 200 μM of oxidized PYO was added at 25°C. Both reduced and oxidized PYO concentration in y-axis is normalized by 200 μM of oxidized PYO.

Reduction of Iron (III) in the Presence of Pyocyanin (PYO)

We hypothesized that a reduced PYO layer may enrich the local environment around a biofilm with Fe(II) by PYO-mediated reduction of Fe(III) even in the presence of oxygen. As demonstrated in Figure 4.16, the addition of excess Fe(III) modulated the reduced PYO layer height. Using a Ferrozine based Fe(II) assay we measured total Fe(II) percentages from media exposed to colony biofilms for 1h. These data are presented in Figure 4.18. The data supports our model that reduced PYO layer produced by the *Δphz* biofilm indeed reduce the Fe(III) present in the solution. Henceforth, addition of NO₃⁻ or the inactivation of cytochrome bc1 leads to a lower Fe(II) percentage due to collapse of reduced PYO layer above the biofilm (Figure 4.16 & 4.17). We also observed that the inhibition of either NO₃ reduction pathway (*napA* or *narG* dependent) led to an increase in Fe(II) percentage. However, *napA* mutant data showed more variability in Fe(III) reduction.

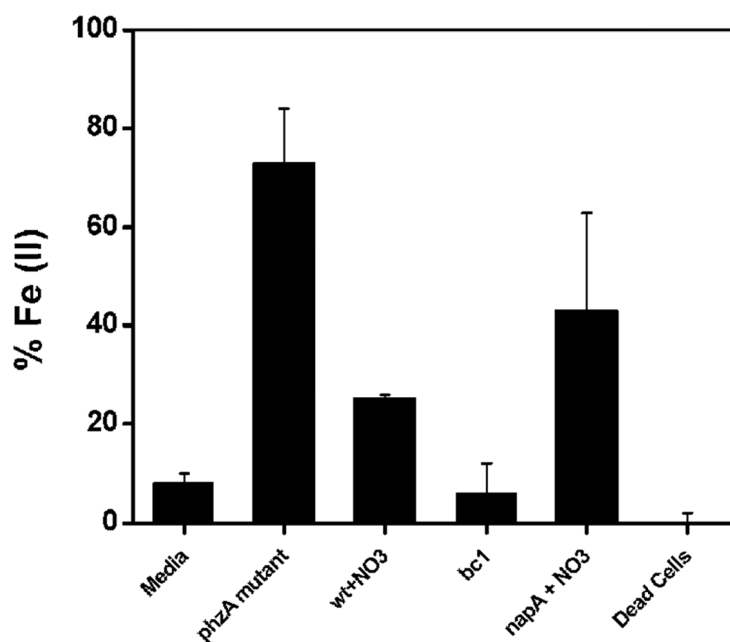


Figure 4.18: Percentage of Fe(II) in the presence of PYO treated biofilms for 1h.

250 μ L of buffer was used in each experiment in standard 5 mm colony biofilms. Media used was LB-MOPS buffer with or without 100 mM NO_3^- . All the experiments were performed at 25°C.

Electrochemical Imaging of a Biofilm

Figure 4.19 shows a constant height-mode SECM image of a 1 mm diameter *P. aeruginosa* biofilm. The image (Figure 4.19 C) was taken in the presence of 200 μM exogenous PYO. The tip was held at -0.3 V (PYO oxidizing potential) while scanning over the biofilm at a distance of 60 μm from the polycarbonate membrane maintaining a constant speed of 8 μm / 0.02 s (Figure 4.19 A). The false color contrast of the electrochemical image shows reactivity mapping of the biofilm for reducing oxidized PYO locally made by the tip just above the cells. The oxidized PYO diffused in the gap (tip-biofilm) where it is bacterially reduced resulting in higher current (purple color) recorded by the tip as shown in (Figure 4.19 C). Thus the image can be seen as mapping of electron shuttling from the biofilm to PYO in real time. Since there is no reduced PYO (as shown in Figure 4.19 C) away from the biofilm the current is almost zero (red color). The over-lapped 40x optical image of the biofilm was added for convenience to compare the topographical image with the electrochemical one (Figure 4.19 D). Figure 4.19 B shows the x-direction scan over a 1 mm biofilm at 25°C and 36°C respectively. The fraction of reduced PYO at 37°C is almost five times higher than that observed at 25°C. This may be due to higher rate of electron transfer from biofilm to PYO in solution as observed in Figure 4.14.

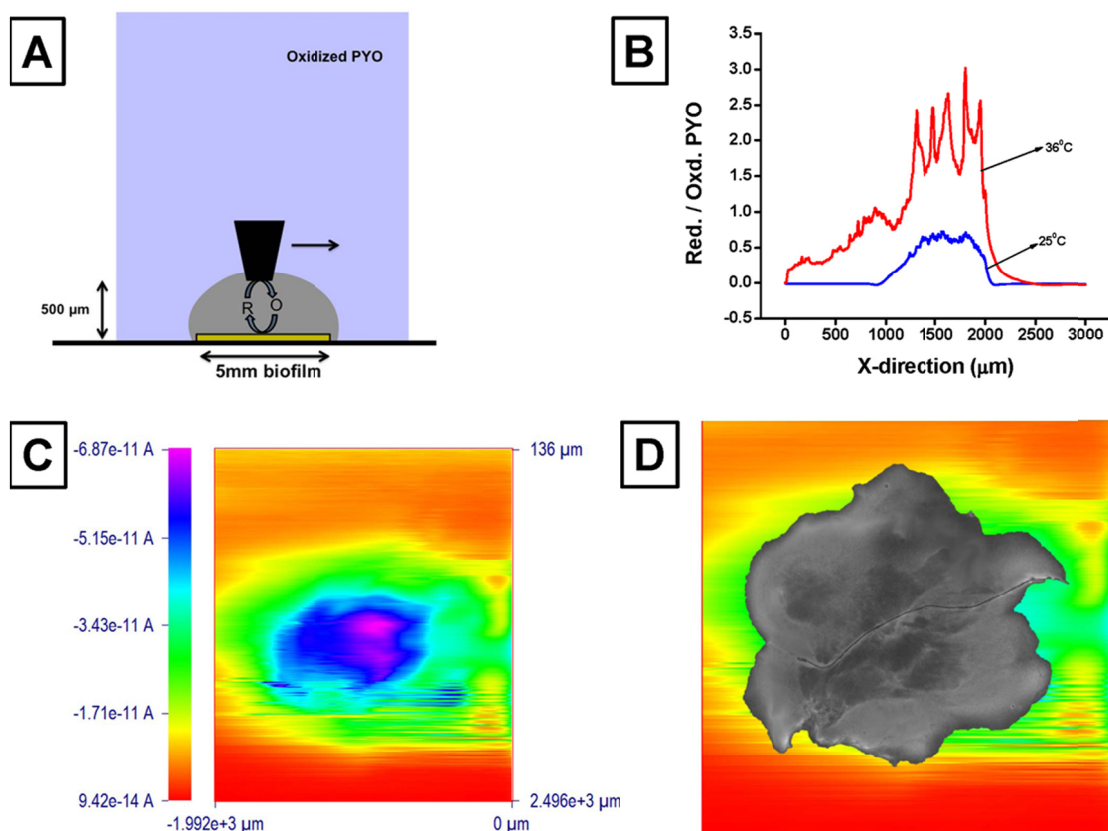


Figure 4.19: SECM image of 1 mm wild type *P. aeruginosa* biofilm

(A) Schematic diagram of experimental setup for x-scan and SECM imaging (B) X-direction scan over 1 mm biofilm at a distance of 30 μm (C) Constant height SECM image of a 1 mm wild type *P. aeruginosa* biofilm. Blue and purple color represents the mapping of electron transport from biofilm to reduce PYO in the solution above it. Tip was held at -0.3V to oxidize PYO. (D) Superimposed optical and SECM image of 1 mm biofilm. Tip used: 10 μm Pt. Tip-substrate (biofilm) distance: 20-30 μm. Solution used: 200 μM oxidized PYO in 1/1 MOPS-LB buffer solution.

4.4 DISCUSSION

Pyocyanin (PYO) is a blue-pigmented phenazine compound produced by *P. aeruginosa* under quorum sensing (QS) controlled regulation during late stages of growth when oxygen is present. PYO is a redox active molecule that has been shown to act as a virulence factor and antimicrobial for *P. aeruginosa* via reactive oxygen species (ROS) generation (34-36). Additionally, PYO and other phenazines have also been hypothesized to act as soluble electron carriers which can shuttle electrons from cells that may be electron donor limited; for example, those in the interior of a biofilm (5, 8, 14) which *P. aeruginosa* is renowned for forming. However, the local redox state of PYO produced from a *P. aeruginosa* biofilm is unknown. To characterize this local redox state of PYO produced from a bacterial biofilm, we utilized scanning electrochemical microscopy (SECM). The SECM electrochemical probe or ultramicroelectrode (UME), not only allowed us to determine the concentration of PYO as it was produced (Figure 4.12), but also to identify the local redox state of PYO in three dimensional space surrounding the biofilm in real-time; properties unable to be measured by other technologies. Z-direction mapping determined that a significantly reduced PYO layer extends over 500 μm from the biofilm surface (Figures 4.13 and 4.15).

To explain the reduced PYO layer phenomenon we propose intracellular and extracellular models, which work in unison as shown in Figure 4.20 respectively. Figure 4.20A shows electron flow from carbon source oxidation to extracellular oxygen via NAD^+/NADH , the ubiquinone pool and cytochrome bc1. However, when excess NO_3^- (100 mM) is present in the extracellular environment, electron flow is diverted from ubiquinone to reduce NO_3^- to NO_2^- through the NapA nitrate reductase (Figure 4.20A). Also, when PYO is present electron flow is diverted from cytochrome bc1 to PYO instead of oxygen reduction (Figure 4.20A). Hence, we hypothesized that reduced PYO layer formation would be diminished by obstructing the electron flow either through

cytochrome bc1 or by diverting electrons from the ubiquinone pool to the NapA nitrate reductase (Figure 4.16 and 4.17). In both cases we demonstrate that the diversion of electron flow to PYO, either by the mutation of cytochrome bc1 or the addition of excess NO_3^- lead to a decrease in reduced layer formation (Figure 4.16 and 4.17). In addition, we also observe increased reduced PYO layer formation for a *napA* mutant even in presence of NO_3^- . This increase may be due to additional electron flow to cytochrome bc1 as a result of electron flow divergence from the nonfunctional Nap complex.

Modulation of the reduced PYO layer also depends on extracellular conditions as shown in Figure 4.20B. According to this model, the amount of reduced/oxidized PYO solely depends on k_f or the rate of heterogeneous electron transfer from the biofilm to the outside solution; whereas the height of a reduced PYO layer above a biofilm depends on the kinetic balance of k_1 , k_2 and k_3 (see diagram for details). To maintain a reduced layer, the kinetics of electron transfer from the biofilm to PYO (k_f), must be greater than the kinetics of electron transfer from PYO to oxygen (k_1) and Fe(III) (k_2 and k_3). Reduced PYO reacts more readily with molecular oxygen than Fe(III) (15) as a result, oxygen concentration proximal (~500 -700 μm) to the biofilm decreases due to respiration as well as PYO-dependent oxygen reduction. This has been demonstrated by PYO cyclic voltammogram (CV) data at 100 and 1500 μm above the biofilm (Figure 4.14). Despite the presence of oxygen, PYO can also reduce Fe(III) to Fe(II) at pH 7 (15). We hypothesized that the addition of Fe(III) to the solution might play a role in modulating the reduced PYO layer by affecting k_2 . Figure 4.16 confirms our hypothesis showing that a decrease in height of the reduced layer is observed upon increasing the Fe(III) concentration in the solution. Figure 4.18 reveals that reduced PYO layer formation correlates with an increase in soluble Fe(II) production. Thus, reduced PYO layer formation may assist *P. aeruginosa* in scavenging insoluble Fe(III) from its

surrounding environment. Such Fe(III) reducing capabilities have been observed for PYO (15) and other *P. aeruginosa* phenazine compounds such as PCA (33).

Oxidized PYO exists beyond the reduced layer (1 to 2 mm) and can be reduced by other organisms to generate reactive oxygen species (ROS), which aid in *P. aeruginosa* virulence (34-36). However, a paradox in PYO and other QS controlled “virulence factors” such as quinolones is that they are made by *P. aeruginosa* even in the absence of a host or bacterial competitors. We propose that a major function for PYO (in addition to ROS generation or electron shuttling) may be to scavenge Fe near the biofilm environment by reduction of Fe(III) to Fe(II) via a reduced PYO layer extending a significant distance (500-700 μm) from the *P. aeruginosa* biofilm. This new proposed role for PYO serves to increase the concentration of Fe(II) around a biofilm providing *P. aeruginosa* with a way to obtain soluble Fe(II) instead of more energy intensive siderophore based Fe(III) transport mechanisms.

Reduced PYO layer formation above a biofilm can only be observed by spatial mapping of the PYO redox state. The measurement of a PYO layer several hundred microns thick, existing under several millimeters of solution is currently only achievable by the use of SECM. The unique capability of SECM, to allow us to know the position of the electrochemical probe (UME) over a biofilm surface, provides a way to quantitatively detect a three-dimensional layer of redox molecules in real-time. This opens a new opportunity of quantitative metabolite measurement by understanding the local distribution of redox metabolites in three-dimensional space and how they might help bacterial growth and survival.

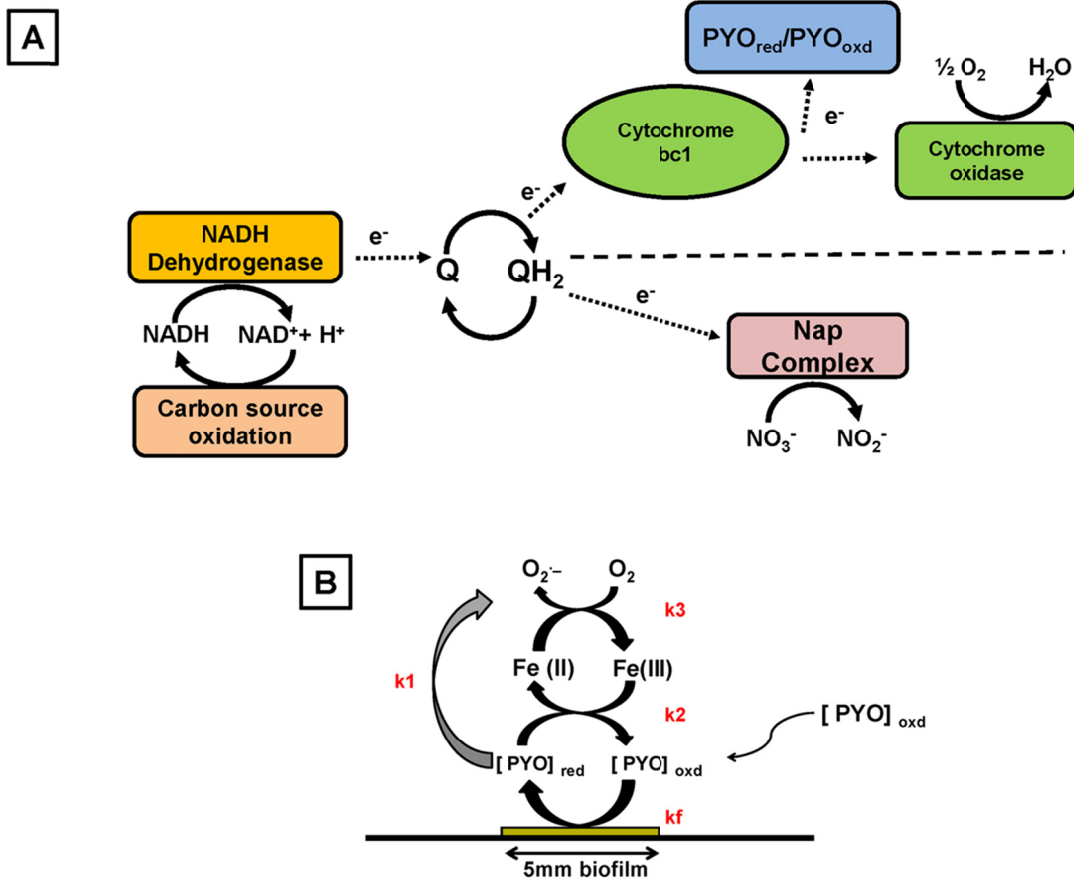


Figure 4.20: Proposed model of reduced PYO layer formation

(A) Proposed model of reduced PYO layer above biofilm. (B) Proposed schematic diagram of the electron flow from glucose oxidation to ubiquinone pool to PYO solution present in the extracellular environment.

4.5 CONCLUSION

In studying the biofilm production of PYO by SECM we have made several discoveries including the ability to detect pyocyanin (PYO) concentrations as low as 3 μM by a novel application of square wave voltammetry (SWV). We have also demonstrated that PYO is reduced locally by a biofilm even in the presence of oxygen and that cells are able to maintain a 500 μm reduced PYO layer above the biofilm. We have also discovered a mechanism that demonstrates a way that a *P. aeruginosa* biofilm can reduce iron over significant distances. This mechanism is reminiscent of recent findings by Newman et al (33) describing the ability of the phenazine PCA to reduce iron for *P. aeruginosa* utilization. We describe a mechanism in which *P. aeruginosa* can expand or contract a volume of an iron reducing substrate dependent upon the iron concentration in the biofilms vicinity which functions to increase the concentration of soluble iron even in the presence of oxygen.

4.6. ACKNOWLEDGEMENT:

This project was conducted in collaboration with Marvin Whiteley laboratory. The bacteria sample was prepared by Matthew M. Ramsey and all the electrochemical data were collected by Dipankar Koley. The Fe(II) determination assay, growth curve and GFP related experiments were performed by M. Ramsey. A. J. Bard and D. Koley acknowledge financial support from National Science Foundation (CH 0808927).

4.7 REFERENCES

- ¹ Miller MB, Bassler BL (2001) Quorum sensing in bacteria. *Annual review of microbiology* 55:165-99.
- ² (a)Taga, M. E., & Bassler, B. L. (2003) Chemical communication among bacteria. *Proc. Natl. Acad. Sci. U.S.A.* 14549-54.

- (b) Nealson KH, Platt T, Hastings JW (1970) Cellular control of the synthesis and activity of the bacterial luminescent system. *J Bacteriol* 104:313-22. (1st paper about quorum sensing in 1970, dealt with light producing bacteria that live inside Squid, 1st time it was characterized but the signal itself was not purified.)
- (c) Pearson JP, Passador L, Iglewski BH, Greenberg EP (1995) A second N-acylhomoserine lactone signal produced by *Pseudomonas aeruginosa*. *Proc. Natl. Acad. Sci. U.S.A.* 92:1490-4. (1st paper describing the likelihood of multiple types of QS functioning in *P aeruginosa*)
- (d) Passador L, Cook JM, Gambello MJ, Rust L, Iglewski BH (1993) Expression of *Pseudomonas aeruginosa* virulence genes requires cell-to-cell communication. *Science (New York, N.Y.)* 260:1127-30. (1st characterization of a QS signal in *P aeruginosa*)
- (e) Eberhard A et al. (1981) Structural identification of autoinducer of *Photobacterium fischeri* luciferase. *Biochemistry* 20:2444-9. (Purification and structural characterization of the first AHL quorum signal)
- ³ Schaechter, M. (2009) *Encyclopedia of microbiology*. Amsterdam ; Boston, Elsevier/Academic Press.
- ⁴ Banin, E., M. L. Vasil, et al. (2005) Iron and *Pseudomonas aeruginosa* biofilm formation. *Proc. Natl. Acad. Sci. U.S.A.* 102(31): 11076-81.
- ⁵ Price-Whelan, A., L. E. Dietrich, et al. (2007) Pyocyanin alters redox homeostasis and carbon flux through central metabolic pathways in *Pseudomonas aeruginosa* PA14. *J Bacteriol* 189(17): 6372-81.
- ⁶ West, S. a, Diggle, S. P., Buckling, A., Gardner, A., & Griffin, A. S. (2007) The Social Lives of Microbes. *Annu. Rev. Ecol. Evol. Syst.* 38(1), 53-77.
- ⁷ Ma L et al. (2009) Assembly and development of the *Pseudomonas aeruginosa* biofilm matrix. *PLoS pathogens* 5:e1000354.
- ⁸ Price-Whelan A, Dietrich LEP, Newman DK (2006) Rethinking “secondary” metabolism: physiological roles for phenazine antibiotics. *Nat. Chem. Biol.* 2:71-8.

- ⁹ Dietrich LEP, Price-Whelan A, Petersen A, Whiteley M, Newman DK (2006) The phenazine pyocyanin is a terminal signalling factor in the quorum sensing network of *Pseudomonas aeruginosa*. *Mol. Microbiol.* 61:1308-21.
- ¹⁰ Pierson LS, Pierson EA (2010) Metabolism and function of phenazines in bacteria: impacts on the behavior of bacteria in the environment and biotechnological processes. *Applied microbiology and biotechnology* 86:1659-70.
- ¹¹ Mentel M et al. (2009) Of two make one: the biosynthesis of phenazines. *Chembiochem : a European journal of chemical biology* 10:2295-304.
- ¹² Hassan, H. M. and I. Fridovich (1980) Mechanism of the antibiotic action pyocyanine. *J Bacteriol* 141(1): 156-63.
- ¹³ Fordos, M.-J. (1860) Recherches sur la matiere colorante des suppurations bleues: pyocyanine." *Comptes rendus hebdomadaires des séances del'Académie des sciences* 51: 215-217.
- ¹⁴ Newman, D. K. and R. Kolter (2000) A role for excreted quinones in extracellular electron transfer. *Nature* 405(6782): 94-7.
- ¹⁵ Yun Wang and Dianne K. Newman (2008) Redox Reactions of Phenazine Antibiotics with Ferric (Hydr)oxides and Molecular Oxygen. *Environ. Sci. Technol.* 42 (7), 2380-2386.
- ¹⁶ Cox, C. D. (1986) Role of pyocyanin in the acquisition of iron from transferrin. *Infect Immun* 52(1): 263-70.
- ¹⁷ Sokol, P. A. and D. E. Woods (1984) Relationship of iron and extracellular virulence factors to *Pseudomonas aeruginosa* lung infections. *J Med Microbiol* 18(1): 125-33.
- ¹⁸ Bearden, S. W. and R. D. Perry (1999) The Yfe system of *Yersinia pestis* transports iron and manganese and is required for full virulence of plague. *Mol Microbiol* 32(2): 403-14.

- ¹⁹ Velayudhan, J., N. J. Hughes, et al. (2000) Iron acquisition and virulence in *Helicobacter pylori*: a major role for FeoB, a high-affinity ferrous iron transporter. *Mol Microbiol* 37(2): 274-86.
- ²⁰ Mashburn, L. M., A. M. Jett, et al. (2005) *Staphylococcus aureus* serves as an iron source for *Pseudomonas aeruginosa* during in vivo coculture. *J Bacteriol* 187(2): 554-66.
- ²¹ Huse H, Whiteley M (2011) 4-Quinolones: Smart Phones of the Microbial World. *Chem. Rev.* 111:152-9.
- ²² Hense B a et al. (2007) Does efficiency sensing unify diffusion and quorum sensing? *Nat. Rev. Microbiol.* 5:230-9.
- ²³ Bukelman O et al. (2009) Electrochemical analysis of quorum sensing inhibition. *Chem. Commun. (Cambridge, England)*:2836-8.
- ²⁴ Waters CM, Bassler BL (2005) Quorum sensing: cell-to-cell communication in bacteria. *Annual review of cell and developmental biology* 21:319-46.
- ²⁵ Whiteley, M., M. G. Banger, et al. (2001) Gene expression in *Pseudomonas aeruginosa* biofilms. *Nature* 413(6858): 860-4.
- ²⁶ Dietrich, L. E., A. Price-Whelan, et al. (2006) The phenazine pyocyanin is a terminal signalling factor in the quorum sensing network of *Pseudomonas aeruginosa*. *Mol Microbiol* 61(5): 1308-21.
- ²⁷ Liberati, N. T., J. M. Urbach, et al. (2006). An ordered, nonredundant library of *Pseudomonas aeruginosa* strain PA14 transposon insertion mutants. *Proc. Natl. Acad. Sci. U.S.A.* 103(8): 2833-8.
- ²⁸ Connell, J. L., A. K. Wessel, et al. (2010) Probing prokaryotic social behaviors with bacterial "lobster traps". *MBio* 1(4).
- ²⁹ Viollier, E., P. W. Inglett, et al. (2000) The ferrozine method revisited: Fe(II)/Fe(III) determination in natural waters. *Appl. Geochem.* 15(6): 785-790.

- ³⁰ Bard AJ, Mirkin MV, Eds. (2001) *Scanning Electrochemical Microscopy* (Merrel Dekker, New York).
- ³¹ Palmer, K. L., S. A. Brown, et al. (2007) Membrane-bound nitrate reductase is required for anaerobic growth in cystic fibrosis sputum. *J Bacteriol* 189(12): 4449-55.
- ³² Price-Whelan, A. (2009) Physiology and mechanisms of pyocyanin reduction in *Pseudomonas aeruginosa*. Biology. Pasadena, CA, California Institute of Technology. Ph.D.
- ³³ Wang, Y., J. C. Wilks, et al. (2011) Phenazine-1-carboxylic acid promotes bacterial biofilm development via ferrous iron acquisition. *J Bacteriol* 193(14): 3606-3617
- ³⁴ Hassan HM & Fridovich I (1980) Mechanism of the antibiotic action pyocyanine. *J Bacteriol* 141(1):156-163.
- ³⁵ Britigan BE, et al. (1992) Interaction of the *Pseudomonas aeruginosa* secretory products pyocyanin and pyochelin generates hydroxyl radical and causes synergistic damage to endothelial cells. Implications for *Pseudomonas*-associated tissue injury. *J Clin Invest* 90(6):2187-2196.
- ³⁶ Ran H, Hassett DJ, & Lau GW (2003) Human targets of *Pseudomonas aeruginosa* pyocyanin. *Proc Natl Acad Sci U S A* 100(24):14315-14320.

CHAPTER 5: Real-time Mapping of a Hydrogen Peroxide Concentration Profile Across a Polymicrobial Biofilm Using SECM

ABSTRACT

Quantitative detection of hydrogen peroxide in solution above a *Streptococcus gordonii* (*Sg*) bacterial biofilm was studied in real time by scanning electrochemical microscopy (SECM). The concentration of hydrogen peroxide was determined to be 0.7 mM to 1.6 mM in the presence of 10 mM glucose over a period of 2 to 8 h. The hydrogen peroxide production measured was higher near the biofilm surface in comparison to *Sg* grown planktonically. Differential hydrogen peroxide production was observed both by fluorometric as well as by SECM measurements. The interaction between two different species in a bacterial biofilm of *Sg* and *Aggregatibacter actinomycetemcomitans* (*Aa*) in terms of hydrogen peroxide production was also studied by SECM. One-directional y-scan SECM measurements showed the unique spatial mapping of hydrogen peroxide concentration across a mixed species biofilm and revealed that hydrogen peroxide concentration varies greatly dependent upon local species composition.

5.1 INTRODUCTION

Streptococcus gordonii (*Sg*) is a member of the viridans group streptococci-Gram-positive oral microbes that are known to ferment sugars into lactic acid and produce hydrogen peroxide in the presence of oxygen (1). The presence of these beneficial oral streptococci has been shown to improve oral health, by either competition with pathogens for nutrients in the oral cavity or by the production of inhibitory concentrations of hydrogen peroxide. Populations of viridans group streptococci negatively correlate with the presence of many notable oral pathogens (2, 3). However, recent work has demonstrated that in vitro *Sg* can grow in coculture with the opportunistic oral pathogen *Aggregatibacter actinomycetemcomitans* (*Aa*) (4). In co-culture *Aa* preferentially utilizes *Sg*-produced lactic acid (5) and detoxifies *Sg*-produced hydrogen peroxide using the KatA enzyme (6). Recent work has demonstrated that hydrogen peroxide induces katA expression as well as apiA, which encodes an immunoprotective factor that renders *Aa* more resistant to killing by host innate immunity (5). These studies demonstrated induction of gene expression in mixed species biofilms by *Sg*-produced hydrogen peroxide. Because hydrogen peroxide is rapidly degraded by catalase and can also react with other biological materials, we sought to quantify local hydrogen peroxide concentrations in real time to be utilized for future polymicrobial experiments between *Sg*, *Aa*, and other oral bacteria.

Previous measurements of hydrogen peroxide have been performed using fluorescence, spectroscopy and other methods (1, 7–10). However, current techniques lack the ability to quantify local hydrogen peroxide concentrations at the surface of a biofilm. In this study, scanning electrochemical microscopy (SECM) was used to address this problem. SECM has the unique ability to set the exact distance from a sensing tip (an ultramicroelectrode (UME) of size ~10 to 25 μm diameter) to a substrate through a feedback approach curve (11) (tip current, i_T , vs. distance above substrate, d) and thus is able to measure the local concentration over a biofilm. Several studies concerned with the

electrochemical measurement of hydrogen peroxide concentration have been reported (12–17), but none dealt with spatial mapping adjacent to a biofilm surface. In addition, SECM has the ability to scan over a substrate in the x-y direction and thus is able to record a unique spatial concentration profile over the surface. SECM has been used before in biological systems (18–24) to measure the local concentration over soft biological samples and for imaging. SECM is thus a new analytical tool to study not only the local hydrogen peroxide concentration in a bacterial biofilm but also to map the hydrogen peroxide concentration spatially across two different species of bacteria located distally in a biofilm. This allows the determination of the actual hydrogen concentration produced by *Sg* and the quantification of the effective hydrogen peroxide concentration encountered by a neighboring organism such as *Aa*. This introduces SECM for use in such real-time mapping of local hydrogen peroxide concentration in a biofilm and determination of the consumption of hydrogen peroxide in a polymicrobial biofilm during spatial scanning. This allows us to measure the effective concentration of hydrogen peroxide in situ, the flux of hydrogen peroxide at the bacterial surface, and determine how it might shape polymicrobial interactions.

5.2 MATERIALS AND METHODS

Chemicals

Sulfuric acid (94–98%, trace metal grade), potassium nitrate, potassium chloride, agar purified grade), and o-phosphoric acid (85%) from Fisher Scientific were used as received. Fresh solutions of hydrogen peroxide were made before each experiment by diluting a concentrated commercial aqueous solution (30% (v/v), Sigma-Aldrich GmbH). All solutions were prepared with deionized Milli-Q water.

Bacterial Strains Culture and Preparation

Streptococcus gordonii strain DL1, *Aggregatibacter actinomycetemcomitans* Y4 and *Aa* Y4 *kataA*- containing an insertion mutant of the catalase-encoding gene *kataA* (6) were used in our study. Broth cultures were grown by shaking at 150 RPM at 37 °C in a 5% CO₂ atmosphere unless specified otherwise. The growth medium included Tryptic soy broth +5% yeast extract (TSBYE) or CDM (5).

Sg was inoculated from a single colony into 3 mL TSBYE broth and grown overnight to an approximate cell density of 3×10^9 cells / mL (A600 = 3). Cells were next diluted into 3 mL of TSBYE to a density of A600 = 0.05 and grown to a density of A600 = 0.5. 2 mL of cells were collected via centrifugation at $10,000 \times g$ for 5 min and resuspended in 1 mL phosphate buffered saline (PBS). 25 mm polycarbonate membranes (Whatman, 0.2 µm pore size) were aseptically transferred to the surface of a 100 mm TSAYE agar plate. 50 µL of the above cell suspension ($\sim 5 \times 10^7$ cells) was spotted directly onto the membrane surface and uniformly spread to cover the entire membrane using a sterile spreader. Cell suspensions were dried on the membranes for approximately 10 min in a laminar flow hood to form a colony biofilm. TSAYE plates and membranes containing bacterial biofilm were transferred back to 37 °C and 5% CO₂ environment for approximately 1 h.

Aa strains were grown overnight in 3 mL TSBYE to a cell density of A600 = 1; then diluted into 3 mL of TSBYE to a density of A600 = 0.05. Cells were then grown to a density of A600 = 0.5 and 2 mL were centrifuged as above and resuspended in 1 mL of PBS. Cells were then diluted 1:10 in PBS buffer. 5 µL of cell suspension (corresponding to $\sim 5 \times 10^6$) cells were spotted directly on the center of the *Sg* coated membrane prepared as above prior to the final 1 h incubation step at 37 °C. The polycarbonate membrane, as a result, had 25 mm bacterial biofilm of *Sg* with a spot of 5 to 7 mm *Aa* in the middle. Biofilm preparations with the *kataA*- mutant were performed identically.

Ultramicroelectrode Fabrication

Gold (99.99 %) wire, 25 μm diameter, from Goodfellow was used to fabricate the SECM tip. First it was fabricated by heat-sealing the corresponding metal wire under vacuum in a borosilicate glass capillary. Then it was polished and shaped conically by a wheel with 180-grid Carbimet paper disks and micropolishing cloth with 1.0, 0.3, and 0.05 μm alumina. The tip used in this study was sharpened to $\text{RG} = 2$, where RG is the ratio between the radius of the glass sheath and the radius of the active electrode surface. Before each experiment, the Au tip was polished with alumina paste (0.3 and 0.05 μm) on microcloth pads (Buehler), sonicated for 15 min in water, and then electrochemically cleaned by cycling between 0.2 and 1.4 V in 0.1 M sulfuric acid for 40 cycles to a constant CV. 0.5 mm tungsten wire from Alfa Products was used as an auxiliary electrode. $\text{Ag} | \text{AgCl} | 3 \text{ M KCl}$ was used as reference electrode to which all potentials for electrochemical experiments are referred.

Calibration Curves for H_2O_2 in CDM

Calibration curves for H_2O_2 were collected in the presence of a *Sg* biofilm. In order to be consistent with our real-time measurements, we strictly followed the same procedure and carried out the calibration curve measurements in the same way. The *Sg* biofilm was incubated in 1.5 mL CDM for at least 1 h before different aliquots of H_2O_2 solution (0.03%, v/v) were added into CDM solution to make H_2O_2 concentrations ranging from 0.06 mM to 1.6 mM. The H_2O_2 oxidation currents were measured by pulsing the Au ultramicroelectrode (UME) from 0.55 V to 0.80 V, 5 min after H_2O_2 was added each time. No glucose was added to the CDM so that *Sg* cells in the biofilm would not produce any extra H_2O_2 during calibration measurements.

Stability Tests

Stability is a very important issue since we normally need to run the experiments for a long duration. Because CDM is a defined culture medium with many components, and the temperature needs to be maintained at approximately 37 °C during the experimental process, in such conditions, the SECM tip (Au UME) is prone to contamination, and H₂O₂ tends to decompose as well. As a result, a current decay is usually observed as time proceeds. To make sure that our measurements were valid during this long duration, we carried out a series of stability tests.

Real-Time Electrochemical Monitoring of Hydrogen Peroxide by SECM on a *Sg* Biofilm

An *Sg*-coated 25 mm polycarbonate membrane was prepared as described in Bacterial Strains Culture and Preparation. The membrane was then transferred carefully from the agar plate onto a piece of double sided tape (3M: 34-8517-3569-5) fixed to the bottom of a 35 mm Petri dish (Becton Dickinson). The dish was later put on a home built copper heating plate on the CHI 920C SECM stage (CH Instruments) to maintain a constant temperature of 37 °C. The experimental setup for SECM measurements is shown in Figure 5.1 A and B. The biofilm was incubated for 1 h at 37 °C after adding 1.5 mL of CDM solution to the 35 mm Petri dish. During this period, an approach curve (tip current, i_T , vs. distance, d) was taken over the biofilm with oxygen as a mediator by holding the tip at -0.6 V (seen in Figure 5.1C). Tip-membrane distance was then fixed at 200 μ m. The background was recorded at the same height by pulsing the tip from 0.55 to 0.80 V for 10 s. 15 μ L of 1 M of glucose was added to the existing 1.5 mL of CDM buffer to make the final glucose concentration 10 mM. The hydrogen peroxide concentration over the biofilm was measured as a function of time by pulsing the tip at the same potential range of background recording every 5 min.

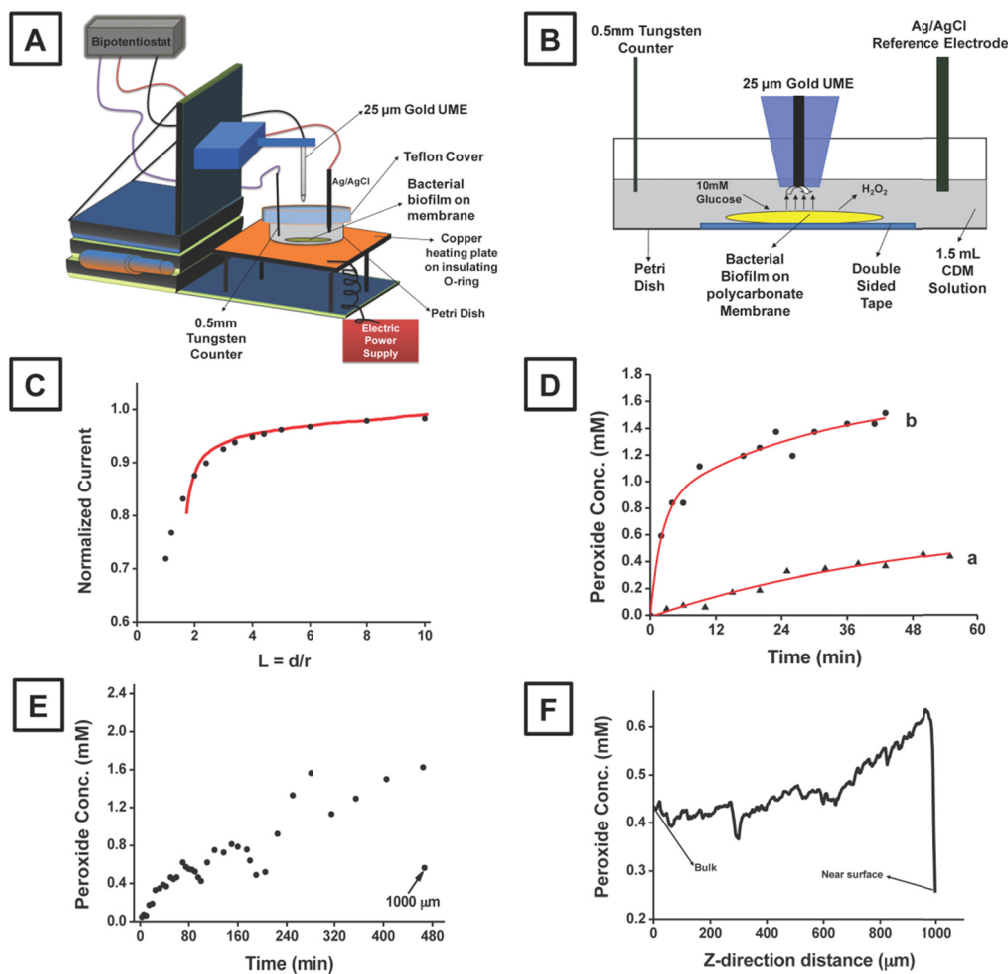


Figure 5.1: Real time quantitative detection of peroxide produced by biofilm

(A) Schematic diagram of SECM for real-time measurement of hydrogen peroxide formation in a bacterial biofilm. (B) Schematic diagram of an electrochemical experimental setup for A. (C) An approach curve (solid line) with oxygen as a mediator in CDM at 37 °C, the tip potential was held at -0.6 V, and the scan rate was 25 $\mu\text{m/s}$. The points represent the theoretical negative feedback approach curve above an electrically insulating surface. (D) Plots of the concentration of hydrogen peroxide produced by Sg in biofilm as a function of time at different distances between the Au UME and the biofilm (a, 200 μm , b, 100 μm). (E) Plot of hydrogen peroxide concentrations produced by a Sg biofilm as a function of time over 8 h. (F) An approach curve with hydrogen peroxide produced by a Sg biofilm as a mediator in CDM at 37 °C, the tip potential was held at 0.8 V, and the scan rate was 25 $\mu\text{m/s}$. The z-direction axis measures distance travelled from bulk to the surface, with the sharp drop indicating the surface position.

Y-scan and Approach Curve SECM Experiment on a *Sg* and *Aa* Coculture Biofilm

The biofilm sample was prepared by the same method as described in Bacterial Strains Culture and Preparation. The only difference in this sample was a 5 to 7 mm diameter spot of *Aa* in the middle of the *Sg* biofilm. As shown in Figure 5.2A, the location of the *Aa* spot was marked on the outside of the Petri dish with a marker. The same SECM imaging procedure was followed as before with the tip-substrate distance at 200 μm and the background current recorded at the same height. First, the growth of the hydrogen peroxide concentration was observed at $d = 200 \mu\text{m}$ over the *Sg* area for 1 h. The tip was then scanned at 150 $\mu\text{m/s}$ in the *y*-direction at $d = 200 \mu\text{m}$ from *Sg-Aa-Sg* to record the hydrogen peroxide concentration across the two different bacterial populations. Approach curves were performed using hydrogen peroxide as a mediator at three different points: one on *Sg* and one on *Aa* and another one again on *Sg*.

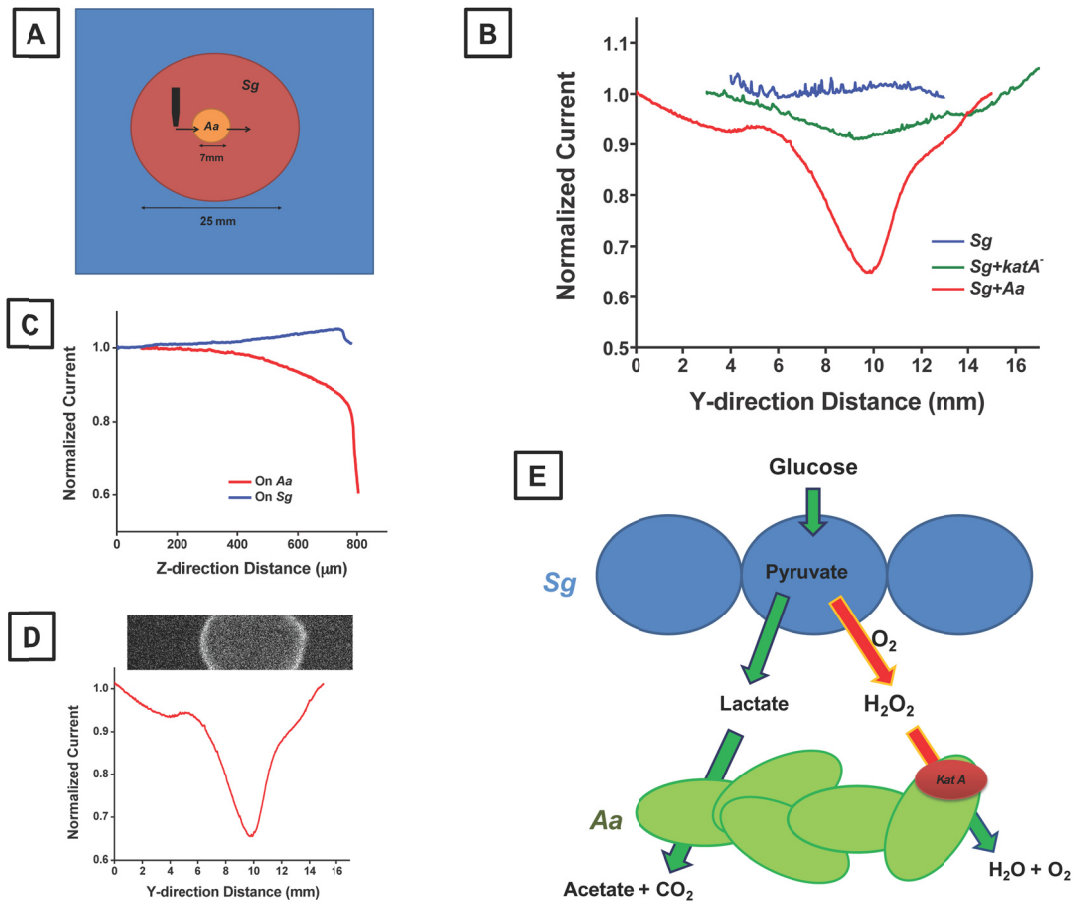


Figure 5.2: Real time spatial mapping of local peroxide produced by polymicrobial (*Aa* and *Sg*) biofilm

(A) Schematic diagram of tip scan across the region of a mixed species biofilm in the order of *Sg*-*Aa*-*Sg*. (B) Normalized current changes of an SECM y-scan over *Sg* alone, mutant *Aa* in an *Sg* film, and wild-type *Aa* in an *Sg* film, respectively, at 37 °C. Tip potential was held at 0.8 V, and scan rate was 150 $\mu\text{m/s}$. Green is pure *Sg*, blue is mutant *Aa* with *Sg*, red is wild *Aa* with *Sg*. (C) Approach curves for pure *Sg* and wild-type *Aa* region in an *Aa* + *Sg* biofilm (B, red curve). (D) Normalized current changes of an SECM y-scan over *Aa* + *Sg* biofilm extrapolated to identical biofilms using *Aa* carrying the *katA*-lux reporter vector. Light production (in white) is indicative of promoter response to hydrogen peroxide. (E) Model for the role of hydrogen peroxide in an *Sg* and *Aa* cocultured biofilm.

Fluorometric Measurements of Hydrogen Peroxide

Hydrogen peroxide production was measured using the Amplex Red hydrogen peroxide assay kit (Invitrogen) using the manufacturer protocols. *Sg* was cultured as mentioned above and 5×10^7 cells were either spread onto a 25 mm polycarbonate membrane to form a biofilm and then placed in a 35 mm Petri dish or resuspended directly in 1.5 mL of CDM + 10 mM glucose. Biofilm cells were covered with 1.5 mL CDM + 10 mM glucose. Aliquots were taken from each culture in triplicate at 2, 4, and 8 h then measured using the above assay kit on a BioTek Synergy MX (BioTek) fluorometric microplate reader at excitation/ emission values of 530 nm and 590 nm, respectively. For lux reporter experiments we used the *Aa katA-lux* reporter strain (4) in place of *Aa* WT in the biofilm overlay. *Aa katA-lux* was grown to the exponential phase and 5×10^8 cells were isolated via centrifugation at $10,000 \times g$ for 10 min. Cells were resuspended in 5 μ L TSBYE and placed onto the surface of the *Sg* biofilm prepared as above. Biofilms were incubated on the surface of a TSAYE plate at 37 °C for approximately 1 h, then image captures were exposed for 10 min in a Syngene G:BOX (Syngene) using the manufacturers software. Image sizes were scaled to the x-axis using Photoshop CS5 (4).

Confocal Laser Scanning Microscopy

Cells were grown and prepared as described in “Bacterial Strains Culture and Preparation” section, except for the replacement of *Aa* Y4 with a constitutive GFP-producing *Aa* Y4 strain. Membranes were stained in 3 mL of PBS containing 60 μ M propidium iodide and incubated for 10 min prior to rinsing in PBS 3x at 3 mL each. Membranes were then resuspended in 3 mL PBS and observed through a 40x water immersion lens with an Olympus FV1000 confocal microscope. Excitation was performed using a 488 nm Ar laser and green and red channels were separated using

standard filter settings. Micrographs were acquired at 400x magnification in 1 μm z-axis step sizes. Image processing was performed using Imaris software.

Simulations

Because the electroactive species hydrogen peroxide or P moved toward and away from the electrode surface only because of a concentration gradient, Fick's second law of diffusion was used in the simulation. The concentration of species P was given as $C(r,z,t)$ and the diffusion equation in cylindrical coordinates was described as

$$\frac{\partial c}{\partial t} = D \left(\frac{\partial^2 c}{\partial r^2} + \frac{1}{r} \frac{\partial c}{\partial r} + \frac{\partial^2 c}{\partial z^2} \right)$$

where r and z are the coordinates as shown in Figure 5.3; t represents time; C and D represent the concentration and diffusion coefficient of species P.

The simulation model described above was solved by a finite element method in 2D axial symmetry dimension where the mesh was increased in exponential grid fashion to generate a two dimensional grid. A finer mesh distribution was used at the regions where sharp changes in the concentration gradients were noticed.

Initially the hydrogen peroxide concentration in the solution was zero and the flux in the bulk boundary was set as zero. The diffusion coefficient of hydrogen peroxide in the solution was taken as $1.5 \times 10^{-9} \text{ m}^2/\text{s}$. The hydrogen peroxide generated from the biofilm surface was assumed to be a constant flux problem. Henceforth, the flux ($\text{mol}/\text{m}^2/\text{sec}$) value was adjusted at the biofilm surface to fit the experimental hydrogen peroxide response curve or hydrogen peroxide concentration vs. time (s) measured by SECM tip. The 25 μm tip ($\text{RG} = 10$) was located 100 μm away from the substrate to record hydrogen peroxide concentration and was held at diffusion controlled potential to avoid kinetic complications. The current at the electrode was calculated as

$$I_{\text{tip}} = \int_{r=0}^{r=a} 2\pi n F D r \frac{\partial c}{\partial z} dr$$

where $n = 1$; $F = 96485$ C/mol; and $D = 1.5 \times 10^{-9}$ m²/s; a = tip radius, m. The current obtained by the simulation was converted to hydrogen peroxide concentration using the same calibration curve used in experimental hydrogen peroxide measurement.

Simulations were performed with Comsol Multiphysics 3.3 on a 2.8 GHz Intel Pentium IV processor and 2 GB RAM desktop PC.

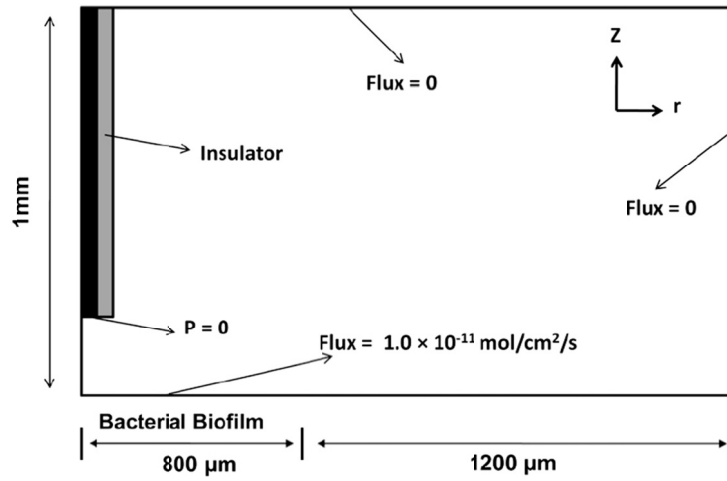


Figure 5.3: The schematic diagram of Comsol Multiphysics model used for simulation.

5.3 RESULTS

Calibration Curves for H₂O₂ in CDM

Figure 5.4 shows the results obtained in the presence of a Sg biofilm. A linear relationship ($I = -0.299C - 0.0069$, $R^2 = 0.99533$) between the current and H₂O₂ concentration was observed at H₂O₂ concentrations smaller than 1.0 mM (Figure 5.5). As concentration goes above 1.0 mM, the curve levels off and deviates from the linear portion. Most of the H₂O₂ concentrations obtained in our real time in vitro measurements were within 1 mM, so we used the linear portion of the calibration curve to calculate H₂O₂ concentration (Figure 5.5).

In order to test if our calibration curve was working properly, we intentionally added 0.5 mM H₂O₂ to a 1.5 mL Sg biofilm suspended in CDM in a Petri dish, and the current response was measured to be 0.15 nA, which corresponds to 0.5 mM based on the calibration curve in Figure. 5.5. This indicated that our calibration curve was indeed valid for our experiments.

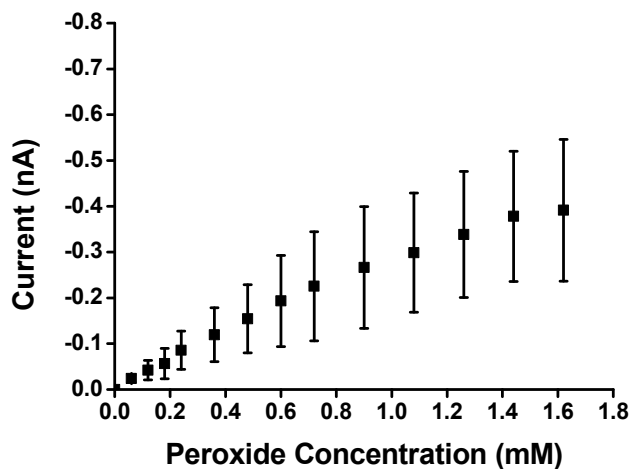


Figure 5.4: Calibration curve for H_2O_2 with concentrations ranging from 0.06 ~1.6 mM in CDM with a *Sg* biofilm at 37°C.

Error bars were calculated based on three independent measurements.

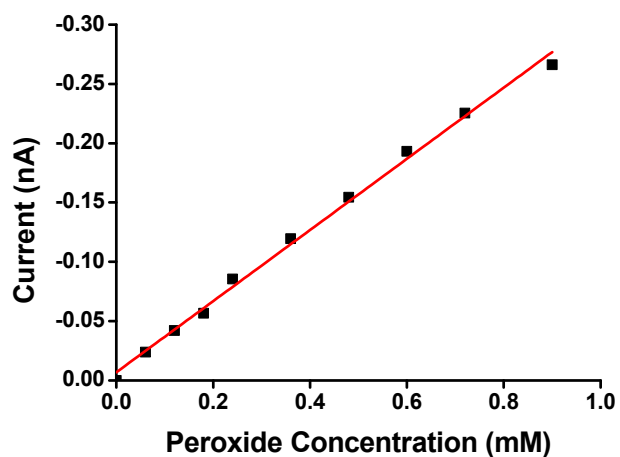


Figure 5.5: Calibration curve for H_2O_2 over the concentration range from 0.06 ~1.0 mM in CDM with a *Sg* biofilm at 37°C.

Stability Tests

Figure 5.6 shows the results of stability tests performed in the absence of *Sg*. The current response for 0.2 mM H₂O₂ in 1.5 mL CDM with 10 mM glucose was measured as a function of time. As shown in Figure 5.6, the H₂O₂ oxidation current decreases slowly with time. After 30 min, the current decreased only approximately 20%, which means that the tip has relatively good stability in low H₂O₂ concentration.

Another stability test was carried out in the presence of a *Sg* biofilm. A relatively high H₂O₂ concentration (0.6 mM) was tested this time. H₂O₂ current was measured every 5 min up to 35 min, and the result is shown in Figure 5.7. The current of H₂O₂ decreased gradually with time. The rate for the current decay is faster (43% current drop in first 20 min) in the presence of *Sg* cells.

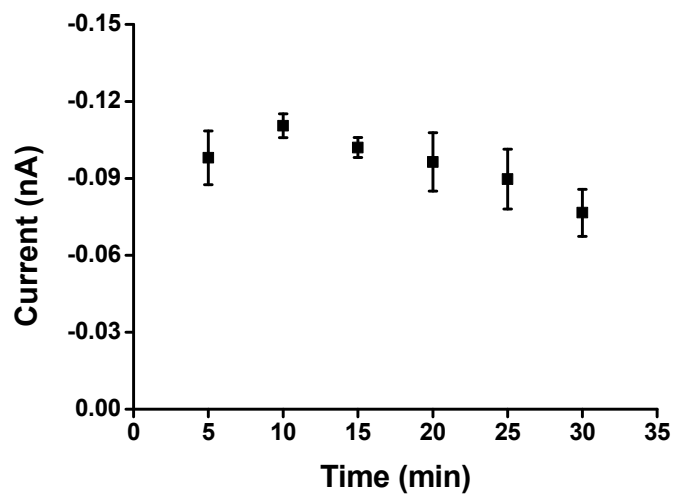


Figure 5.6: Amperometric current of Au UME as a function of time in 0.2 mM H₂O₂ CDM solution at 37°C.

Error bars were calculated based on at least three independent measurements.

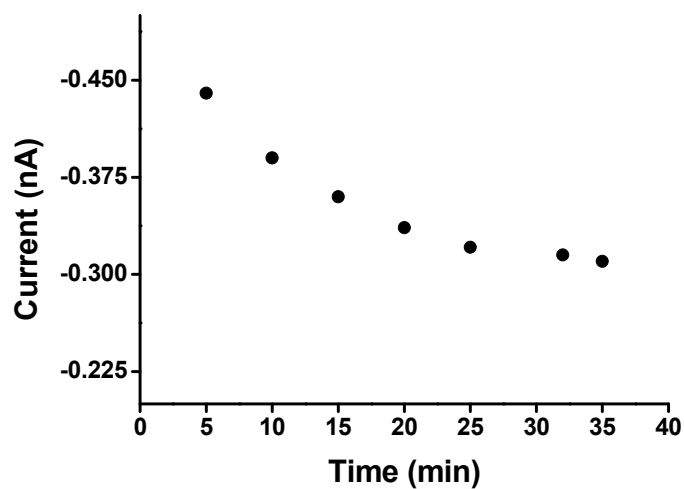


Figure 5.7: Current response of 0.6 mM H₂O₂ as a function of time in the presence of a *Sg* biofilm.

Real-Time Quantitative Measurement of Hydrogen Peroxide Produced by Living *Sg* Colony Biofilms with SECM

Figure 5.1D shows the formation of hydrogen peroxide by a *Sg* colony biofilm (25) as a function of time (min) at 100 μm and 200 μm , respectively, above the film. Each concentration point in the plot corresponds to the chronoamperometric current due to hydrogen peroxide oxidation at a particular time, e.g., $t = 30$ min. The concentration was calculated from the current recorded at 10 s using the calibration curve shown in Figure. 5.4.

For a pure *Sg* biofilm with the tip 100 μm away, the hydrogen peroxide concentration increased initially for about 10 to 12 min and then tended to a quasi-steady-state concentration of approximately 1.4 mM. This behavior can be understood in terms of a substrate, the biofilm, with a sufficiently large area that diffusion from it can be considered linear. However, as is well known from the behavior of electrodes generating a species with a constant flux, diffusional behavior can only be maintained, even with careful isolation of the cell from vibrations, for a time of 5 to 10 min. At some stage natural convection begins and the current then tends to a steady state governed by the convection rate (26). When the tip was placed at 200 μm above the membrane for the same biofilm, hydrogen peroxide concentration was found to be 0.4 mM after 60 min.

To obtain the most relevant measurement of the capacity of streptococcal released hydrogen peroxide, a relatively long monitoring time (8 h) for hydrogen peroxide generation from *Sg* was performed as shown in Figure 5.1E. After 8 h, the tip was raised to 1,000 μm away from the membrane and hydrogen peroxide concentration at that region was found to be about 0.5 mM, much smaller than the steady-state concentration of hydrogen peroxide closer to the membrane (e.g., ~ 1.6 mM), indicating that even with natural convection, there is a concentration profile of hydrogen peroxide away from the membrane. To show this, an approach curve was performed from 1,000 μm away toward the membrane, as shown in Figure 5.1F. A gradual increase in tip current due to an

increase of hydrogen peroxide concentration was observed over a distance of several hundred μm as the tip approached the membrane, indicating that somewhat higher hydrogen peroxide concentrations exist in the local area near the biofilm. The sharp decrease of tip current at 1,000 μm in Figure 5.1F is due to a blocking effect when the tip touched the membrane. The absolute value of hydrogen peroxide concentration near the surface of the biofilm in Figure 5.1F was smaller than that shown in Figure 5.1D. This difference might be due to a difference in time for data acquisition. The current found through an approach curve over the 1,000 μm distance was measured over a long duration compared to the 10 s pulse measurement (Figure 5.1D). However the bulk hydrogen peroxide concentrations were the same in both cases (Figure 5.1 D and F).

Y-scan and Approach Curve SECM Experiments over a *Sg* and *Aa* Cocultured Bacterial Biofilm

Figure 5.2B shows the results of a SECM y-scan over *Sg* only, *Sg* + *Aa*, and *Sg* + *Aa katA*- biofilms. All currents were normalized for comparison purposes. The y-scan data obtained with the pure *Sg* biofilm shown in Figure 5.2B (green curve) is fairly constant, showing uniform behavior across the film. The *Sg* biofilm modified with a 5 to 7 mm spot of *Aa* in the center (Figure 5.2B, red curve), however, showed an evident current decrease (valley) over the *Aa* region on the membrane. The width of the valley was about 7,000 μm , consistent with the diameter of the *Aa* spot made on the *Sg* biofilm (seen in Figure 5.2D). The current in the valley dropped to approximately 0.66 of the current for the *Sg* region. The blue curve in Figure 5.2B displays the y-scan over the *Aa katA*- mutant doped *Sg* biofilm. It shows a slight current dip over the *Aa katA*- mutant region as well; here the current dropped only to approximately 0.91 compared to *Sg*, indicating that a higher concentration of hydrogen peroxide is observed on the *Aa* mutant lacking catalase (*katA*) compared to wild-type *Aa*.

Approach curves were collected over the pure *Sg* region ($y = 1,000 \mu\text{m}$) and the *Aa* region ($y = 10,000 \mu\text{m}$) in the same membrane, respectively (see Figure 5.2C). The approach curve over the *Sg* region showed a steady current increase as the tip approached the *Sg* membrane over a distance of $300 \mu\text{m}$, indicating that a higher concentration of hydrogen peroxide was found near the *Sg* membrane. Over the *Aa* region, however, a current drop was observed as the tip moved closer to the *Aa* surface, showing a negative deviation from the usual negative feedback mode approach curve as a result of shielding because of consumption of hydrogen peroxide in the *Aa* region.

Effect of the Number of *Sg* Bacteria on H_2O_2 Current Response

We also tested to see if the amount of *Sg* cells would affect H_2O_2 measurements. In this experiment, $0.5 \text{ mM } \text{H}_2\text{O}_2$ was added to 1.5 mL CDM solution. The current response of $0.5 \text{ mM } \text{H}_2\text{O}_2$ was measured 10 min later each time when one aliquot of 0.5 mL of *Sg* suspension (2.5×10^8 *Sg* cells) was added into the above solution. To make the concentration of H_2O_2 constant during the measurements, extra H_2O_2 was added ($28 \mu\text{L}$ $0.03\% \text{ H}_2\text{O}_2$) each time to compensate the volume change due to the addition of 0.5 mL *Sg* suspension. A total of 4 aliquots of *Sg* suspension were added, and it was found that the current responses did not show any significant changes (Figure 5.8). This indicated that the number of *Sg* did not significantly affect H_2O_2 detection.

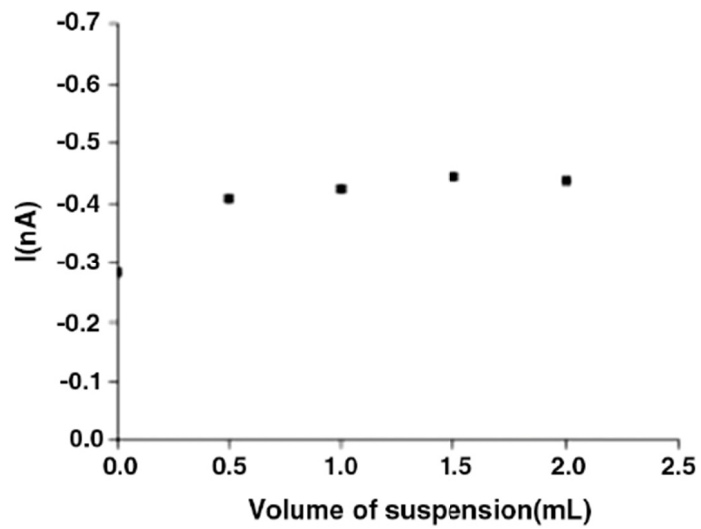


Figure 5.8: Effect of *Sg* numbers on H₂O₂ detection. 1.0 mL of *Sg* suspension contain 5×10^8 *Sg* cells.

5.4 DISCUSSION

Real-Time Quantitative Measurement of Local Hydrogen Peroxide Concentration Produced by a *Sg* Biofilm

Sg-produced hydrogen peroxide was measured with a SECM tip located approximately 100 to 200 μm above the biofilm in the experimental setup as shown in Figure 5.1 A and B. The biofilm itself was 10 to 20 μm thick as measured by confocal laser scanning microscopy. Although individual measurements were expected to be different because of biological variability (e.g., cell condition, number of the bacterial cells on the membrane), most concentration vs. time profiles we observed were very similar in shape to that shown in Figure 5.1D. A quasi steady-state hydrogen peroxide concentration of 1.4 mM was observed (Figure 5.1D, curve b) at 100 μm away from biofilm, while only 0.4 mM hydrogen peroxide was recorded at 200 μm over 60 min in the presence of 10 mM glucose as shown in Figure 5.1D, curve a. As indicated earlier, this difference in hydrogen peroxide measurement may be due to mass transfer of hydrogen peroxide produced by the biofilm into the bulk phase by natural and induced convection. In addition, a slower response of hydrogen peroxide above the biofilm is observed at 200 μm because it takes a much longer time to build up detectable hydrogen peroxide concentrations at this distance through diffusion and convection. This is supported by Figure 5.1E, where a higher hydrogen peroxide concentration (1.6 mM) is observed at 200 μm away for the same type of *Sg* biofilm when exposed to 10 mM glucose for 8 h.

Figure 5.10 shows the fitted simulated curve demonstrating diffusion of hydrogen peroxide from the film to the SECM tip could be fit to the experimental response by the biofilm upon exposure to 10 mM glucose. The simulated curve (the solid line) fit the experimental data (dots) for about 10 min and then began to deviate because of the onset of natural convection during measurement (not considered in the simulation model). However, the response for the first 10 min could be used to predict the flux at the biofilm

surface. As discussed previously, SECM was a very useful tool in measuring the local concentration of peroxide above the biofilm or 100 μm from the biofilm surface, it still did not give the concentration or flux at the biofilm surface. With the aid of digital simulation, the exact hydrogen peroxide flux at the biofilm surface can be calculated as in SECM experiments, when the tip-substrate distance is known. Briefly, the simulation assumes only diffusional mass transfer and a constant hydrogen peroxide flux from the biofilm surface to a 25 μm SECM tip ($\text{RG} = 10$) at a distance of 100 μm away from the surface. The fitted hydrogen peroxide flux at the biofilm surface was determined to be $1.0 \times 10^{-11} \text{ mol/cm}^2/\text{s}$. Assuming a dimension of each bacterium is $1.5 \mu\text{m} \times 0.8 \mu\text{m}$, the calculated bacterial density was $8.3 \times 10^7/\text{cm}^2$. So, approximately $1.2 \times 10^{-19} \text{ mol}$ ($\sim 70,000$ molecules) of hydrogen peroxide effluxed from a single bacterium at the film surface per second. This gives an important estimate of the amount of hydrogen peroxide produced at the bacteria surface, which may be useful for elucidating the defense mechanism of a bacterial species or interactions with other bacterial species in terms of metabolite or hydrogen peroxide concentration.

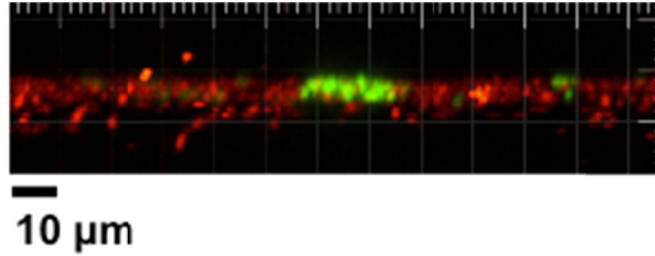


Figure 5.9: Confocal laser scanning micrograph of a mixed species biofilm. *S. gordonii* (red) and *Aa* (green) were cocultured in a colony biofilm.

Green and red channel fluorescence are due to *Aa* GFP expression and propidium iodide staining respectively. Images were taken at 400x magnification with a z-step interval of 1 μm .

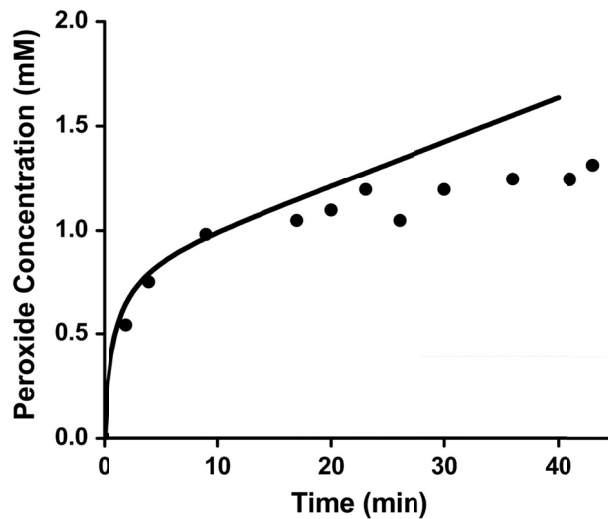


Figure 5.10: The simulated (solid line) hydrogen peroxide metabolite efflux from bacterial biofilm of *Sg* at a distance of 100 μm from surface compared to experimental measurements (dots). The diameter of the SECM tip used was 25 μm (RG = 10).

Interestingly, significantly lower concentrations (20–40 μM range) of hydrogen peroxide are observed in Table 5.1 both for biofilm as well as cell suspensions when measured by taking aliquots of bulk solution using a commercial fluorometric assay. Similar bacterial numbers and incubation times in 1.5 mL of chemically defined medium (CDM) culture solution were used for the same time periods in both methods for comparison. Results suggest that the local hydrogen peroxide concentration is significantly higher for a biofilm in comparison to the bulk phase and that SECM is an ideal analytical tool due to its ability to measure such concentrations close to the biofilm surface. However, it is difficult to understand the results in terms of diffusion from the bacteria surface at times longer than about 10 min at most.

H₂O₂ concentration at different experimental setup	Time (h)		
	2	4	8
Suspension fluorometric measurement	19.2 μ M	20.2 μ M	30.6 μ M
Biofilm fluorometric measurement	21.0 μ M	19.0 μ M	30.6 μ M
Biofilm electrochemical measurement (at 200 μ m away)	0.7 mM	0.9 mM	1.6 mM

Table 5.1: Comparison of hydrogen peroxide production concentration from *Sg* by fluorometric and electrochemical measurement.

It is also important to carefully consider the conditions at which the metabolite concentration measurements are made before considering any of their effects on bacterial functions or their interactions with other bacterial species; especially for toxic molecules such as hydrogen peroxide. As observed from our SECM experiments, the *Sg* biofilm is able to produce sufficient hydrogen peroxide (mM range) to inhibit the growth of many bacteria, but such conditions prevail only at a very close distance from the biofilm surface. The presence of higher hydrogen peroxide concentrations close to the surface ($\sim 200 \mu\text{m}$) is also observed in the hydrogen peroxide approach curve (shown in Figure 5.1F). The sharp drop in current or hydrogen peroxide concentration happens when the tip touches the surface and thus blocks any further diffusion of hydrogen peroxide to the tip.

Fluorescent dyes are available to detect reactive oxygen species such as hydrogen peroxide and superoxides in individual cells; however, such techniques only provide qualitative information about these metabolites. Thus, SECM has a significant advantage in measuring local concentrations spatially across a biofilm to elucidate how mass transfer affects this complex and dynamic biological system; existing biological analytical methods are unable to obtain such information.

KatA Mediated Decomposition of Hydrogen Peroxide in a Mixed Species Biofilm

The y-direction SECM scan shown in Figure 5.2B (red curve) over cocultured *Sg* and *Aa* wild-type biofilms reveals a unique hydrogen peroxide concentration profile across two different regions. The current from hydrogen peroxide oxidation at the tip while scanning over the *Aa* region exhibits a lower concentration ($\sim 34\%$ decrease) based on the normalized currents at the deepest point, indicating that hydrogen peroxide is consumed by *Aa*. The reason for this consumption can be explained as shown in the model in Figure 5.2E. According to the proposed model (4), wild-type *Sg* bacteria can

produce hydrogen peroxide by metabolizing glucose in the presence of oxygen. *Aa* is able to flourish in this environment by decomposing hydrogen peroxide using the KatA enzyme. This model has been validated in our experiments by performing y-scans over *Aa katA-*, which is unable to detoxify hydrogen peroxide in the presence of *Sg*. As shown in Figure 5.2B (blue curve), no significant decrease in y-scan current or concentration is noticed, thus confirming no hydrogen peroxide consumption by *Aa katA-*. The slight dip in y-scan current over the mutant *Aa* zone is, however, due to lower hydrogen peroxide concentration over a void space created by the nonconsuming and non-hydrogen-peroxide-producing mutant *Aa*. Because the *Aa* spot is surrounded by hydrogen peroxide producing *Sg* bacteria (Figure 5.2A), hydrogen peroxide can diffuse from the surrounding area and subsequently fill the empty *Aa* spot. No dip in current is observed in Figure 5.2B (green curve) when the tip is scanned over the *Sg*-only bacterial biofilm because no spatial change in hydrogen peroxide concentration in the y-direction is expected at a given height.

5.5 CONCLUSIONS

By using SECM, we measured the local hydrogen peroxide concentration produced by *Sg* biofilms in real time and found it to be significantly different than suspension hydrogen peroxide measurements. The concentration of hydrogen peroxide can reach 1.2 mM with the tip placed 100 μm away from the biofilm. A quasi-steady-state concentration was always observed, as hydrogen peroxide is likely decomposed by *Sg* to prevent injury by excessive hydrogen peroxide concentrations. Furthermore, we also measured local hydrogen peroxide concentrations across *Sg* and *Aa* cocultured biofilms with a one-directional scan SECM technique. Our results confirmed not only that *Aa* catalase activity was critical for decreasing local hydrogen peroxide concentration but also that this decomposition effect was only observed in the immediate vicinity of *Aa*.

Quantitative investigation with these and other bacteria will help us to understand the mechanism of how hydrogen peroxide influences the ecology of mixed species communities.

5.6 ACKNOWLEDGEMENT

Allen J Bard and Dipankar Koley acknowledge support from the Robert A. Welch Foundation (F-0021) and the National Science Foundation (CHE-0808927). This project was conducted in collaboration with Marvin Whiteley Lab. The biological samples were prepared by Matthew M. Ramsey. All the electrochemical measurements were performed by Xiuhui Liu, Xiaole Chen and Dipankar Koley. Simulations were done by Dipankar Koley.

5.7 REFERENCES

- ¹ Barnard JP, Stinson MW (1999) Influence of environmental conditions on hydrogen peroxide formation by *Streptococcus gordonii*. *Infect Immun* 67:6558–6564.
- ² De Stoppelaar JD, et al. (1969) The relationship between extracellular polysaccharideproducing streptococci and smooth surface caries in 13-year-old children. *Caries Res* 3:190–199.
- ³ Kreth J, et al. (2008) Streptococcal antagonism in oral biofilms: *Streptococcus sanguinis* and *Streptococcus gordonii* interference with *Streptococcus mutans*. *J Bacteriol* 190:4632–4640.
- ⁴ Ramsey MM, Whiteley M (2009) Polymicrobial interactions stimulate resistance to host innate immunity through metabolite perception. *Proc Natl Acad Sci USA* 106:1578–1583.
- ⁵ Brown SA, Whiteley M (2007) A novel exclusion mechanism for carbon resource partitioning in *Aggregatibacter actinomycetemcomitans*. *J Bacteriol* 189:6407–6414.

- ⁶ Thomson VJ, et al. (1999) Direct selection of IS903 transposon insertions by use of a broad-host-range vector: Isolation of catalase-deficient mutants of *Actinobacillus actinomycetemcomitans*. *J Bacteriol* 181:7298–307.
- ⁷ Jakubovics NS, Gill SR, Vickerman MM, Kolenbrander PE (2008) Role of hydrogen peroxide in competition and cooperation between *Streptococcus gordonii* and *Actinomyces naeslundii*. *FEMS Microbiol Ecol* 66:637–644.
- ⁸ Mendoza AG, Liébana J, Castillo AM, de la Higuera A, Piédrola G (1993) Evaluation of the capacity of oral streptococci to produce hydrogen peroxide. *J Med Microbiol* 39:434–439.
- ⁹ Seki M, Iida K, Saito M, Nakayama H, Yoshida S (2004) Hydrogen peroxide production in *Streptococcus pyogenes*: Involvement of lactate oxidase and coupling with aerobic utilization of lactate. *J Bacteriol* 186:2046–2051.
- ¹⁰ Kreth J, Merritt J, Shi W, Qi F (2005) Competition and coexistence between *Streptococcus mutans* and *Streptococcus sanguinis* in the dental biofilm. *J Bacteriol* 187:7193–7203.
- ¹¹ Bard AJ, Mirkin MV, eds. (2001) *Scanning Electrochemical Microscopy* (Marcel Dekker, New York), pp 1–15.
- ¹² Wang X, Yang T, Feng Y, Jiao K, Li G (2009) A novel hydrogen peroxide biosensor based on the synergistic effect of gold-platinum alloy nanoparticles/polyaniline nanotube/chitosan nanocomposite membrane. *Electroanal* 21:819–825.
- ¹³ Mao L, Osborne PG, Yamamoto K, Kato T (2002) Continuous on-line measurement of cerebral hydrogen peroxide using enzyme-modified ring-disk plastic carbon film electrode. *Anal Chem* 74:3684–3689.
- ¹⁴ Liu X, Zweier LJ (2001) A real-time electrochemical technique for measurement of cellular hydrogen peroxide generation and consumption: Evaluation in human polymorphonuclear leukocytes. *Free Radical Biol Med* 31:894–901.

- ¹⁵ Horrocks BR, Schmidtke D, Heller A, Bard AJ (1993) Scanning electrochemical microscopy. 24. Enzyme ultramicroelectrodes for the measurement of hydrogenat surfaces. *Anal Chem* 65:3605–3614.
- ¹⁶ Wittstock G, Schuhmann W (1997) Formation and imaging of microscopic enzymatically active spots on an alkanethiolate covered gold electrode by scanning electrochemical microscopy. *Anal Chem* 69:5059–5066.
- ¹⁷ Wilhelm T, Wittstock G (2003) Analysis of interaction in patterned multienzyme layers by using scanning electrochemical microscopy. *Angew Chem Int Edit* 42:2248–2250.
- ¹⁸ Zhan D, Li X, Zhan W, Fan FF, Bard AJ (2007) Scanning electrochemical microscopy. 58. Application of a micropipet-supported ITIES tip to detect Ag⁺ and study its effect on fibroblast cells. *Anal Chem* 79:5225–5231.
- ¹⁹ Kirchner CN, Träuble M, Wittstock G (2010) Diffusion and reaction in microbead agglomerates. *Anal Chem* 82:2626–2635.
20. Li X, Bard AJ (2009) Scanning electrochemical microscopy of HeLa cells—Effects of ferrocene methanol and silver ion. *J Electroanal Chem* 628:35–42.
- ²¹ Cai C, Liu B, Mirkin MV, Frank HA, Rusling JF (2002) Scanning electrochemical microscopy of living cells. *Anal Chem* 74:114–119.
- ²² Liu B, Rotenberg SA, Mirkin MV (2000) Scanning electrochemical microscopy of living cells: Different redox reactivities of human breast cells and metastatic breast cancer cells. *Proc Natl Acad Sci USA* 97:9855–9860.
- ²³ Fan FRF, Bard AJ (1999) Imaging of biological macromolecules on mica in humid air by scanning electrochemical microscopy. *Proc Natl Acad Sci USA* 96:14222–14227.
- ²⁴ Zhan D, Fan FF, Bard AJ (2008) The Kv channel blocker 4-aminopyridine enhances Ag⁺ uptake: A scanning electrochemical microscopy study of single living cells. *Proc Natl Acad Sci USA* 105:12118–12122.

- ²⁵ Anderl JN, Franklin MJ, Stewart PS (2000) Role of antibiotic penetration limitation in *Klebsiella pneumoniae* biofilm resistance to ampicillin and ciprofloxacin. *Antimicrob Agents Chemother* 44(7):1818–1824.
- ²⁶ Bard AJ (1961) Effect of electrode configuration and transition time in solid electrode chronopotentiometry. *Anal Chem* 33:11–15.

CHAPTER 6: Electrochemical Characterization of Nanoelectrodes using SECM

The nanoelectrodes were generous gift from Nanonics (Israel). After being received from Nanonics, the electrodes were modified as shown in Figure 6.1. The electrodes were adapted for better handling and using in SECM experiment. During assembly the nanoelectrodes were kept in a 100°C oven for 1 h to cure the silver paste. The nanoelectrodes were then numbered and stored in deionized water for further electrochemistry experiments. The nanoelectrode number corresponds to a batch number and an electrode number such as nanoelectrode 2.3 means it's the third electrode from the second batch sent.

TESTING OF NANO-ELECTRODES

The electrodes were tested in 2 mM ferrocene methanol and 0.1(M) Na₂SO₄ using 0.5 mm tungsten wire and Hg/Hg₂SO₄ as counter and reference respectively (Figure 6.2). The diameters of the nanoelectrodes were determined from the steady state current from CV using the formulae $i_{ss} = 4nFrDC$, where r is the radius of electrode and C is the bulk concentration of redox species. No other method such as SEM was used to confirm the diameter of nanoelectrode. The CVs' were obtained for 1 h at every 5-10 min interval to determine the stability of the nanoelectrode. All the electrochemical experiments from henceforth mentioned were done in the solution filtered through a 0.22 μm filter. If the electrodes showed instability after use, they were cleaned in a H₂SO₄ solution as described in the section below.

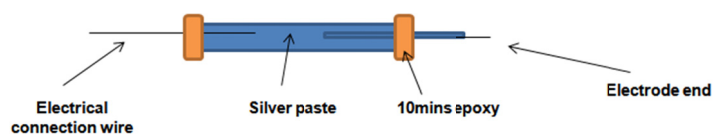


Figure 6.1: The nanoelectrode assembly after being received from nanonics.

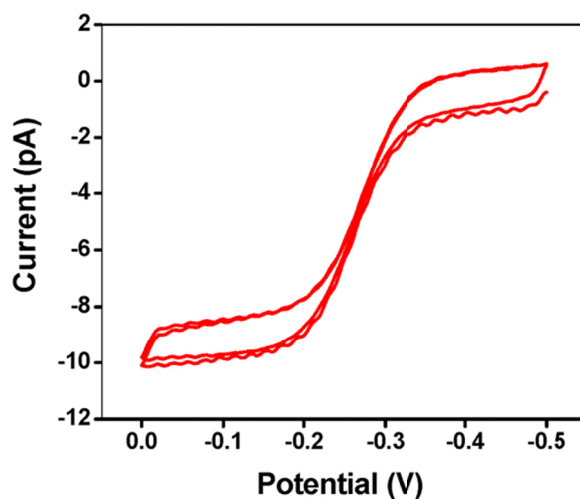


Figure 6.2: The CV of nanoelectrode 2.3 (19 nm approx.) in presence of 2 mM ferrocene methanol & 0.1 (M) Na₂SO₄.

The radius of electrode shown above is 19 nm (approx.). Counter & Reference used: 0.5 mm Tungsten wire & Hg/Hg₂SO₄. Scan rate: 50 mV/s.

CLEANING OF ELECTRODE

The nanoelectrodes were cleaned by dipping the electrodes inside a 0.1 (M) H_2SO_4 acid solution and cycling within the potential range of -0.63 V to 1.1 V (vs. $\text{Hg}/\text{Hg}_2\text{SO}_4$) for 45-60 min (Figure 6.3). After electrochemical cleaning, the electrodes were washed with DI water three times and then used for electrochemical experiment.

Nanoelectrode 2.2 was cleaned with H_2SO_4 by scanning in the same potential range described above for 45 min. The CV was obtained after cleaning showed the radius of 250 nm. The electrode was then “annealed” by keeping it in an oven of 100°C for 1h and then CV was taken in same 2 mM ferrocene methanol solution. But in this case 20 nm radius was observed (Figure 6.4).

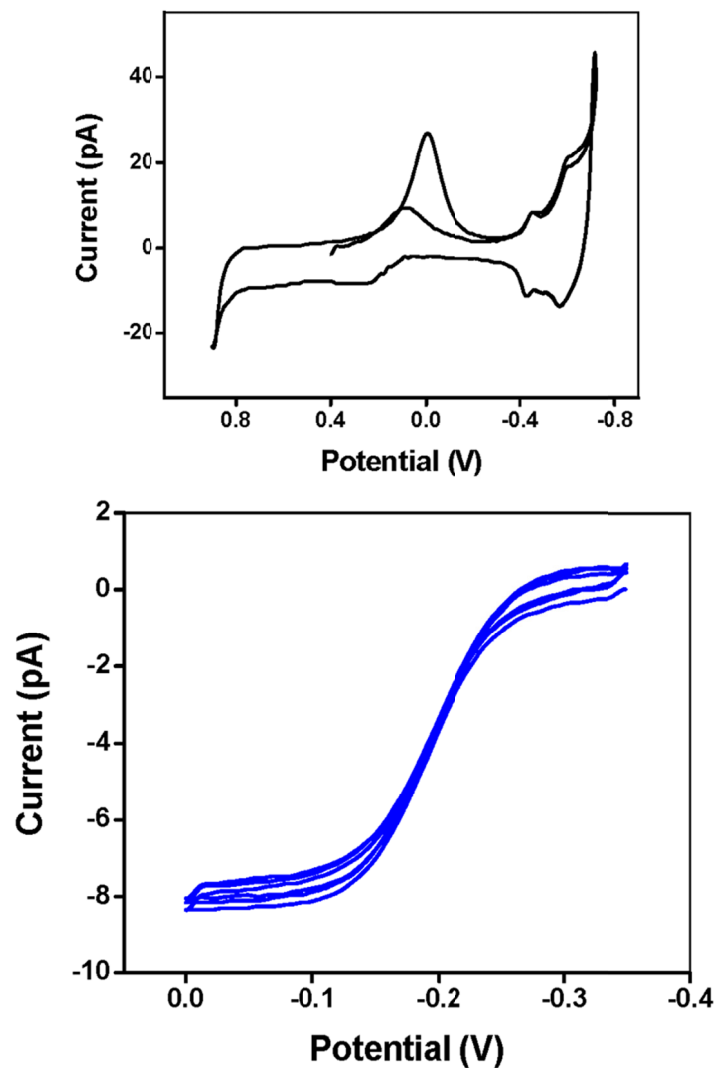


Figure 6.3: Electrochemical cleaning of nanoelectrodes

(*Top*) The cleaning CV of nanoelectrode 1.1 in presence of 0.1 (M) H_2SO_4 . (*Bottom*) CV of nanoelectrode 1.1 of 4 nm radius in presence of 10 mM ferrocyanide and 0.1 (M) Na_2SO_4 after cleaning. Counter & Reference used: 0.5 mm tungsten & $\text{Hg}/\text{Hg}_2\text{SO}_4$ respectively.

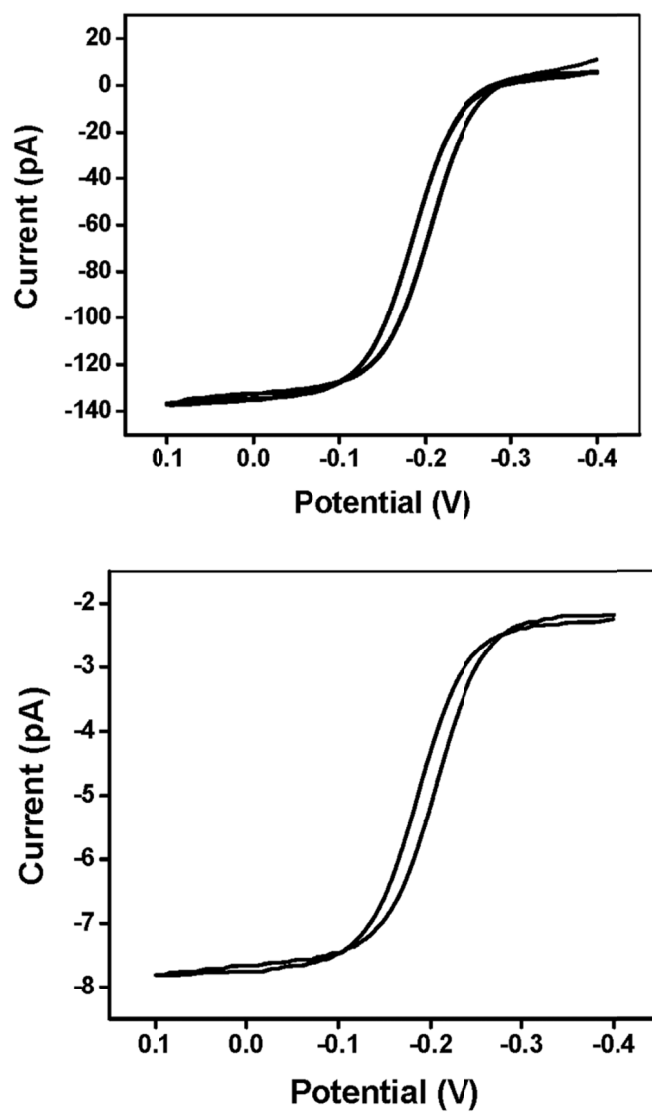


Figure 6.4: Effect of electrochemical cleaning and annealing of nanoelectrode on radius

(*Top*) CV of nanoelectrode 2.2 in 2 mM ferrocene methanol after cleaning with H_2SO_4 . The steady state current of 140 pA (radius 250 nm) was observed. (*Bottom*) CV taken after exposing the nanoelectrode 2.2 to 100°C for 1h. The steady current of 8 pA (radius 10 nm) was observed. Scan rate: 50mV/s.

APPROACH CURVE WITH NANOELECTRODES

The typical negative and positive feedback approach curve obtained with commercial CHI SECM is shown below in figure 6.5. In the experiment, a typical three electrode SECM cell was used. The x and y axis were normalized distance and normalized current respectively.

Normalized distance = $L = d/r$ where, d is distance between tip and substrate, r , is radius of electrode.

Normalized current = $I_{\text{norm}} = I/I_{\text{ss}}$ where, I_{ss} is the steady state current at infinity.

By fitting the experimental curve with the theoretical one, the exact distance between tip and the substrate was determined in SECM. Since the negative feedback approach curve was dependent on blocking of redox mediator by the insulating glass portion of the tip, it gives information about the RG (the ratio of outside electrode diameter and Pt diameter). Hence, ideally the thickness of glass surrounding the Pt portion also can be determined. In the experiment below, clean Teflon was used as insulating substrate and 2 mm Pt electrode was used as conducting substrate. The nanoelectrode was tested first by running CV for 30 min. The approaching speed of the nanoelectrode for positive feedback approach curve had to be approximately 10 times slower in comparison of negative feedback approach curve.

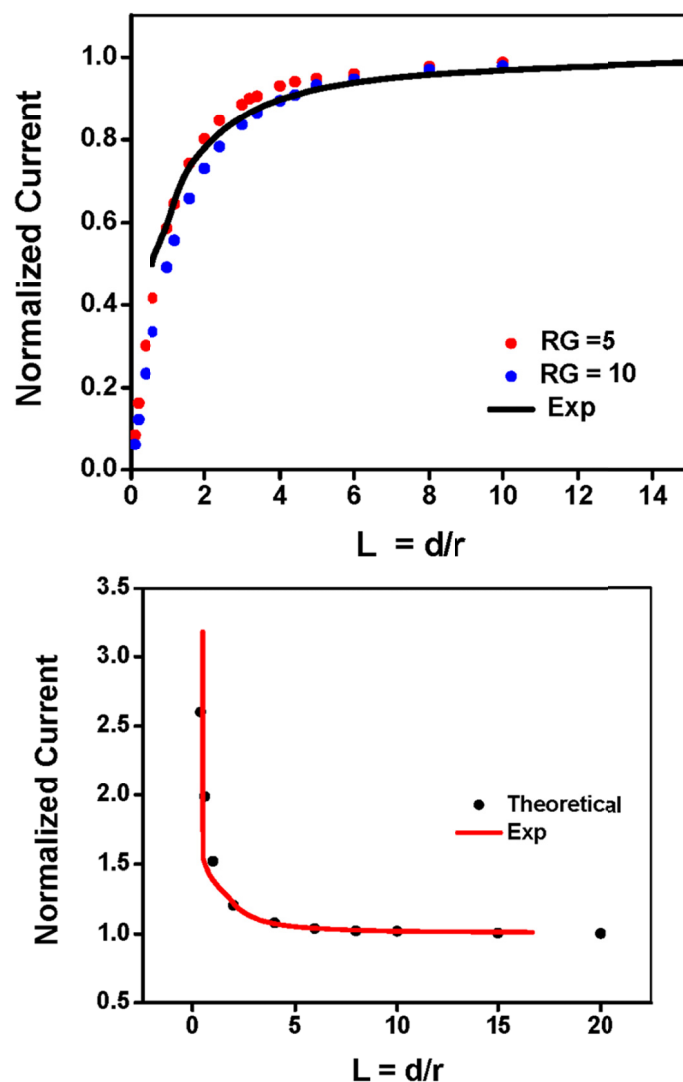


Figure 6.5: Negative and positive feedback approach curve using nanoelectrode

(Top) The negative feedback approach curve of nanoelectrode 1.3 (radius ~ 180 - 200 nm). Approach Speed: $0.05 \mu\text{m}/0.0167\text{sec}$ (Bottom) The positive feedback approach curve of nanoelectrode 1.3 (radius ~ 180 - 200 nm). Approaching speed: $0.005 \mu\text{m}/0.0167$ s or 300 nm/s. The experiment approach curve (smooth lines) was fitted with theoretical approach curve (points).

SECM IMAGING WITH NANO-ELECTRODES

Figure 6.6 and 6.7 showed the SECM image of a polycarbonate membrane of 200 nm pore size in the presence of 10 mM ferrocyanide methanol in solution. The membrane was placed on a 2 mm Pt electrode and used as a substrate on SECM stage. The nanoelectrode 1.3 of 180-200 nm radius (approx.) was used as tip for imaging at the distance of 200-300 nm away from the substrate (Figure 6.7).

In the Figure 6.8 described below, a glass nanopore was used as a substrate for electrochemical imaging with the aid of a nanotip. In brief, the nanopore was made by the Henry White group at the University of Utah as follows: At first the Pt wire was electrochemically etched and sealed in glass to make a nanoelectrode. The wire was then etched away to form nanopore. The pore is conical in shape and tapered at the top. The inside surface of the pore was then modified with 3-cyanopropyldimethylchlorosilane to make it hydrophobic. The pore was loaded with aqueous solution, containing 2 mM ferrocene methanol and 0.1 (M) Na_2SO_4 , in vacuum suction line and later assembled in SECM cell set up for imaging experiment.

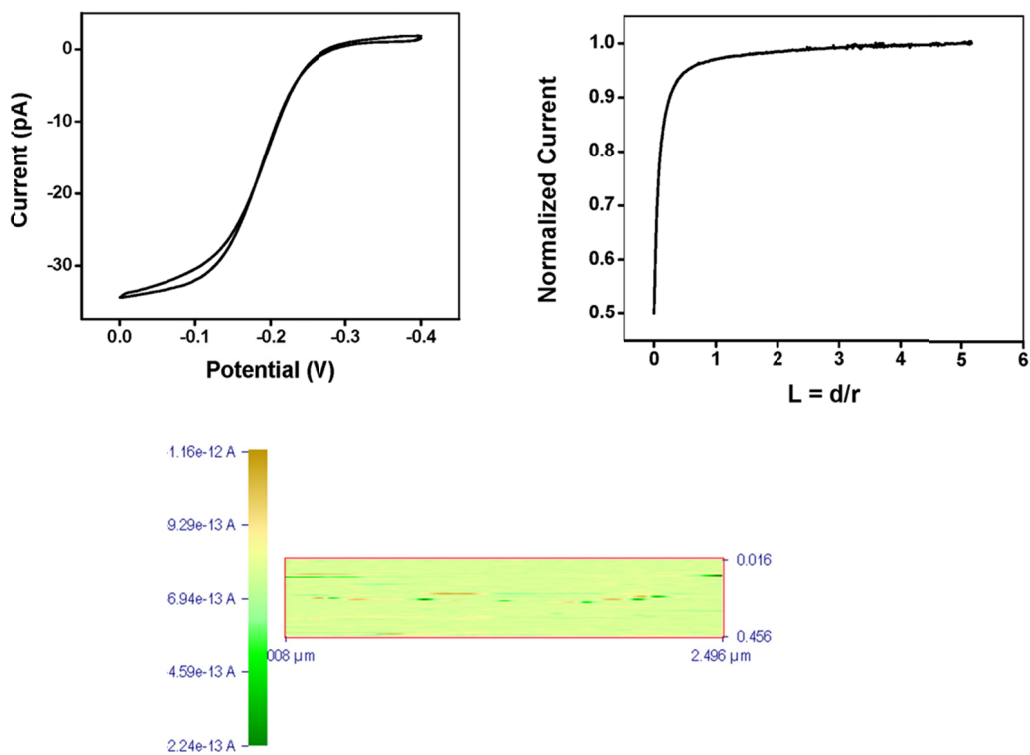


Figure 6.6: SECM image of pores of a polycarbonate membrane

(*Top Left*) CV of nanoelectrode 2.4 of radius 63 nm in presence of 2 mM ferrocene methanol and 0.1 (M) Na_2SO_4 . (*Top Right*) Negative feedback approach curve on insulating polycarbonate. (*Bottom*) Constant height SECM image when tip was held at 0V (vs. $\text{Hg}/\text{Hg}_2\text{SO}_4$) or diffusion controlled potential and substrate was at open circuit potential. Scanning Speed: 480 nm/s.

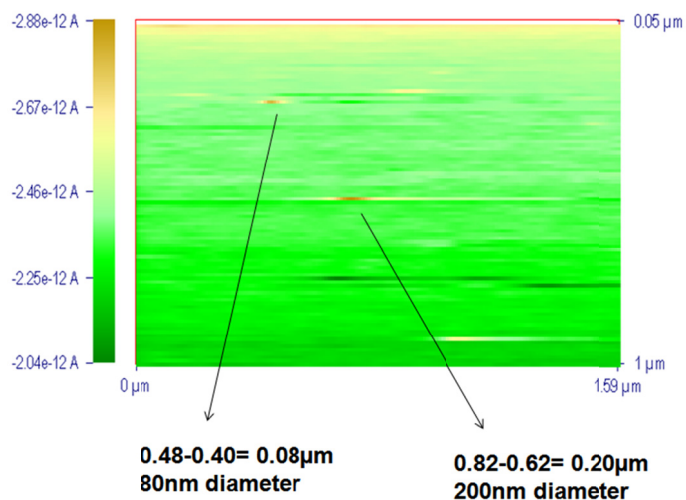


Figure 6.7: Constant height mode SECM image of 200 nm pore polycarbonate membrane placed on 2 mm Pt electrode.

Counter & reference: 0.5 mm Tungsten and Hg/Hg₂SO₄ respectively. Scanning Speed: 0.01 μm/ 0.0167 s or 600 nm/s. Tip: 0V & Substrate: open circuit potential.

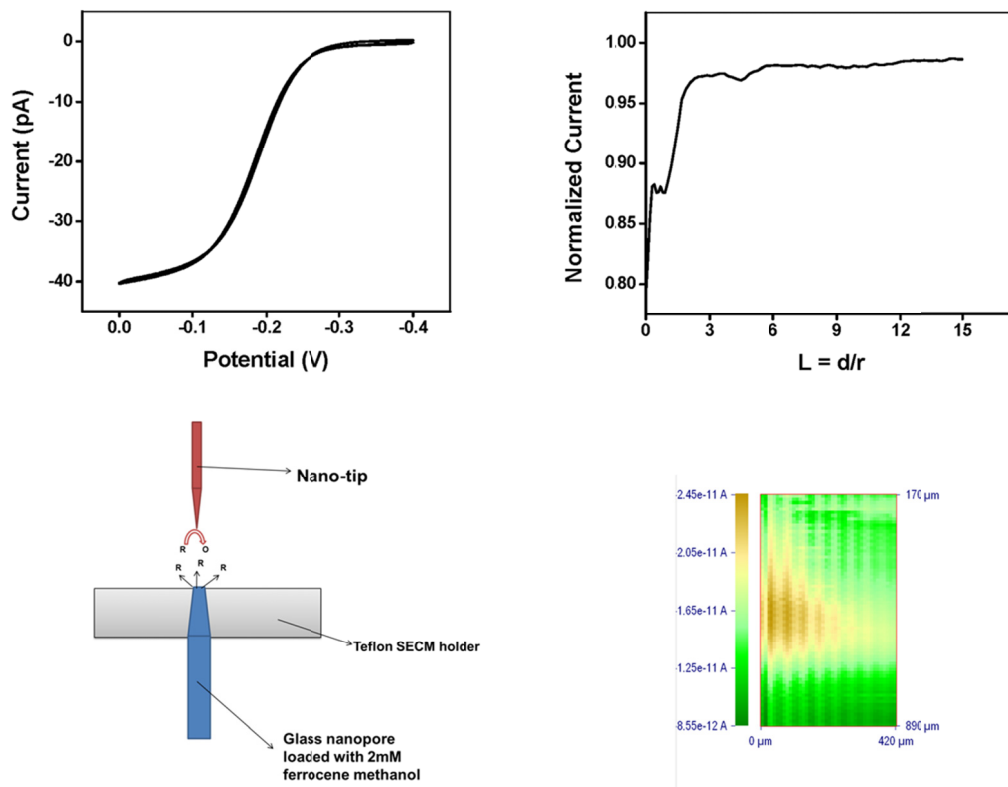


Figure 6.8: SECM image of a glass nanopore

(*Top Left*) CV of nanoelectrode 2.4 of radius 150 nm (approx.) in presence of 2 mM ferrocene methanol at bulk (*Top Right*) Negative feedback approach curve on glass Nanopore substrate. (*Bottom Left*) Constant height mode SECM image in substrate generation and tip collection mode. Tip was held at 0 V vs. Hg/Hg₂SO₄ or 0.64 V vs. NHE. (*Bottom Right*) Schematic representation of Nanopore experiment set up. The nanotip, held at 0 V, was dipped inside the solution containing only 0.1 (M) Na₂SO₄. The glass Nanopore was loaded with 2 mM ferrocene methanol & 0.1 (M) Na₂SO₄ and let the ferrocene methanol diffuse through the 1 μm pore by natural diffusion due to concentration gradient.

MAJOR CHALLENGES ASSOCIATED WITH NANO-ELECTRODES & COMMERCIAL CHI SECM

- a) One of the major problems with nanoelectrodes is cleaning the electrode surface after it accidentally touches the surface during the approach curve or becomes contaminated. Though the sulfuric acid scanning based electrochemical cleaning works well with normal cleaning of the surface it is not suitable for the cases where the electrode surface got too contaminated either by crashing or by irreversible adsorption of contaminants on the surface.

- b) For the electrodes of the order of 100 nm it is a real a technical challenge to do an approach curve on regular basis without crashing the tip on some occasions. First the response signal from the instrument to computer is not sensitive and fast enough for the tip to stop from crashing at the nm level distance. So, our proposal is as follows: moving the tip from far away to very close (~200nm) to the surface or performing the long distance approach curve by tuning fork method and then withdrawing at a 0.5-1 μm distance and then doing the short distance approach curve using SECM based technique (using very slow approach rate with piezo motor) to know the exact distance between the substrate and tip.

- c) Another major problem in SECM imaging is to fix the tilt of the substrate so that the tip doesn't touch the substrate while scanning a 100 μm X 100 μm area. In the commercial SECM it's become increasingly hard to fix the tilt in the nm range. It has become especially important when the tip-substrate distance is ~200 nm or less. The alternative would be to use constant current imaging.

d) For nano scale imaging the sensitivity is a major problem, especially when the current is in the order 10^{-12} Amp, due to the fact that the bad signal-noise ratio results in a poor quality SECM image.

Appendix A: Publications from this dissertaion

Chapter-2

Dipankar Koley and Allen J Bard (2010) Triton X-100 Concentration Effects on Membrane Permeability of a Single HeLa Cell by Scanning Electrochemical Microscopy (SECM) *Proc. Natl. Acad. Sci. U.S.A.* 107(39):16783-16787.

Chapter-3

Dipankar Koley and Allen J Bard (2011) Inhibition of the MRP1-Mediated Transport of the Menadione-Glutathione Conjugate (Thiodione) in HeLa Cells as Studied by Scanning Electrochemical Microscopy, *manuscript in preparation*.

Chapter-4

Dipankar Koley, Matthew M Ramsey, Marvin Whiteley and Allen J Bard (2011) Reduction of Iron (III) by reduced pyocyanin layer produced by *P. aeruginosa* biofilm, *manuscript in preparation*.

Chapter-5

Xuihui Liu, Matthew M Ramsey, Xiaole Chen, **Dipankar Koley**, Marvin Whiteley and Allen J Bard (2011) Real Time Mapping of a Hydrogen Peroxide Concentration Profile Across a Polymicrobial Bacterial Biofilm Using Scanning Electrochemical Microscopy (SECM) *Proc. Natl. Acad. Sci. U.S.A.* 108(7): 2668-2673.

Appendix B: List of Protocols

B.1 SUBCULTURE OF HELA CELLS

1. HeLa cell is bought from ATCC (catalog number CCL-2)
2. ATCC recommended culture medium (ATCC 30-2003) and fetal bovine serum (ATCC 30-2020) was used.
3. The medium was first divided in 50 mL of centrifuge tube inside the laminar flow bio-fumehood.
4. Then the serum was thawed at 37°C water bath and then added to centrifuge tube containing medium only solution inside bio-fumehood.
5. 5 mL of serum was added to medium only 45 mL solution to make it 50 mL solution total.
6. Thus complete culture medium with 10% fetal bovine serum was prepared. It was kept in refrigerator at 4°C for storage.
7. The big bottle of serum was divided in small 50 mL centrifuge tube because repeated thawing and freezing of serum was not good for serum quality. When serum need to be used 50 mL serum containing centrifuge tube was taken out, thawed and used as needed.
8. Before adding to cells the complete culture medium was taken out of the refrigerator and put in 37°C water bath for 10min.
9. The tubes were sprayed with 70% ethanol water mixture and then put inside bio-fumehood.
10. 2 mL complete culture medium was then added into tissue culture Petri dish.
11. ATCC shipped HeLa cells in dry ice.
12. The vial was thawed in 37°C water bath for 10 min
13. The cells were transferred to culture medium as soon as it was thawed.
14. Be very careful not to pipette too harshly as it may kill the cells.

B.2 FREEZE STORING OF HE LA CELLS

1. Culture the cells in 6 well plate Petri dish
2. Grow the cells almost 100% coverage
3. Add 500 μ L of trypsin and wait for 10mins
4. Centrifuge the cells and then wash the cells with 500 μ L of fresh medium without serum
5. Add 1000 μ L complete culture medium with serum and re-suspend the cells by pipetting
6. Add 10 μ L of DMSO to 1000 μ L of cell suspended medium
7. Pipette very gently the medium once or twice as the cell membrane are sensitive in presence of DMSO
8. Wrap the centrifuge tube cap with paraffin and put the tube inside the refrigerator at 4°C for 2 h.
9. Put the tube in freezer at -20°C for 5 h
10. Put the tube permanently inside the liquid nitrogen cooled freezer at -70°C for long-term storage.

B.3 MENADIONE-ANTIBODY SECM EXPERIMENT PROTOCOL

1. HeLa cells were cultured in full tissue cultured Petri dish until 90-100 % coverage.
2. Add 500 μ L of trypsin, wait 6-10 min; centrifuge; discard trypsin and add 500 μ L of medium only solution; re-suspend the cells; centrifuge for 5 min at 3,000 rpm; discard medium;
3. Add 2 mL of medium + serum solution and re-suspend the cells.
4. Dilute the cell numbers by adding suitable amount of medium + serum solution
5. Drop 100 μ L of medium with cells on the middle of the Petri dish.

6. Put the dish inside incubator for 16 hr to stick on the surface and multiply. Transfection worked efficiently on logarithmic phase growth or dividing cells.
7. Follow the antibody transfection protocol procedures for delivery of antibody inside the cells
8. Add 20 μL of antibody solution (stock solution from Santa Cruz Biotechnology) in centrifuge tube and then add 4 μL of lipodin-Ab solution and mix them thoroughly. Wait for 15 min. All these procedures are done inside fume hood.
9. During this 15 min, wash the cells by replacing the complete culture medium with 120 μL of medium only solution
10. After 15 min, add 100 μL of medium only solution to the antibody-lipodin complex solution; mix them thoroughly and then immediately add to the cells.
11. The dish was then put back to the incubator for 5 to 6 h.
12. Take out the dish from incubator and add 400 μL of buffer to wash twice.
13. Put the dish on the SECM stage and set up the reference electrode and counter electrode. Attach the tip with SECM holder.
14. Add 400 μL of buffer only solution for 1 h at room temperature.
15. After 1 h, replace the buffer with 400 μL of ferrocene methanol solution
16. Perform negative feedback approach curve over the cells. Fix the height at 80 μm .
17. Pull up the tip for 3,000 μm
18. Replace the solution with buffer solution. Wash the cells thrice and check any presence of ferrocene methanol in the solution by running CV.
19. Pull up the tip at 3,000 μm distance
20. Add 500 μL of menadione solution as slowly as possible
21. Bring back the tip at 80 μm away from the surface

22. Run the CV from -0.65 V to +0.65 V starting from 0 V and cycle is 3

23. Record the CV at every 2 min until half an hour time period

Materials

1. HeLa Cells (ATCC-CCL2)
2. Petri dish (BD Primaria, Tissue culture dish, 35 mm dia × 10 mm H, cat. 353801)
3. Medium (ATCC, EMEM, 30-2003)
4. Serum (ATCC 30-2020)
5. Trypsin (Hyclone SH3004201)
6. Antibody (Santa Cruz biotechnology, QCRL-4, sc-18874);
200 µg of IgG₁ in 1mL of PBS
7. Antibody Transfecting Agent (Abbiotec, Lipodin-Ab)

References

Chapter-1

- ¹ Adams KL, Puchades M, Ewing AG (2008) In Vitro Electrochemistry of Biological Systems. *Annu. Rev. Anal. Chem. (Palo Alto, Calif.)* 1:329.
- ² Adams RN (1976) Probing brain chemistry with electroanalytical techniques. *Anal. Chem.* 48:1126A-1138A.
- ³ Feng JX, Brazell M, Renner K, Kasser R, Adams RN (1987) Electrochemical pretreatment of carbon fibers for in vivo electrochemistry: effects on sensitivity and response time. *Anal. Chem.* 59:1863-1867.
- ⁴ Wightman RM (1991) Temporally Resolved Catecholamine Spikes Correspond to Single Vesicle Release from Individual Chromaffin Cells. *Proc. Natl. Acad. Sci. U.S.A.* 88:10754-10758.
- ⁵ Montenegro, M.I., Queir'os, M.A., Daschbach, J.L. (Eds.), (1991) *Biological Systems in Microelectrodes: Theory and Applications*. (Kluwer Academic Publishing, Dordrecht) pp. 453–462.
- ⁶ Bard AJ ed. (2007) *Encyclopedia of Electrochemistry* (Wiley-VCH Verlag GmbH & Co. KGaA, Weinheim, Germany).
- ⁷ Cooper, J.M., Jung, S.-K., 2001. In: Bard, A.J., Stratman, M., Wilson, G.S. (Eds.), *Encyclopedia of Electrochemistry*, vol. 9. Wiley-VCH, pp. 31–49.
- ⁸ Gao N, Zhao M, Zhang X, Jin W (2006) Measurement of enzyme activity in single cells by voltammetry using a microcell with a positionable dual electrode. *Anal. Chem.* 78:231-8.
- ⁹ Cannon DM, Winograd N, Ewing AG (2000) Quantitative chemical analysis of single cells. *Annu. Rev. Biophys.* 29:239-63.
- ¹⁰ Bard AJ, Mirkin MV, eds. (2001) *Scanning Electrochemical Microscopy* (Merrel Dekker, New York).

- ¹¹ Bard AJ, Denuault G, Lee C, Mandler D, Wipf DO (1990) Scanning electrochemical microscopy - a new technique for the characterization and modification of surfaces. *Acc. Chem. Res.* 23:357-363.
- ¹² Amemiya S, Guo J, Xiong H, Gross D a (2006) Biological applications of scanning electrochemical microscopy: chemical imaging of single living cells and beyond. *Anal. Bioanal.Chem.* 386:458-71.
- ¹³ Amemiya S, Bard AJ, Fan F-RF, Mirkin MV, Unwin PR (2008) Scanning Electrochemical Microscopy. *Annu. Rev. Anal. Chem.* (2008) 1:95-131.
- ¹⁴ Bard AJ, Li X, Zhan W (2006) Chemically imaging living cells by scanning electrochemical microscopy. *Biosens. Bioelectron.* 22:461-72.
- ¹⁵ Mauzeroll J, Bard AJ (2004) Scanning electrochemical microscopy of menadione-glutathione conjugate export from yeast cells. *Proc. Natl. Acad. Sci. U.S.A.* 101:7862-7.
- ¹⁶ Mauzeroll J, Bard AJ, Owhadian O, Monks TJ (2004) Menadione metabolism to thiodione in hepatoblastoma by scanning electrochemical microscopy. *Proc. Natl. Acad. Sci. U.S.A.* 101:17582-7.
- ¹⁷ Lu H, Gratzl M (1999) Monitoring drug efflux from sensitive and multidrug-resistant single cancer cells with microvoltammetry. *Anal. Chem.* 71:2821-30.
- ¹⁸ Holt KB, Bard AJ (2005) Interaction of silver(I) ions with the respiratory chain of *Escherichia coli*: an electrochemical and scanning electrochemical microscopy study of the antimicrobial mechanism of micromolar Ag⁺. *Biochemistry* 44:13214-23.
- ¹⁹ Zhan D, Li X, Zhan W, Fan F-RF, Bard AJ (2007) Scanning electrochemical microscopy. 58. Application of a micropipet-supported ITIES tip to detect Ag⁺ and study its effect on fibroblast cells. *Anal. Chem.* 79:5225-31.

- ²⁰ Zhan D, Fan F-RF, Bard AJ (2008) The Kv channel blocker 4-aminopyridine enhances Ag⁺ uptake: a scanning electrochemical microscopy study of single living cells. *Proc. Natl. Acad. Sci. U.S.A.* 105:12118-22.
- ²¹ Li X, Bard AJ (2009) Scanning electrochemical microscopy of HeLa cells – Effects of ferrocene methanol and silver ion. *J. Electroanal. Chem.* 628:35-42.
- ²² Sun P et al. (2008) Nanoelectrochemistry of mammalian cells. *Proc. Natl. Acad. Sci. U.S.A.* 105:443-8.
- ²³ Gonsalves M et al. (2000) Scanning electrochemical microscopy as a local probe of oxygen permeability in cartilage. *Biophys. J.* 78:1578-88.
- ²⁴ Liu B, Rotenberg SA, Mirkin MV (2000) Scanning electrochemical microscopy of living cells: different redox activities of nonmetastatic and metastatic human breast cells. *Proc. Natl. Acad. Sci. U.S.A.* 97:9855-60.
- ²⁵ Kaya T, Torisawa Y-suke, Oyamatsu D, Nishizawa M, Matsue T (2003) Monitoring the cellular activity of a cultured single cell by scanning electrochemical microscopy (SECM). A comparison with fluorescence viability monitoring. *Biosens. Bioelectron.* 18:1379-83.
- ²⁶ Bard, A. J. & Faulkner, L. R. (2001) *Electrochemical Methods* (Wiley, New York), 2nd Ed., p. 294-296.

Chapter-2

- ¹ Gennuso F, et al. (2004) Bilirubin protects astrocytes from its own toxicity by inducing up-regulation and translocation of multidrug resistance-associated protein 1 (mrp1). *Proc Natl Acad Sci USA* 101:2470–2475.
- ² Rajagopal A, Pant AC, Simon SM, Chen Y (2002) In Vivo analysis of human multidrug resistance protein (MRP1) activity using transient expression of fluorescently Tagged MRP1. *Cancer Res* 62:391–396.
- ³ Hipfner DR, Gauldie SD, Deeley RG, Cole SPC (1994) Detection of the Mr 190,000 multidrug resistance protein, MRP, with monoclonal antibodies. *Cancer Res* 54:5788–5792.

- ⁴ Borner MM, et al. (1994) The detergent TX100 induces a death pattern in human carcinoma cell lines that resembles cytotoxic lymphocyte-induced apoptosis. *FEBS Lett* 353:129–132.
- ⁵ Benoit J, Cormier M, Wepierre J (1988) Comparative effects of four surfactants on growth, contraction and adhesion of cultured human fibroblasts. *Cell Biol Toxicol* 4(1):111–122.
- ⁶ Dayeh VR, Chow SL, Schirmer K, Lynn DH, Bols NC (2004) Evaluating the toxicity of TX100 to protozoan, fish, and mammalian cells using fluorescent dyes as indicators of cell viability. *Ecotox Environ Safe* 57:375–382.
- ⁷ Laouar L, Lowe KC, Mulligan BJ (1996) Yeast response to nonionic surfactants. *Enzyme Microb Tech* 18:433–438.
- ⁸ Barnett SM, Dracheva S, Hendler RW, Levin IW (1996) Lipid-induced conformational change of an integral membrane protein: An infrared spectroscopic study of the effects of TX100 treatment on the purple membrane of *Halobacterium halobium* ET1001. *Biochemistry* 35:4558–4567.
- ⁹ Aránzazu MP, Ostolaza H, Goñi FM, Barberá-Guillem E (1990) Surfactant-induced cell toxicity and cell lysis a study using B16 melanoma cells. *Biochem Pharmacol* 40(6):1323–1328.
- ¹⁰ Benoit J, Cormier M, Wepierre J (1988) Comparative effects of four surfactants on growth, contraction and adhesion of cultured human fibroblasts. *Cell Biol Toxicol* 4(1):111–122.
- ¹¹ Maire ML, Champeil P, Moller JV (2000) Interaction of membrane proteins and lipids with solubilizing detergents. *Biochim Biophys Acta* 1508:86–111.
- ¹² Fontaine P, et al. (2007) Unexpected stability of phospholipid langmuir monolayers deposited on TX100 aqueous solutions. *Langmuir* 23:12959–12965.
- ¹³ Nyholm T, Slotte JP (2001) Comparison of TX100 penetration into phosphatidylcholine and sphingomyelin mono- and bilayers. *Langmuir* 17:4724–4730.

- ¹⁴ London E, Brown DA (2000) Insolubility of lipids in TX100: Physical origin and relationship to sphingolipid/cholesterol membrane domains (rafts). *Biochim Biophys Acta* 1508:182–195.
- ¹⁵ Bard AJ, Mirkin MV, eds. (2001) Scanning Electrochemical Microscopy (Mercel Dekker, New York).
- ¹⁶ Li X, Bard AJ (2009) Scanning electrochemical microscopy of HeLa cells—Effects of ferrocene methanol and silver ion. *J Electroanal Chem* 628:35–42.
- ¹⁷ Guo J, Amemiya S (2005) Permeability of the nuclear envelope at isolated *Xenopus* Oocyte nuclei studied by scanning electrochemical microscopy. *Anal Chem* 77(7):2147–2156.
- ¹⁸ Hirano Y, et al. (2008) Construction of time-lapse scanning electrochemical microscopy with temperature control and its applications to evaluate the preservation effects of antifreeze proteins on living cells. *Anal Chem* 80:9349–9354.
- ¹⁹ Gonsalves M, Macpherson JV, O’Hare D, Winlove CP, Unwin PR (2000) High resolution imaging of the distribution and permeability of methyl viologen dication in bovine articular cartilage using scanning electrochemical microscopy. *BBA-Gen Subjects* 1524(1):66–74.
- ²⁰ Gonsalves M, et al. (2000) Scanning electrochemical microscopy as a local probe of oxygen permeability in cartilage. *Biophys J* 78:1578–1588.
- ²¹ London E, Brown DA (2000) Insolubility of lipids in TX100: Physical origin and relationship to sphingolipid/cholesterol membrane domains (rafts). *Biochim Biophys Acta* 1508:182–195.
- ²² Lanyi JK (1973) Influence of electron transport on the interaction between membrane lipids and TX100 in halobacterium cutirubrum. *Biochemistry* 12(7):1433–1438.
- ²³ Maire ML, Champeil P, Moller JV (2000) Interaction of membrane proteins and lipids with solubilizing detergents. *Biochim Biophys Acta* 1508:86–111.

- ²⁴ Fontaine P, et al. (2007) Unexpected stability of phospholipid langmuir monolayers deposited on TX100 aqueous solutions. *Langmuir* 23:12959–12965.
- ²⁵ Troiano GC, Tung L, Sharma V, Stebe JK (1998) The reduction in electroporation voltages by the addition of a surfactant to planar lipid bilayers. *Biophys J* 75:880–888.
- ²⁶ Sigma-Aldrich Co (1999) TX100, T9284 product information sheet (Sigma-Aldrich, St. Louis).
- ²⁷ Rafat M, et al. (2008) Association (micellization) and partitioning of aglycon triterpenoids. *J Colloid Interface Sci* 325(2):324–330.
- ²⁸ Morandat S, Kirat EK (2006) Membrane resistance to TX100 explored by real time atomic force microscopy. *Langmuir* 22:5786–5791.
- ²⁹ Paternostre MT, Roux M, Rigaud JL (1988) Mechanisms of membrane protein insertion into liposomes during reconstitution procedures involving the use of detergents. 1. Solubilization of large unilamellar liposomes (prepared by reverse-phase evaporation) by TX100, Octyl Glucoside, and Sodium Cholate. *Biochemistry* 27:2668–2677.
- ³⁰ Rigaud JL, Paternostre MT, Bluzat A (1988) Mechanisms of membrane protein insertion into liposomes during reconstitution procedures involving the use of detergents. 2. Incorporation of the light-driven proton pump bacteriorhodopsin. *Biochemistry* 27:2677–2688.
- ³¹ Nyholm T, Slotte JP (2001) Comparison of TX100 penetration into phosphatidylcholine and sphingomyelin mono- and bilayers. *Langmuir* 17:4724–4730.

Chapter-3

- ¹ Higgins CF (2007) Multiple molecular mechanism for multidrug resistance transporters. *Nature* 446:749-757.
- ² Hooijberg JH, et al. (2000) The effect of glutathione on the ATPase activity of MRP 1 in its natural membranes. *FEBS Lett* 469:47-51.

- ³ Paul S, Breuninger LM, Tew KD, Shen H, Kruh GD (1996) ATP-dependent uptake of natural product cytotoxic drugs by membrane vesicles establishes MRP as a broad specificity transporter. *Proc Natl Acad Sci USA* 93:6929-6934.
- ⁴ Seung S, Lee JY, Lee MY, Park JS, Chung JH (1998) The relative importance of oxidative stress versus arylation in the mechanism of quinone –induced cytotoxicity to platelets. *Chem Biol Interact* 113:133-144.
- ⁵ Hultberg B, Anderson A, Isaksson A (1999) Thiol and redox reactive agents exert different effects on glutathione metabolism in HeLa cells culture. *Clin Chim Acta*, 283:21-32.
- ⁶ Monks TJ, Lau SS (1997) Biological reactivity of polyphenolic-glutathione conjugates. *Chem Res Toxicol* 10:1296-1313
- ⁷ Miller MG, Rodgers A, Cohen GM (1986) Mechanisms of toxicity of naphthoquinones to isolated hepatocytes. *Biochem Pharmacol* 35:1177-1184.
- ⁸ Eaton DL, Bammler TK (1999) Concise review of the glutathione S-Transferases and their Significance to Toxicology. *Toxicol Sci* 49:156-164.
- ⁹ Mueller CFH, et al. (2005) The role of multidrug resistance protein-1 in modulation of endothelial cell oxidative stress. *Circ Res* 97:637-644.
- ¹⁰ Roelofsen H, Hooiveld GJEJ, Koning H, Havinga R, Jansen PLM (1999) Glutathione S-conjugate transport in hepatocytes entering the cell cycle is preserved by a switch in expression from the apical MRP2 to the basolateral MRP1 transporting protein. *J Cell Sci* 112:1395-1404.
- ¹¹ Zaman GJR, et al. (1995) Role of glutathione in the export of compounds from cells by the multidrug resistance-associated protein. *Proc Natl Acad Sci USA* 92:7690-7694.
- ¹² Muller M, et al. (1994) Overexpression of the gene encoding the multidrug resistance-associated protein results in increased ATP-dependent glutathione S-conjugate transport. *Proc Natl Acad Sci USA* 91:13033-13037.
- ¹³ Renes J, Vries EGE, Nienhuis EF, Jansen PLM, Muller M (1999) ATP-and glutathione-dependent transport of chemotherapeutic drugs by the multidrug resistance protein MRP1. *Br J Pharmacol* 126:681-688.
- ¹⁴ Hipfner DR, Deeley RG, Cole SPC (1999) Structural, mechanistic and clinical aspects of MRP1. *BBA* 1461:359-376.
- ¹⁵ Jedlitschky G, et al. (1996) Transport of glutathione, glucuronate and sulfate conjugates by the MRP gene-encoded conjugate export pump. *Cancer Res* 56:988-994.
- ¹⁶ I. Leier, et al. (1994) The MRP gene encodes an ATP-dependent export pump for Leukotriene C4 and structurally related conjugates. *J Biol Chem* 269:27807-27810.
- ¹⁷ Shen H, et al. (1996) Cellular and in-vitro transport of glutathione conjugate by MRP. *Biochemistry* 35:5719-5725.

- ¹⁸ Karla PK, Pal D, Quinn T, Mitra AK (2007) Molecular evidence and functional expression of a novel drug efflux pump (ABCC2) in human corneal epithelium and rabbit cornea and its role in ocular drug efflux. *Int J Pharm* 336:12-21.
- ¹⁹ Tabas LB, Dantzig AH (2002) A high-throughput assay for measurement of multidrug resistance protein-mediated transport of leukotriene C4 into membrane vesicles. *Anal Biochem* 310:61-66.
- ²⁰ Decory HH, Dumas KMP, Sheu SS, Federoff HJ, Anders MW (2001) Efflux of glutathione conjugate of monochlorobimane from striatal and cortical neurons. *Drug Metab Dispos* 29:1256-1262.
- ²¹ Tabas LB, Dantzig AH (2002) A high-throughput assay for measurement of multidrug resistance protein-mediated transport of leukotriene C4 into membrane vesicles. *Anal Biochem* 310:61-66.
- ²² Rigato I, Pascolo L, Ferneti C, Ostrow JJD, Tiribelli C (2004) The human multidrug-resistance-associated protein MRP1 mediates ATP-dependent transport of unconjugated bilirubin. *Biochem J* 383:335-341.
- ²³ Gekeler V, Ise W, Sanders KH, Ulrich WR, Beck J (1995) The Leukotriene LTD4 receptor antagonist MK571 specifically modulates MRP associated multidrug resistance. *Biochem Biophys Res Commun* 208:345-352.
- ²⁴ Gennuso F, et al. (2004) Bilirubin protects astrocytes from its own toxicity by inducing up-regulation and translocation of multidrug resistance-associated protein 1 (Mrp1). *Proc Natl Acad Sci USA* 101:2470-2475.
- ²⁵ Salerno M, Loechariyakul P, Saengkhae C, Suillerot AG (2004) Relation between the ability of some compounds to modulate the MRP1-mediated efflux of glutathione and to inhibit the MRP1-mediated efflux of daunorubicin. *Biochem Pharmacol* 68:2159-2165.
- ²⁶ Jeong EJ, Jia X, Hu M (2005) Disposition of formononetin via enteric recycling: Metabolism and excretion in mouse intestinal perfusion and caco-2 cell models. *Mol Pharmaceutics* 2:319-328.
- ²⁷ Hipfner DR, Gaudie SD, Deeley RG, Cole SPC (1994) Detection of the Mr 190,000 Multidrug resistance protein, MRP, with monoclonal antibodies. *Cancer Res* 54:5788-5792.
- ²⁸ Hipfner DR, Almquist KC, Stride BD, Deeley RG, Cole SPC (1996) Location of a protease-hypersensitive region in the multidrug resistance protein (MRP) by mapping of the epitope of MRP-specific monoclonal antibody QCRL-1. *Cancer Res* 56:3307-3314.
- ²⁹ Hipfner DR, Mao Q, Qui W, Leslie EM, Gao M, Deeley RG, Cole SPC (1999) Monoclonal antibodies that inhibit the transport function of the 190-kDa multidrug resistance protein, MRP. *J Biol Chem* 274:15420-15426.
- ³⁰ Hipfner DR, Deeley RG, Cole SPC (1999) Structural mechanistic and clinical aspects of MRP1. *Biochim Biophys Acta* 1461:359-376.

- ³¹ Scheffer GL et. al. (2000) Specific detection of multidrug resistance proteins MRP1, MRP2, MRP3, MRP5, and MDR3 P-Glycoprotein with a panel of monoclonal antibodies. *Cancer Res* 60:5269-5277.
- ³² Loe DW, Almquist KC, Deeley RG, Cole SPC (1996) Multidrug resistance protein (MRP)-mediated transport of leukotriene C4 and chemotherapeutic agents in membrane vesicles. *J Biol Chem* 271:9675-9682.
- ³³ Loe DW, Deeley RG, Cole SPC (1998) Characterization of vincristine transport by the Mr 190,000 multidrug resistance protein (MRP): Evidence for cotransport with reduced glutathione. *Cancer Res* 58:5130-5136.
- ³⁴ Hipfner DR, Gao M, Scheffer, Scheper RJ, Deeley RG, Cole SPC (1998) Epitope mapping of monoclonal antibodies specific for the 190-kDa multidrug resistance protein (MRP). *Br J Pharmacol* 78:1134-1140.
- ³⁵ Cole SPC and Deeley RG (1998) Multidrug resistance mediated by the ATP-binding cassette transporter protein MRP. *BioEssays* 20:931-940.
- ³⁶ Mauzeroll J, Bard AJ (2004) Scanning electrochemical microscopy of menadione-glutathione conjugate export from yeast cells. *Proc Natl Acad Sci USA* 101:7862-7867.
- ³⁷ Mauzeroll J, Bard AJ, Owhadian O, Monks TJ (2004) Menadione metabolism to thiodione in hepatoblastoma by scanning electrochemical microscopy. *Proc Natl Acad Sci USA* 101:17582-17587.
- ³⁸ Bard AJ, Mirkin MV, Eds., *Scanning Electrochemical Microscopy*; MerceL Dekker, New York, 2001 p 75.

Chapter-4

- ¹ Miller MB, Bassler BL (2001) Quorum sensing in bacteria. *Annual review of microbiology* 55:165-99.
- ² (a) Taga, M. E., & Bassler, B. L. (2003) Chemical communication among bacteria. *Proc. Natl. Acad. Sci. U.S.A.* 14549-54.
- (b) Nealson KH, Platt T, Hastings JW (1970) Cellular control of the synthesis and activity of the bacterial luminescent system. *J Bacteriol* 104:313-22. (1st paper about quorum sensing in 1970, dealt with light producing bacteria that live inside Squid, 1st time it was characterized but the signal itself was not purified.)
- (c) Pearson JP, Passador L, Iglewski BH, Greenberg EP (1995) A second N-acylhomoserine lactone signal produced by *Pseudomonas aeruginosa*. *Proc. Natl.*

- Acad. Sci. U.S.A.* 92:1490-4. (1st paper describing the likelihood of multiple types of QS functioning in *P. aeruginosa*)
- (d) Passador L, Cook JM, Gambello MJ, Rust L, Iglewski BH (1993) Expression of *Pseudomonas aeruginosa* virulence genes requires cell-to-cell communication. *Science (New York, N.Y.)* 260:1127-30. (1st characterization of a QS signal in *P. aeruginosa*)
- ³ Schaechter, M. (2009) *Encyclopedia of microbiology*. Amsterdam ; Boston, Elsevier/Academic Press.
- ⁴ Banin, E., M. L. Vasil, et al. (2005) Iron and *Pseudomonas aeruginosa* biofilm formation. *Proc. Natl. Acad. Sci. U.S.A.* 102(31): 11076-81.
- ⁵ Price-Whelan, A., L. E. Dietrich, et al. (2007) Pyocyanin alters redox homeostasis and carbon flux through central metabolic pathways in *Pseudomonas aeruginosa* PA14. *J Bacteriol* 189(17): 6372-81.
- ⁶ West, S. a, Diggle, S. P., Buckling, A., Gardner, A., & Griffin, A. S. (2007) The Social Lives of Microbes. *Annu. Rev. Ecol. Evol. Syst.* 38(1), 53-77.
- ⁷ Ma L et al. (2009) Assembly and development of the *Pseudomonas aeruginosa* biofilm matrix. *PLoS pathogens* 5:e1000354.
- ⁸ Price-Whelan A, Dietrich LEP, Newman DK (2006) Rethinking “secondary” metabolism: physiological roles for phenazine antibiotics. *Nat. Chem. Biol.* 2:71-8.
- ⁹ Dietrich LEP, Price-Whelan A, Petersen A, Whiteley M, Newman DK (2006) The phenazine pyocyanin is a terminal signalling factor in the quorum sensing network of *Pseudomonas aeruginosa*. *Mol. Microbiol.* 61:1308-21.
- ¹⁰ Pierson LS, Pierson EA (2010) Metabolism and function of phenazines in bacteria: impacts on the behavior of bacteria in the environment and biotechnological processes. *Applied microbiology and biotechnology* 86:1659-70.

- ¹¹ Mentel M et al. (2009) Of two make one: the biosynthesis of phenazines. *Chembiochem : a European journal of chemical biology* 10:2295-304.
- ¹² Hassan, H. M. and I. Fridovich (1980) Mechanism of the antibiotic action pyocyanine. *J Bacteriol* 141(1): 156-63.
- ¹³ Fordos, M.-J. (1860) Recherches sur la matiere colorante des suppurations bleues: pyocyanine." *Comptes rendus hebdomadaires des séances del'Académie des sciences* 51: 215-217.
- ¹⁴ Newman, D. K. and R. Kolter (2000) A role for excreted quinones in extracellular electron transfer. *Nature* 405(6782): 94-7.
- ¹⁵ Yun Wang and Dianne K. Newman (2008) Redox Reactions of Phenazine Antibiotics with Ferric (Hydr)oxides and Molecular Oxygen. *Environ. Sci. Technol.* 42 (7), 2380-2386.
- ¹⁶ Cox, C. D. (1986) Role of pyocyanin in the acquisition of iron from transferrin. *Infect Immun* 52(1): 263-70.
- ¹⁷ Sokol, P. A. and D. E. Woods (1984) Relationship of iron and extracellular virulence factors to Pseudomonas aeruginosa lung infections. *J Med Microbiol* 18(1): 125-33.
- ¹⁸ Bearden, S. W. and R. D. Perry (1999) The Yfe system of Yersinia pestis transports iron and manganese and is required for full virulence of plague. *Mol Microbiol* 32(2): 403-14.
- ¹⁹ Velayudhan, J., N. J. Hughes, et al. (2000) Iron acquisition and virulence in Helicobacter pylori: a major role for FeoB, a high-affinity ferrous iron transporter. *Mol Microbiol* 37(2): 274-86.
- ²⁰ Mashburn, L. M., A. M. Jett, et al. (2005) Staphylococcus aureus serves as an iron source for Pseudomonas aeruginosa during in vivo coculture. *J Bacteriol* 187(2): 554-66.
- ²¹ Huse H, Whiteley M (2011) 4-Quinolones: Smart Phones of the Microbial World. *Chem. Rev.* 111:152-9.

- ²² Hense B a et al. (2007) Does efficiency sensing unify diffusion and quorum sensing? *Nat. Rev. Microbiol.* 5:230-9.
- ²³ Bukelman O et al. (2009) Electrochemical analysis of quorum sensing inhibition. *Chem. Commun. (Cambridge, England)*:2836-8.
- ²⁴ Waters CM, Bassler BL (2005) Quorum sensing: cell-to-cell communication in bacteria. *Annual review of cell and developmental biology* 21:319-46.
- ²⁵ Whiteley, M., M. G. Banger, et al. (2001) Gene expression in *Pseudomonas aeruginosa* biofilms. *Nature* 413(6858): 860-4.
- ²⁶ Dietrich, L. E., A. Price-Whelan, et al. (2006) The phenazine pyocyanin is a terminal signalling factor in the quorum sensing network of *Pseudomonas aeruginosa*. *Mol Microbiol* 61(5): 1308-21.
- ²⁷ Liberati, N. T., J. M. Urbach, et al. (2006). An ordered, nonredundant library of *Pseudomonas aeruginosa* strain PA14 transposon insertion mutants. *Proc. Natl. Acad. Sci. U.S.A.* 103(8): 2833-8.
- ²⁸ Connell, J. L., A. K. Wessel, et al. (2010) Probing prokaryotic social behaviors with bacterial "lobster traps". *MBio* 1(4).
- ²⁹ Viollier, E., P. W. Inglett, et al. (2000) The ferrozine method revisited: Fe(II)/Fe(III) determination in natural waters. *Appl. Geochem.* 15(6): 785-790.
- ³⁰ Bard AJ, Mirkin MV, Eds. (2001) *Scanning Electrochemical Microscopy* (Merzel Dekker, New York).
- ³¹ Palmer, K. L., S. A. Brown, et al. (2007) Membrane-bound nitrate reductase is required for anaerobic growth in cystic fibrosis sputum. *J Bacteriol* 189(12): 4449-55.
- ³² Price-Whelan, A. (2009) Physiology and mechanisms of pyocyanin reduction in *Pseudomonas aeruginosa*. Biology. Pasadena, CA, California Institute of Technology. Ph.D.

- ³³ Wang, Y., J. C. Wilks, et al. (2011) Phenazine-1-carboxylic acid promotes bacterial biofilm development via ferrous iron acquisition. *J Bacteriol* 193(14): 3606-3617.
- ³⁴ Hassan HM & Fridovich I (1980) Mechanism of the antibiotic action pyocyanine. *J Bacteriol* 141(1):156-163.
- ³⁵ Britigan BE, et al. (1992) Interaction of the *Pseudomonas aeruginosa* secretory products pyocyanin and pyochelin generates hydroxyl radical and causes synergistic damage to endothelial cells. Implications for *Pseudomonas*-associated tissue injury. *J Clin Invest* 90(6):2187-2196.
- ³⁶ Ran H, Hassett DJ, & Lau GW (2003) Human targets of *Pseudomonas aeruginosa* pyocyanin. *Proc Natl Acad Sci U S A* 100(24):14315-14320.

Chapter-5

- ¹ Barnard JP, Stinson MW (1999) Influence of environmental conditions on hydrogen peroxide formation by *Streptococcus gordonii*. *Infect Immun* 67:6558–6564.
- ² De Stoppelaar JD, et al. (1969) The relationship between extracellular polysaccharide-producing streptococci and smooth surface caries in 13-year-old children. *Caries Res* 3:190–199.
- ³ Kreth J, et al. (2008) Streptococcal antagonism in oral biofilms: *Streptococcus sanguinis* and *Streptococcus gordonii* interference with *Streptococcus mutans*. *J Bacteriol* 190:4632–4640.
- ⁴ Ramsey MM, Whiteley M (2009) Polymicrobial interactions stimulate resistance to host innate immunity through metabolite perception. *Proc Natl Acad Sci USA* 106:1578–1583.
- ⁵ Brown SA, Whiteley M (2007) A novel exclusion mechanism for carbon resource partitioning in *Aggregatibacter actinomycetemcomitans*. *J Bacteriol* 189:6407–6414.
- ⁶ Thomson VJ, et al. (1999) Direct selection of IS903 transposon insertions by use of a broad-host-range vector: Isolation of catalase-deficient mutants of *Actinobacillus actinomycetemcomitans*. *J Bacteriol* 181:7298–307.

- ⁷ Jakubovics NS, Gill SR, Vickerman MM, Kolenbrander PE (2008) Role of hydrogen peroxide in competition and cooperation between *Streptococcus gordonii* and *Actinomyces naeslundii*. *FEMS Microbiol Ecol* 66:637–644.
- ⁸ Mendoza AG, Liébana J, Castillo AM, de la Higuera A, Piédrola G (1993) Evaluation of the capacity of oral streptococci to produce hydrogen peroxide. *J Med Microbiol* 39:434–439.
- ⁹ Seki M, Iida K, Saito M, Nakayama H, Yoshida S (2004) Hydrogen peroxide production in *Streptococcus pyogenes*: Involvement of lactate oxidase and coupling with aerobic utilization of lactate. *J Bacteriol* 186:2046–2051.
- ¹⁰ Kreth J, Merritt J, Shi W, Qi F (2005) Competition and coexistence between *Streptococcus mutans* and *Streptococcus sanguinis* in the dental biofilm. *J Bacteriol* 187:7193–7203.
- ¹¹ Bard AJ, Mirkin MV, eds. (2001) *Scanning Electrochemical Microscopy* (Marcel Dekker, New York), pp 1–15.
- ¹² Wang X, Yang T, Feng Y, Jiao K, Li G (2009) A novel hydrogen peroxide biosensor based on the synergistic effect of gold-platinum alloy nanoparticles/polyaniline nanotube/chitosan nanocomposite membrane. *Electroanal* 21:819–825.
- ¹³ Mao L, Osborne PG, Yamamoto K, Kato T (2002) Continuous on-line measurement of cerebral hydrogen peroxide using enzyme-modified ring-disk plastic carbon film electrode. *Anal Chem* 74:3684–3689.
- ¹⁴ Liu X, Zweier LJ (2001) A real-time electrochemical technique for measurement of cellular hydrogen peroxide generation and consumption: Evaluation in human polymorphonuclear leukocytes. *Free Radical Biol Med* 31:894–901.
- ¹⁵ Horrocks BR, Schmidtke D, Heller A, Bard AJ (1993) Scanning electrochemical microscopy. 24. Enzyme ultramicroelectrodes for the measurement of hydrogenat surfaces. *Anal Chem* 65:3605–3614.
- ¹⁶ Wittstock G, Schuhmann W (1997) Formation and imaging of microscopic enzymatically active spots on an alkanethiolate covered gold electrode by scanning electrochemical microscopy. *Anal Chem* 69:5059–5066.

- ¹⁷ Wilhelm T, Wittstock G (2003) Analysis of interaction in patterned multienzyme layers by using scanning electrochemical microscopy. *Angew Chem Int Edit* 42:2248–2250.
- ¹⁸ Zhan D, Li X, Zhan W, Fan FF, Bard AJ (2007) Scanning electrochemical microscopy. 58. Application of a micropipet-supported ITIES tip to detect Ag⁺ and study its effect on fibroblast cells. *Anal Chem* 79:5225–5231.
- ¹⁹ Kirchner CN, Träuble M, Wittstock G (2010) Diffusion and reaction in microbead agglomerates. *Anal Chem* 82:2626–2635.
20. Li X, Bard AJ (2009) Scanning electrochemical microscopy of HeLa cells—Effects of ferrocene methanol and silver ion. *J Electroanal Chem* 628:35–42.
- ²¹ Cai C, Liu B, Mirkin MV, Frank HA, Rusling JF (2002) Scanning electrochemical microscopy of living cells. *Anal Chem* 74:114–119.
- ²² Liu B, Rotenberg SA, Mirkin MV (2000) Scanning electrochemical microscopy of living cells: Different redox reactivities of human breast cells and metastatic breast cancer cells. *Proc Natl Acad Sci USA* 97:9855–9860.
- ²³ Fan FRF, Bard AJ (1999) Imaging of biological macromolecules on mica in humid air by scanning electrochemical microscopy. *Proc Natl Acad Sci USA* 96:14222–14227.
- ²⁴ Zhan D, Fan FF, Bard AJ (2008) The Kv channel blocker 4-aminopyridine enhances Ag⁺ uptake: A scanning electrochemical microscopy study of single living cells. *Proc Natl Acad Sci USA* 105:12118–12122.
- ²⁵ Anderl JN, Franklin MJ, Stewart PS (2000) Role of antibiotic penetration limitation in *Klebsiella pneumoniae* biofilm resistance to ampicillin and ciprofloxacin. *Antimicrob Agents Chemother* 44(7):1818–1824.
- ²⁶ Bard AJ (1961) Effect of electrode configuration and transition time in solid electrode chronopotentiometry. *Anal Chem* 33:11–15.

Vita

Dipankar Koley was born in Chandernagore, India in 1979. After attending high school in Chandernagore he moved to Haldia to obtain B. Tech (Hons) in chemical engineering from “Haldia Institute of Technology” in summer of 2003. He then moved to the U.S.A to attend Texas A&M-Commerce for graduate studies. His master’s research involved surface chemistry to understand low temperature carbon monoxide oxidation on silica based palladium catalyst. He earned his M.S. degree in chemistry in summer 2005.

In Fall 2005 he moved to University of Texas at Austin to join Dr. Allen J Bard laboratory to pursue his graduate research in electrochemistry. He will be finishing his PhD study in the summer of 2011.

His professional interest primarily focuses on developing scanning electrochemical microscopy (SECM) as a new electroanalytical tool for understanding complex biological problems such as multidrug resistance phenomenon in cancer cells as well as microbial communication in a biofilm structure.

Permanent address (or email): Tematha, Moran road, Chandernagore, West Bengal,
India. (dipankarkoley@yahoo.com)

This dissertation was typed by author.